



Doppler Constraints on Planetary Companions to Nearby Sun-like Stars: An Archival Radial Velocity Survey of Southern Targets for Proposed NASA Direct Imaging Missions*

Katherine Laliotis¹, Jennifer A. Burt², Eric E. Mamajek^{2,3}, Zhexing Li⁴, Volker Perdelwitz^{5,6}, Jinglin Zhao⁷, R. Paul Butler⁸, Bradford Holden⁹, Lee Rosenthal¹⁰, B. J. Fulton^{10,11}, Fabo Feng^{12,13}, Stephen R. Kane⁴, Jeremy Bailey¹⁴, Brad Carter¹⁵, Jeffrey D. Crane¹⁶, Elise Furlan¹⁷, Crystal L. Gnillka¹⁸, Steve B. Howell¹⁸, Gregory Laughlin¹⁹, Stephen A. Shectman¹⁶, Johanna K. Teske⁸, C. G. Tinney²⁰, Steven S. Vogt⁹, Sharon Xuesong Wang²¹, and Robert A. Wittenmyer¹⁵

¹ Department of Physics, The Ohio State University, 191 West Woodruff Avenue, Columbus, OH 43210, USA; laliotis.2@osu.edu

² Jet Propulsion Laboratory, California Institute of Technology, 4800 Oak Grove Drive, Pasadena, CA 91109, USA

³ Department of Physics and Astronomy, University of Rochester, Rochester, NY 14627-0171, USA

⁴ Department of Earth and Planetary Sciences, University of California, Riverside, CA 92521, USA

⁵ Kimmel fellow, Department of Earth and Planetary Sciences, Weizmann Institute of Science, Rehovot, 76100, Israel

⁶ Hamburger Sternwarte, Universität Hamburg, Gojenbergsweg 112, D-21029 Hamburg, Germany

⁷ Department of Astronomy & Astrophysics, The Pennsylvania State University, 525 Davey Lab, University Park, PA 16802, USA

⁸ Earth & Planets Laboratory, Carnegie Institution for Science, 5241 Broad Branch Road, NW, Washington, DC 20015, USA

⁹ UCO/Lick Observatory, Department of Astronomy and Astrophysics, University of California at Santa Cruz, Santa Cruz, CA 95064, USA

¹⁰ Cahill Center for Astronomy & Astrophysics, California Institute of Technology, Pasadena, CA 91125, USA

¹¹ IPAC-NASA Exoplanet Science Institute, Pasadena, CA 91125, USA

¹² Tsung-Dao Lee Institute, Shanghai Jiao Tong University, Shengrong Road 520, Shanghai, 201210, People's Republic of China

¹³ Department of Astronomy, School of Physics and Astronomy, Shanghai Jiao Tong University, 800 Dongchuan Road, Shanghai 200240, People's Republic of China

¹⁴ School of Physics, University of New South Wales, Sydney, NSW 2052, Australia

¹⁵ University of Southern Queensland, Centre for Astrophysics, USQ Toowoomba, QLD 4350, Australia

¹⁶ The Observatories of the Carnegie Institution for Science, 813 Santa Barbara Street, Pasadena, CA 91101, USA

¹⁷ NASA Exoplanet Science Institute, Caltech/IPAC, Mail Code 100-22, 1200 E. California Boulevard, Pasadena, CA 91125, USA

¹⁸ NASA Ames Research Center, Moffett Field, CA 94035, USA

¹⁹ Department of Astronomy, Yale University, New Haven, CT 06511, USA

²⁰ School of Physics and Australian Centre for Astrobiology, University of New South Wales, Sydney 2052, Australia

²¹ Department of Astronomy, Tsinghua University, Beijing 100084, People's Republic of China

Received 2022 April 29; revised 2022 December 23; accepted 2022 December 31; published 2023 March 27

Abstract

Directly imaging temperate rocky planets orbiting nearby, Sun-like stars with a 6 m class IR/O/UV space telescope, recently dubbed the Habitable Worlds Observatory, is a high-priority goal of the Astro2020 Decadal Survey. To prepare for future direct imaging (DI) surveys, the list of potential targets should be thoroughly vetted to maximize efficiency and scientific yield. We present an analysis of archival radial velocity data for southern stars from the NASA/NSF Extreme Precision Radial Velocity (EPRV) Working Group's list of high-priority target stars for future DI missions (drawn from the HabEx, LUVOIR, and Starshade Rendezvous studies). For each star, we constrain the region of companion mass and period parameter space we are already sensitive to based on the observational baseline, sampling, and precision of the archival radial velocity (RV) data. Additionally, for some of the targets, we report new estimates of magnetic activity cycle periods, rotation periods, improved orbital parameters for previously known exoplanets, and new candidate planet signals that require further vetting or observations to confirm. Our results show that for many of these stars we are not yet sensitive to even Saturn-mass planets in the habitable zone, let alone smaller planets, highlighting the need for future EPRV vetting efforts before the launch of a DI mission. We present evidence that the candidate temperate super-Earth exoplanet HD 85512b is most likely due to the star's rotation, and report an RV acceleration for δ Pav that supports the existence of a distant giant planet previously inferred from astrometry.

Unified Astronomy Thesaurus concepts: Exoplanet astronomy (486); Exoplanet systems (484); Radial velocity (1332)

Supporting material: figure sets, machine-readable tables

1. Introduction

In order to further push the boundaries of the search for life elsewhere in the universe, astronomers must advance our capabilities to detect temperate, terrestrial planets orbiting Sun-like stars and to characterize their atmospheres. To detect and spectrally characterize many such planets in reflected light, it is expected that future space-based direct imaging (DI) missions will employ starlight suppression

* This paper includes data gathered with the 6.5 m Magellan Telescopes located at Las Campanas Observatory, Chile.



Original content from this work may be used under the terms of the [Creative Commons Attribution 4.0 licence](https://creativecommons.org/licenses/by/4.0/). Any further distribution of this work must maintain attribution to the author(s) and the title of the work, journal citation and DOI.

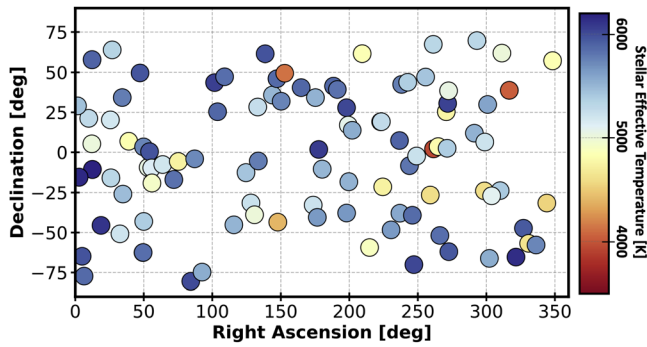


Figure 1. Stars identified by the EPRV Working Group as potential targets for future DI missions such as HabEx and LUVOIR that would aim to detect and characterize Earth-analog exoplanets. This work focuses primarily on the stars located in the Southern hemisphere.

technologies such as coronagraphs or starshades, and survey of the order of ~ 100 of the nearest Sun-like stars (National Academies of Sciences, Engineering, & Medicine 2018, 2021). Habitable Exoplanet Observatory (HabEx) and the Large Ultraviolet Optical Infrared Surveyor (LUVOIR), two proposed space-based DI mission concepts considered by the 2020 Decadal Survey on Astronomy and Astrophysics (Astro2020²²), were designed to obtain direct atmospheric spectra and enable atmospheric characterization of small, temperate planets (The LUVOIR Team 2019; Gaudi et al. 2020). Pathways to Habitable Worlds was a priority science theme in the Astro2020 Decadal Survey,²³ which included a recommendation²⁴ for NASA to work²⁵ toward launching a 6-m class UV/Visible/IR space observatory in the early 2040s to spectrally search for biosignatures in the atmospheres of directly imaged temperate rocky planets orbiting nearby stars.²⁶ The scale of the proposed observatory is intermediate between the HabEx and LUVOIR-B concepts, and will require further technology and science maturation and trade studies to converge on an architecture before project implementation later in the 2020s. To inform trade studies and simulate mission yields, and ultimately to fulfill the Astro2020 Decadal goal of searching for biosignatures in the atmospheres of ~ 25 imaged exo-Earths, one requires a prioritized and carefully vetted target list.

The stars that are chosen for a future DI mission must meet criteria related to their T_{eff} , brightness (e.g., V_{mag}), luminosity, multiplicity, and distance from Earth. Of primary

importance is the maximum separation that a potentially habitable planet can achieve in its orbit around its star, as seen from Earth. The habitable zone annuli scale as the square root of the luminosity, such that one can define the Earth equivalent insolation distance (EEID) as $\sqrt{L/L_{\odot}}$ au, or in angular separation $\theta_{\text{EEID}} = \sqrt{L/L_{\odot}} D_{\text{pc}}^{-1} = \sqrt{L/L_{\odot}} \varpi$, for a star at distance D_{pc} (parsecs) ($=1/\varpi$) and parallax ϖ (arcseconds). For a planet to be visible, at least part of its orbit must be outside the inner working angles (IWAs) for the observatory's means of starlight suppression—usually either a coronagraph or starshade²⁷—so that the incoming starlight does not overwhelm the planet's signal. Instrumentation limits constrain the primary candidate stars' locations to be within a range where a ~ 1 au orbit would have a minimum on-sky separation of ~ 40 mas for LUVOIR (The LUVOIR Team 2019) and larger separations are required for HabEx and Starshade Rendezvous. Given the limited number of Sun-like stars in the solar neighborhood, and the sizes of their habitable zones, this places tight limits on the distance ranges and sample sizes of targets well suited to Earth-analog searches with a DI mission. An ideal observation candidate must both exhibit Sun-like characteristics and be close enough that its habitable zone would be accessible to a DI mission's instruments.

The accuracy to which the properties of the exoplanets' atmosphere can be determined will rely on precise measurements of the planets' surface gravities, which in turn require precise planet mass measurements (Batalha et al. 2019). There are two practical methods for the foreseeable future for measuring the masses of temperate rocky exoplanets orbiting Sun-like stars—radial velocity and astrometry—both of which would require considerable advancement to achieve this goal (Lovis & Fischer 2010; Quirrenbach 2010; National Academies of Sciences, Engineering, & Medicine 2018). It is generally acknowledged, however, that extreme precision radial velocity (EPRV) measurements obtained via spectrographs with single measurement precisions $< 10 \text{ cm s}^{-1}$ are likely the most direct route to detecting Earth analogs around Sun-like stars (National Academies of Sciences, Engineering, & Medicine 2018). The current generation of radial velocity (RV) instruments is beginning to demonstrate single measurement precisions at the $30\text{--}50 \text{ cm s}^{-1}$ level (see, e.g., Seifahrt et al. 2018; Brewer et al. 2020; Pepe et al. 2021; Trifonov et al. 2021). Further improvements to reach the 10 cm s^{-1} level will require advances in sustained instrument stability, wavelength calibration, and data extraction and analysis techniques with a focus on methods for mitigating stellar variability.

Exploring solutions to these challenges that prevent mass measurements for Earth analogs was the goal of the EPRV Working Group chartered by NASA and the NSF.²⁸ The EPRV Working Group was charged with devising a path toward developing methods and facilities that will be capable of accurately measuring the masses of temperate terrestrial

²² <https://www.nationalacademies.org/our-work/decadal-survey-on-astronomy-and-astrophysics-2020-astro2020>

²³ Released 2021 November, near the completion of this study.

²⁴ “Recommendation: After a successful mission and technology maturation program, NASA should embark on a program to realize a mission to search for biosignatures from a robust number of about ~ 25 habitable zone planets and to be a transformative facility for general astrophysics. If mission and technology maturation are successful, as determined by an independent review, implementation should start in the latter part of the decade, with a target launch in the first half of the 2040s.”

²⁵ NASA Administrator Bill Nelson recently announced plans in 2022 December to the National Academies on the 50th anniversary of the Apollo 17 mission to proceed with the Decadal mission concept for a large UV/Vis/IR space telescope with the name Habitable Worlds Observatory.

²⁶ We note that an alternative approach to discovering and characterizing rocky temperate exoplanets via space-based mid-infrared nulling interferometry is being pursued for the Large Interferometer for Exoplanets (LIFE) concept for ESA's Voyage 2050 program (Dannert et al. 2022; Hansen & Ireland 2022; Konrad et al. 2022; Quanz et al. 2022).

²⁷ For LUVOIR's ECLIPS instrument (a coronagraph with imaging and imaging spectroscopy), $\text{IWA} = 3.5\lambda/D$ for wavelength λ (between 0.2 and $2.0 \mu\text{m}$) and aperture size D (15 m for LUVOIR-A, 8 m for LUVOIR-B; The LUVOIR Team 2019). For HabEx ($D = 4 \text{ m}$), $\text{IWA} = 2.4\lambda/D$ for the coronagraph (λ range $0.48\text{--}1.8 \mu\text{m}$, corresponding to 62 mas for $0.5 \mu\text{m}$) and 58 mas for the starshade over $\lambda = 0.3\text{--}1.0 \mu\text{m}$. Astro2020 recommended an observatory with $D \simeq 6 \text{ m}$; however, since multiple architectures will likely be considered, the IWA is not yet defined—but should ultimately be a low multiple of λ/D .

²⁸ <https://exoplanets.nasa.gov/exep/NNExplore/EPRV/>

Table 1
Sample and Stellar Parameters

HD	GJ	T_{eff}	$\log g$	[Fe/H]	References	Spec. Type	References	$\log L/L_{\odot}$	References(L)
693	10	6169	4.07	-0.34	1	F8V Fe-0.8 CH-0.5	2	0.477	3
1581	17	5977	4.51	-0.18	4	F9.5V	2	0.101	3
2151	19	5873	3.98	-0.04	5	G0V	2	0.541	27
4628	33	5009	4.62	-0.24	1	K2V	6	-0.523	3
7570	55	6111	4.36	0.17	7	F9V Fe+0.4	2	0.302	3
10700	71	5331	4.44	-0.49	5	G8V	8	-0.296	3
13445	86A	5217	4.56	-0.23	9	K1V	2	-0.389	3
14412	95	5368	4.55	-0.47	10	G8V	2	-0.351	3
16160	105A	4866	4.66	-0.12	11	K3V	8	-0.549	3
20766	136	5713	4.48	-0.20	12	G2V	2	-0.100	3
20794	139	5398	4.41	-0.41	13	G8V	2	-0.184	3
20807	138	5837	4.47	-0.22	12	G1V	8	0.007	3
22049	144	5050	4.60	-0.09	5	K2V	8	-0.471	3
22484	147	5996	3.97	-0.05	14	F9IV-V	8	0.494	27
23249	150	5057	3.80	0.08	15	K1IV	6	0.500	16
23356	...	4960	4.60	-0.09	9	K2.5V	2	-0.515	3
26965	166A	5128	4.37	-0.37	17	K0.5V	2	-0.364	3
30495	177	5870	4.54	0.04	18	G1.5V CH-0.5	2	-0.015	3
32147	183	4745	4.57	0.19	9	K3+V	6	-0.537	3
38858	1085	5719	4.49	-0.23	13	G2V	6	-0.083	3
39091	9189	6003	4.42	0.09	4	G0V	2	0.186	3
43834	231	5569	4.43	0.11	9	G7V	2	-0.063	3
50281	250A	4758	4.92	0.14	11	K3.5V	6	-0.658	3
69830	302	5390	4.39	-0.05	12	G8+V	2	-0.216	3
72673	309	5243	4.46	-0.41	4	G9V	2	-0.394	3
75732	324A	5328	4.58	0.46	1	K0IV-V	6	-0.197	3
76151	327	5776	4.54	0.11	19	G2V	8	-0.013	3
85512	370	4400	4.36	-0.26	13	K6V(k)	2	-0.778	3
100623	432A	5189	4.68	-0.37	11	K0-V	2	-0.432	3
102365	442A	5629	4.44	-0.29	4	G2V	2	-0.074	3
102870	449	6083	4.08	0.24	5	F8.5IV-V	20	0.576	3
104304	454	5510	4.33	0.25	1	G8IV	2	-0.054	3
114613	9432	5672	3.95	0.12	15	G4IV	2	0.626	3
115617	506	5556	4.35	-0.02	21	G6.5V	8	-0.078	3
125072	542	4899	4.55	0.28	9	K3IV	2	-0.466	3
131977	570A	4744	4.76	0.12	11	K4V	8	-0.653	3
136352	582	5664	4.39	-0.34	4	G2-V	2	0.012	3
140901	599A	5586	4.45	0.09	9	G7IV-V	2	-0.088	3
146233	616	5808	4.44	0.04	18	G2Va	8	0.039	3
147584	624	6030	4.43	-0.08	9	F9V	2	0.134	3
149661	631	5289	4.61	0.05	1	K0V(k)	2	-0.335	3
156026	664	4600	4.70	-0.34	9	K5V(k)	2	-0.803	3
160346	688	4808	4.56	-0.08	9	K2.5V	6	-0.480	22
160691	691	5845	4.27	0.35	5	G3IV-V	2	0.278	3
165341	702A	5314	4.51	0.05	1	K0-V	8	-0.221	23
188512	771A	5117	3.64	-0.19	15	G8IV	8	0.780	16
190248	780	5566	4.24	0.32	13	G8IV	2	0.097	3
192310	785	5104	4.54	0.06	9	K2+V	2	-0.394	3
196761	796	5415	4.43	-0.31	4	G7.5IV-V	8	-0.252	3
203608	827	6150	4.35	-0.66	9	F9V Fe-1.4 CH-0.7	2	0.166	3
207129	838	5937	4.49	0.00	4	G0V Fe+0.4	2	0.082	3
209100	845	4649	4.63	-0.19	9	K4V(k)	2	-0.654	3
216803	879	4647	4.88	0.07	24	K4+Vk	2	-0.707	3

References. (1) Takeda et al. (2005), (2) Gray et al. (2006), (3) Stassun et al. (2019), (4) Sousa et al. (2008), (5) Jofré et al. (2014), (6) Gray et al. (2003), (7) Ramírez et al. (2014), (8) Keenan & McNeil (1989), (9) Ramírez et al. (2013), (10) Santos et al. (2004), (11) Valenti & Fischer (2005), (12) Adibekyan et al. (2016), (13) Tsantaki et al. (2013), (14) Gonzalez et al. (2010), (15) Maldonado & Villaver (2016), (16) Brewer et al. (2016) (17) Montes et al. (2018), (18) Spina et al. (2016), (19) Mahdi et al. (2016), (20) Gray et al. (2001), (21) Sousa et al. (2018), (22) Luck (2017), (23) Schofield et al. (2019), (24) Santos et al. (2001), (25) Luminosities for these stars were calculated using the Virtual Observatory SED Analyzer version 7.0 (VOSA; Bayo et al. 2008) assuming zero extinction, $\log(g) = 4.0$, and BT-Settl-AGSS2009 model spectra for both stars. This produces best-fit $\log(L/L_{\odot})$ values of $+0.5407 \pm 0.0065$ for HD 2151 and $+0.494 \pm 0.0066$ dex for HD 22484.

(This table is available in machine-readable form.)

exoplanets orbiting Sun-like stars.²⁹ The Working Group’s final report (Crass et al. 2021) includes recommendations for advancements in stellar activity and telluric mitigation, instrument efficiency and accuracy, and research and analysis techniques.

In parallel to these advancements in RV instrumentation and analysis, there must also be a concerted effort to better understand the potential DI target stars. One way to do this is by studying archival RV data sets taken using previous, less-precise ($\sigma_{\text{RV}} < 5 \text{ m s}^{-1}$), generations of RV spectrographs. The EPRV Working Group curated a list of ~ 100 nearby, Sun-like (F9-K7) stars that are promising candidates for a future DI mission, many of which have already been included in multiple RV surveys over the past three decades as the community’s interests have often been tied to bright G and K dwarfs.

In this study, we analyze archival radial velocity and stellar activity data from the the High Accuracy Radial Velocity Planet Searcher (HARPS), High Resolution Spectrometer (HIRES), University College London Échelle Spectrograph (UCLES), Automated Planet Finder (APF), and Planet Finder Spectrometer (PFS) instruments for 52 southern hemisphere stars identified as promising future DI mission targets. We perform planet injection and recovery tests to assess the completeness of the existing RV data as a function of planet mass and orbital period, so as to identify regions of mass/period parameter space in which planet signals might still be hiding. Any mass/period gaps identified in this work can then be filled by directed future observations, contributing to the completeness of the target star list data. In preparing the RV data sets for the injection/recovery analysis, we first identify and remove significant signals from the RV time series. This results in the detection of numerous, previously confirmed exoplanets; a number of new planet candidates; and rotation and magnetic activity cycles within the data.

The structure of this paper is as follows. In Section 2, we discuss the stars chosen for this project and the types and sources of the data analyzed. In Section 3 we detail the sources and treatments of the data sets used in this work. In Section 4, we present the different methods of analysis used to characterize the stars’ existing RV sensitivity. In Sections 5–7 we explain the results of our analysis. Each star on the target list has a subsection including updates to parameters of any known planets, evidence of strong stellar activity cycles, and any new signals recovered. We address those targets that lacked any significant signals in Section 7. Section 8 contains a general discussion of our results, including highlights of the analysis carried out in this work and exploration of major gaps we have identified in the archival RV data. Finally, in Section 9 we cover the conclusions drawn from this work, and identify future work necessary before any target list is finalized for a DI mission concept. The full set of figures for each target, including radial velocity, S-index, completeness contour, and, if relevant, H α activity and speckle imaging plots is available.

2. Stellar Target List

Our list of target stars is drawn from the EPRV Working Group, and a full description of the selection process and criteria considered can be found in its final presentation³⁰ and report (Crass et al. 2021). In brief, the Working Group cross-matched target lists provided by the HabEx, LUVOIR-A, LUVOIR-B, and Starshade Rendezvous teams (Seager et al. 2018; The LUVOIR Team 2019; Gaudi et al. 2020) to assemble a combined list of potential target stars. It then compiled information on the stars’ effective temperatures, apparent magnitudes, rotational velocities, metallicities, and surface gravities, among other traits. From this catalog, they culled those stars with spectral types from F7-K9, projected rotational velocities $v \sin i < 5 \text{ km s}^{-1}$, and that appear on at least two of the mission concept target lists. Stars were not eliminated based on knowledge of their stellar activity levels as the characterization and mitigation of stellar variability is an active field, and we may yet overcome the obstacles it presents. The resulting list includes 101 stars (Figure 1).

For this work, we have chosen to focus primarily on the 53 stars from this list located in the southern hemisphere³¹ (Figure 2) due to the recent publication of archival HARPS RV data that is now available on the RVBank website (Trifonov et al. 2020).

3. Data

3.1. Radial Velocities

In this work, we include data sets consisting of unbinned radial velocity measurements from five different instruments: HARPS (on the ESO 3.6 m telescope; Mayor et al. 2003), HIRES (on the 10 m Keck I telescope; Vogt et al. 1994), the Levy spectrometer (on the 2.4 m APF telescope; Vogt et al. 2014), PFS (on the 6.5 m Magellan Clay telescope; Crane et al. 2006, 2008, 2010), and UCLES (on the 3.9 m Anglo-Australian Telescope; Diego et al. 1990). Table 2 lists the number of archival RV epochs (binned at a 12 hr cadence) acquired by each facility. All radial velocity and activity indicator measurements for each star are provided in a machine-readable table alongside this paper in their original, unbinned, form (Table 3).

The HARPS instrument uses multiple observing fibers; one directed at the stellar target, and one directed instead at a Th-Ar calibration lamp. The calibration lamp serves as a wavelength reference for the stellar spectra. HARPS has a resolving power of $\sim 115,000$ and a spectral grasp of 3800–6900 Å (Pepe et al. 2002; Cosentino et al. 2012). All HARPS RV data used in this work were downloaded from the HARPS RVBank archive³² (Trifonov et al. 2020). These RVBank velocities were

²⁹ The final NASA concept study reports for the HabEx, LUVOIR, and Starshade Rendezvous reports for the Astro 2020 Decadal Survey are posted at: <https://science.nasa.gov/astrophysics/2020-decadal-survey-planning>.

³⁰ https://exoplanets.nasa.gov/internal_resources/1556/

³¹ It should be noted that this list was assembled before the Astro2020 Decadal Survey was released, which recommended a 6 m class space telescope. From subsequent analysis and literature survey (E. E. Mamajek & K. R. Stapelfeldt 2023, in preparation), 10 of the sample stars in Table 1 may be undesirable targets for a survey for potentially habitable exoplanets with a 6 m class space telescope: four systems have habitable zones prohibitively close to their stars (HD 85512 [EEID = 36 mas], HD 23356 [EEID = 40 mas], HD 125072 [EEID = 49 mas], and HD 196761 [EEID = 36 mas]), five stars have close ($< 3''$) companions (HD 16160, HD 147584, HD 104304A, HD 13445A, and HD 160346), and one has high luminosity and its HZ rocky planets may have planet-to-star brightness ratios that are prohibitively low (HD 188512). These 10 stars will be omitted from a NASA ExEP mission target list meant to inform precursor science for the Habitable Worlds Observatory.

³² https://www2.mpia-hd.mpg.de/homes/trifonov/HARPS_RVBank.html

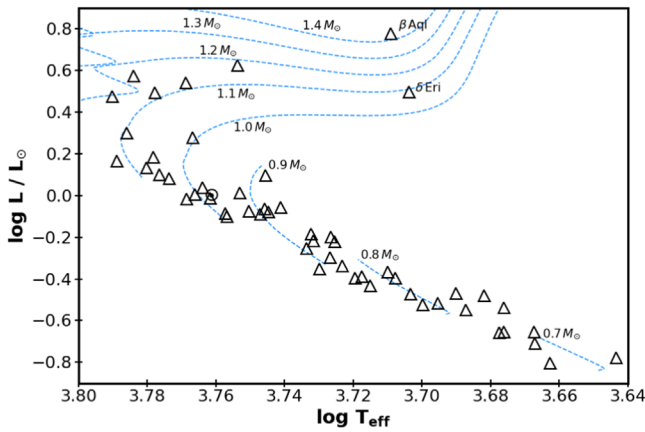


Figure 2. HR diagram containing the target stars in this study. The dashed blue lines are MIST V1.2 evolutionary tracks from Choi et al. (2016) covering masses $0.7\text{--}1.4 M_{\odot}$ over an age range 100 Myr–14 Gyr. The tracks adopt a protosolar mix (initial $Y = 0.2703$, $Z = 0.0142857$, $[\alpha/\text{Fe}] = 0$, $v/v_{\text{crit}} = 0$). The Sun is depicted using the \odot symbol.

generated using the *SERVAL* pipeline (Zechmeister et al. 2020), which uses a template matching approach (Zechmeister et al. 2018). For each star, *SERVAL* creates a high signal-to-noise ratio template spectrum by shifting and coadding all individual spectra of that star. The template is then used to derive RVs from the same observed spectra by using a χ^2 -minimization approach. The final velocities were checked for any nightly systematic errors that can be corrected in order to increase the precision of the RV data set.

HIRES, APF, UCLES, and PFS are Iodine-based instruments, meaning that they each include a cell of gaseous I_2 within the converging beam of their respective telescopes. Incoming stellar spectra are imprinted in a high-density forest of I_2 lines in the 5000–6200 Å bandpass. These lines act both as a calibrator for the wavelengths of the stellar spectra and as a representative for the point-spread function (PSF) of each instrument. After extraction of the iodine region of the spectrum, the stellar spectrum must be deconvolved from the I_2 absorption lines such that the wavelengths, instrument PSFs, and Doppler shifts may be extracted. This is accomplished by splitting each iodine region into 2 Å chunks, and then analyzing them via the spectral synthesis technique outlined in Butler et al. (1996). A weighted mean of all of the Doppler velocities of the individual chunks is taken, and serves as the final Doppler velocity for each individual observation. The standard deviation of all of the 2 Å chunks (~ 800 for PFS and ~ 700 for the APF and HIRES) constitutes the total internal uncertainty for each velocity measurement. The time stamps for each iodine-based RV are converted from their pipeline-produced MJD values to BJD_{TDB} time stamps using the *Pexo* modeling package (Feng et al. 2019b).

We note that three of the above spectrographs have undergone instrumental upgrades since their deployment. The HIRES detector was replaced with a new mosaic CCD in 2004 August, HARPS moved to the use of an octagonal science fiber in 2015 and in 2018, the PFS detector was replaced with a smaller pixel $10\text{k} \times 10\text{k}$ detector, and the slit used for I_2 observations was changed from $0''.5$ to $0''.3$. In all three cases, we treat the data taken before and after the upgrade as coming from two separate instruments, identified in our RV data sets and figures as “-Pre” and “-Post” velocities.

The instruments cover spectral ranges of 3700–8000 Å for HIRES, 3700–9000 Å for APF, 3900–6700 Å for PFS, and 4800–8400 Å for UCLES; however, the RV measurements are made using only the 5000–6200 Å wavelength region. The typical spectral resolutions for each instrument are: $R \simeq 90,000$ for the APF, 60,000 for HIRES, 45,000 for UCLES, and 80,000/130,000 for PFS pre-/post-upgrade, respectively.

The HIRES data was obtained from the public Earth Bound Planet Search archive,³³ which provides updates to the Butler et al. (2017) HIRES data catalog. The final HIRES data point included in this analysis was taken on 2017 December 26. The APF, PFS, and UCLES data were provided by the corresponding instrument teams.

For each instrument’s data set for a given star, we apply a robust sigma clipping where any points farther than 5σ from the mean are discarded as outliers. We visually inspect the points identified as outliers in each case, and find that in practice this analysis flags 1–3 data points per instrument per star, which is generally a small percentage of the overall data. Once each instrument’s outliers are removed, we combine the cleaned data sets from each instrument into a single list. We include a column of data tracking which instrument was used to generate each measurement, so that later analysis can determine offsets between instruments.

There are three stars that, despite having a significant number of HARPS observations, cover time baselines incompatible with our science case. HD 203608 and HD 165341 were both observed over a single week, and HD 147584 was observed over a single night. None of these stars have been targeted by the other instruments in our study, and so we remove them from further consideration.

3.2. S-index Measurements

A major challenge when classifying periodic signals seen in Doppler velocity data is determining whether those signals are due to planetary companions or the star itself. Stellar variability is produced by a variety of surface phenomena that occur and evolve across a range of timescales, but they can be grouped into four broad categories. Acoustic waves within the star cause patches of the surface to rise and fall periodically, creating RV oscillations at the few-meters-per-second level over timescales of minutes (Bouchy & Carrier 2001; Nordlund et al. 2009). Granulation is due to motion within stellar convective cells as hot plasma wells up to the surface before radiatively cooling and sinking back down via intergranular lanes. This process takes anywhere from 20 minutes to 1 day depending on the granule size and, again, results in RV shifts at the few-meters-per-second level (Meunier et al. 2015; Cegla et al. 2019; Meunier & Lagrange 2019). Active regions are areas of increased magnetic flux on the stellar surface such as star spots, plages, and faculae that transit across the visible hemisphere of the star as it rotates. They generally persist for multiple rotation periods and induce cyclic RV variations at the $1\text{--}10 \text{ m s}^{-1}$ level each time they pass over the star’s face (Saar & Donahue 1997; Lockwood et al. 2007; Haywood et al. 2016). Finally, stellar magnetic cycles are driven by stellar dynamos, which are maintained through differential rotation at the tachocline—the interface between a star’s radiative and convective layers. These magnetic cycles vary slowly, generally exhibiting periods of 5–15 yr for Sun-like stars, and can induce RV variations up to 20 m s^{-1} over that time span (Makarov 2010; Meunier et al. 2010; Dumusque et al. 2011). In our case of

³³ <https://ebps.carnegiescience.edu/data/hireskeck-data>

Table 2
Number of Archival RV Epochs Analyzed for Each Target Star

HD	^a HARPS	HIRES	UCLES	^a PFS	APF	HD	^a HARPS	HIRES	UCLES	^a PFS	APF
HD 693	16 [16/0]	0 [0/0]	0	0 [0/0]	0	HD 85512	580 [517/63]	7 [0/7]	31	44 [38/6]	0
HD 1581	329 [262/67]	0 [0/0]	119	0 [0/0]	0	HD 100623	4 [4/0]	64 [16/48]	104	40 [34/6]	0
HD 2151	34 [34/0]	0 [0/0]	163	0 [0/0]	0	HD 102365	82 [78/4]	13 [0/13]	187	33 [22/11]	0
HD 4628	42 [37/5]	117 [0/117]	0	0 [0/0]	71	HD 102870	8 [8/0]	0 [0/0]	0	0 [0/0]	59
HD 7570	19 [19/0]	0 [0/0]	60	0 [0/0]	0	HD 104304	26 [0/26]	42 [0/42]	0	0 [0/0]	14
HD 13445	11 [0/11]	0 [0/0]	74	0 [0/0]	0	HD 114613	20 [13/7]	45 [0/45]	244	39 [27/12]	0
HD 14412	26 [0/26]	139 [24/115]	28	12 [11/1]	0	HD 115617	229 [224/5]	157 [0/157]	169	31 [28/3]	0
HD 16160	45 [45/0]	76 [0/76]	0	0 [0/0]	83	HD 125072	74 [55/19]	0 [0/0]	86	0 [0/0]	0
HD 20766	26 [26/0]	0 [0/0]	58	0 [0/0]	0	HD 131977	22 [22/0]	0 [0/0]	0	0 [0/0]	0
HD 20794	260 [187/73]	0 [0/0]	147	21 [18/3]	0	HD 136352	249 [242/7]	28 [0/28]	169	24 [21/3]	0
HD 20807	99 [76/23]	0 [0/0]	99	16 [13/3]	0	HD 140901	27 [27/0]	0 [0/0]	117	27 [23/4]	0
HD 22049	28 [24/4]	89 [0/89]	0	0 [0/0]	0	HD 146233	177 [119/58]	112 [28/84]	81	15 [15/0]	0
HD 22484	26 [0/26]	8 [0/8]	0	0 [0/0]	71	HD 147584 ^b	1 [1/0]	0	0	0 [0/0]	0
HD 23249	116 [76/40]	55 [20/35]	95	0 [0/0]	29	HD 149661	12 [12/0]	43 [31/12]	14	0 [0/0]	0
HD 23356	14 [14/0]	71 [12/59]	0	0 [0/0]	0	HD 156026	0 [0/0]	27 [18/9]	11	54 [35/19]	59
HD 26965	103 [82/21]	163 [7/156]	112	24 [20/4]	13	HD 160346	34 [34/0]	0 [0/0]	0	0 [0/0]	0
HD 30495	44 [35/9]	6 [0/6]	0	0 [0/0]	0	HD 160691	163 [161/2]	0 [0/0]	178	14 [12/2]	0
HD 32147	41 [37/4]	157 [0/157]	0	27 [22/5]	65	HD 165341 ^b	7 [7/0]	0	0	0 [0/0]	0
HD 38858	103 [91/12]	69 [16/53]	0	0 [0/0]	0	HD 188512	17 [17/0]	57 [7/50]	0	0 [0/0]	0
HD 39091	49 [42/7]	0 [0/0]	77	37 [0/37]	0	HD 190248	391 [279/112]	0 [0/0]	236	0 [0/0]	0
HD 43834	26 [0/26]	0 [0/0]	140	24 [21/3]	0	HD 192310	432 [348/84]	137 [0/137]	171	19 [19/0]	0
HD 50281	12 [12/0]	52 [29/23]	0	0 [0/0]	33	HD 196761	37 [27/10]	63 [30/33]	49	29 [21/8]	0
HD 69830	273 [265/8]	154 [0/154]	24	29 [29/0]	87	HD 203608 ^b	7 [7/0]	0	0	0 [0/0]	0
HD 72673	158 [115/43]	77 [21/56]	63	15 [15/0]	0	HD 207129	111 [98/13]	0 [0/0]	123	22 [15/7]	0
HD 75732	2 [2/0]	220 [23/197]	0	0 [0/0]	25	HD 209100	137 [100/37]	0 [0/0]	0	0 [0/0]	0
HD 76151	7 [7/0]	0 [0/0]	0	0 [0/0]	0	HD 216803	11 [11/0]	16 [6/10]	15	0 [0/0]	0

Notes.

^a The total number of HARPS, HIRES, and PFS RV epochs are followed by a breakdown of how many data points were taken before and after the instruments' upgrades (see Section 3) as the pre- and post-upgrade time series are treated as coming from two different instruments.

^b These stars have thousands of individual observations all taken over observational baselines covering less than 1 week of time, making them incompatible with exoplanet search and injection/recovery analyses. We therefore remove them from further consideration in this paper.

Table 3
Full Time-series Data for Each Target Star

Starname	BJD _{TBD}	RV (m s ⁻¹)	RV _{err} (m s ⁻¹)	Instrument	S-index	S-index _{err}	H α	H α _{err}	File Name
HD 115617	2453026.86393	-3.12	0.95	HARPS-Pre	0.1404	0.0026	-1.0	-1.0	2004-01-22T08:41:20
HD 115617	2453026.86533	-3.98	0.98	HARPS-Pre	0.1426	0.0032	-1.0	-1.0	2004-01-22T08:43:22
HD 115617	2453026.86674	-2.59	0.96	HARPS-Pre	0.1490	0.0028	-1.0	-1.0	2004-01-22T08:45:26
HD 115617	2453026.86822	-3.02	0.94	HARPS-Pre	0.1420	0.0027	-1.0	-1.0	2004-01-22T08:47:29
HD 115617	2453026.86967	-5.38	0.95	HARPS-Pre	0.1471	0.0025	-1.0	-1.0	2004-01-22T08:49:33
HD 115617	2453026.87111	-2.8	0.95	HARPS-Pre	0.1414	0.0028	-1.0	-1.0	2004-01-22T08:51:38
HD 115617	2453026.87254	-4.59	0.95	HARPS-Pre	0.1506	0.0026	-1.0	-1.0	2004-01-22T08:53:42
HD 115617	2453026.87393	-3.23	0.94	HARPS-Pre	0.1423	0.0025	-1.0	-1.0	2004-01-22T08:55:46
HD 115617	2453026.87541	-1.22	0.94	HARPS-Pre	0.1468	0.0025	-1.0	-1.0	2004-01-22T08:57:49
HD 115617	2453026.87686	-4.58	0.94	HARPS-Pre	0.1481	0.0024	-1.0	-1.0	2004-01-22T08:59:54
:	:	:	:	:	:	:	:	:	:

Note. This table contains, for each target, the full set of observations of RVs, S-indices, and H α from each instrument included in this study. Complete time-series data for each target in the format above are available.

(This table is available in its entirety in machine-readable form.)

working primarily with RV data sets taken at relatively low cadence (e.g., once per week or month) the latter two varieties, active regions and magnetic cycles, produce the highest rate of false-positive signals.

A well-established method for tracing a star's variability level is the use of stellar activity indicators, which compare the amount of flux inside activity sensitive lines to the flux in nearby continuum regions. The most common stellar activity

indicators for Sun-like stars are derived from measurement of the emission reversal at the cores of the Fraunhofer H and K lines of Ca II located at 3968 Å and 3934 Å, respectively, which trace chromospheric activity. As the Ca II line core emission is generated in regions of concentrated magnetic fields, these lines serve as a proxy for the number of spots on the star, and often show variations with the star's rotational period. Because stars in the active phases of their magnetic cycles tend to produce

more sunspots (Schwabe 1843), activity indicators based on the Ca II lines can also act as a tracer of long-term magnetic cycles.

For Sun-like stars, the best known Ca II activity indicator is the S-index, which compares the flux in the cores of the H & K lines to two nearby continuum regions denoted as the R and V filters (Wilson 1968; Duncan et al. 1991). The S-index generally takes the form:

$$S_{\text{index}} = \frac{H + K}{R + V} \quad (1)$$

and is often calibrated to the original Mt. Wilson S-index survey, which ran from 1966 to 1983 (Duncan et al. 1991) to allow for comparisons between facilities. Over the Mt. Wilson survey’s two-decade span, 111 F2-M2 stars were monitored continuously from Mt. Wilson and 60% were seen to exhibit magnetic cycles on a 5–15 yr timescale (Baliunas et al. 1995). These time series make clear that the range of variability exhibited by the continuously monitored Mt. Wilson stars is much more diverse than what we observe in the Sun.

To search for evidence of these long-term magnetic cycles, in addition to shorter-term rotational periods, in our RV data sets we first derive an S-index value from each RV spectrum. For the HIRES APF and PFS data sets, these S-index values are generated automatically as part of the data reduction pipelines, and further details can be found in Butler et al. (2017) and Burt et al. (2021). We determine errors for each instrument’s S-index values taking into account photon noise. The resulting uncertainty, by error propagation, is:

$$\sigma_S = S \cdot \sqrt{\frac{\sigma_H^2 + \sigma_K^2}{(H + K)^2} + \frac{\sigma_R^2 + \sigma_V^2}{(R + V)^2}}. \quad (2)$$

In each case we have used a set of overlapping target stars to calibrate the instrument’s S-index measurements to the Mt. Wilson survey so that they can be considered together without concerns for large scaling offsets. In some cases, however, the Mt. Wilson calibration is based on a small number of stars and may introduce nonastrophysical offsets between the instruments. To account for this, our analysis allows us to fit for offsets between the S-index data sets, as described more thoroughly in Section 4.1.

The HARPS RVBank data does not yet provide S-index measurements, and so we instead make use of the methodology described in Perdelwitz et al. (2021). Specifically, we use a set of narrow bands close to the Ca II line cores, along with PHOENIX synthetic spectra (Husser et al. 2013), to derive R'_{HK} . We then convert these into S-Indices using the prescription given by Gomes da Silva et al. (2021) and calibrate the results to the Mount Wilson scale by cross matching with the mean S-indices derived by Duncan et al. (1991). The S-index errors are calculated via a Monte Carlo approach where, in each trial, the flux in each bin of the measured spectrum is randomly displaced within a Gaussian distribution with width of the flux error. The S-index is then evaluated for each trial, and the error is taken to be the standard deviation of the resulting set. This approach yields S-indices for ~93.5% of the HARPS spectra present in the RVBank archives.

Attempts to use these Monte Carlo S-index errors for the HARPS data alongside the photon-noise limited errors derived from the HIRES, PFS, and APF data results in an uneven weighting in favor of the iodine-based instruments. While we

report all of these errors in the data tables that accompany this publication for reference, in practice we adopt a third, alternative method for determining S-index errors so that all four instruments’ data sets are treated in the same way. We begin by selecting six stars (HD 69830, HD 196761, HD 114613, HD 4628, HD 39091, and HD 22484) all of which have at least two dozen observations from at least two of the instruments. We assign all of the S-index data for each star the same error bar of $\sigma_S = 0.01$ and carry out an initial uninformed fit with *RVSearch*. We then combine all of the residual values from each instrument across all stars, measure the standard deviation, and assign that as the global error for that instrument. Those values are: HARPS-Pre : 0.010; HARPS-Post : 0.006; HIRES-Pre : 0.010; HIRES-Post : 0.014; PFS-Pre : 0.005; PFS-Post : 0.009, APF : 0.007. As we expect the S-index measurement to be systematics dominated (e.g., from the deblazing and continuum normalization) rather than photon-noise dominated, this empirical approach to measuring the uncertainty provides a more homogeneous error estimate.

When summarizing the properties of our target stars below, we reference $\log R'_{\text{HK}}$ values for stars where it has been reported in the literature. This metric is also derived using the Ca II H&K absorption lines, but $\log R'_{\text{HK}}$ removes the basal (rotation independent) photospheric flux (Noyes et al. 1984; Schrijver 1987; Mittag et al. 2013). This photospheric flux, which can contaminate the S-index filters, introduces a dependency on stellar effective temperature. By removing it, the $\log R'_{\text{HK}}$ metric produces a measure of activity that can be compared across spectral types.

3.3. $H\alpha$ Equivalent Width Measurements

The UCLES spectrograph cannot simultaneously cover the Iodine region necessary for precise wavelength calibration of the stellar spectra and the Ca II H & K region necessary for extracting the S-index measurements. To provide a stellar activity check on the RVs derived from the AAT data set, we instead make use of the $H\alpha$ absorption line, using measurements of the line’s equivalent width (EW) to detect variations related to the long-term stellar magnetic activity cycle. This $\text{EW}_{H\alpha}$ analysis follows the methodology of Wittenmyer et al. (2017), which is similar to that presented by Robertson et al. (2014), except for the addition of an automated algorithm for continuum normalization and telluric contamination identification near the $H\alpha$ line.

A visual comparison of the resulting $\text{EW}_{H\alpha}$ time series reveals the presence of very similar structured variations among each of the resulting data sets (Figure 3). Given the shared trends between the stars, the source is likely either instrumental or environmental in nature. One potential cause is variations in the water content of the atmosphere. As our $\text{EW}_{H\alpha}$ calculation algorithm does not actively correct for the telluric lines, it is reasonable to assume the $\text{EW}_{H\alpha}$ measurements are subject to effects from atmospheric water content. However, when compared to the historic precipitable water vapor measurements from Siding Spring (e.g., those in Haslebacher et al. 2022), no strong correlation is evident.

While the exact cause of the variations is not clear, we note that the stacked periodograms of a dozen stars (each with dozens of UCLES $H\alpha$ data points but no significant detections) all linearly interpolated onto the same period grid shows prominent peaks at ~1 yr, ~3000 days (approximately half the

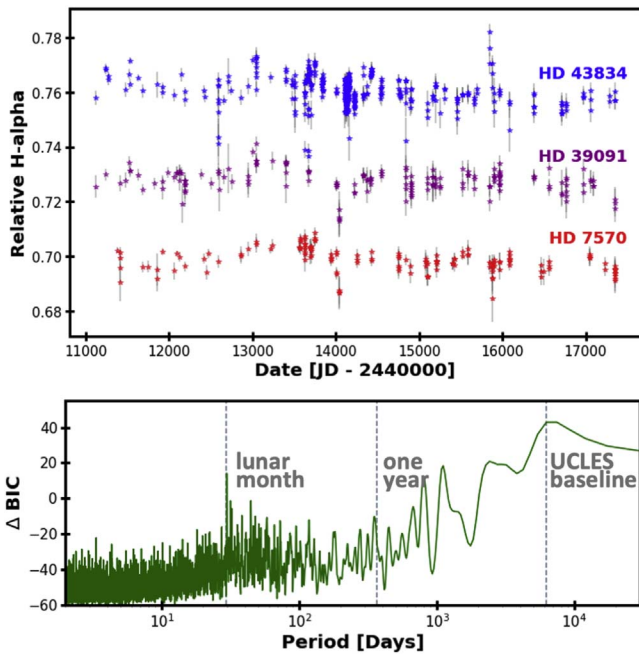


Figure 3. Top: $EW_{H\alpha}$ time series for three of the stars observed with the UCLES spectrograph, offset vertically from one another for ease of viewing. Similar long-term behavior is present in each of these three data sets, suggesting that the cause is not stellar but rather instrumental or environmental. Bottom: stacked periodograms from six stars with at least 100 UCLES $H\alpha$ measurements spread over the majority of the instrument’s ~ 6000 days observational baseline, where no significant signals were detected by RVSearch. The long-term structure seen in the top panel emerges as two humps in this composite periodogram, one at UCLES’ observing baseline (6000 days), and another at half that (3000 days). The impact of the monthly lunar cycle is also evident via a narrow peak at 29.5 days. We therefore treat $H\alpha$ periods detected around any of these three periods with some degree of caution.

UCLES observation time span), and ~ 6000 days (approximately equal to the UCLES observation time span) periods. We therefore advise caution when interpreting the results of the $H\alpha$ RVSearch analysis, especially in the case of long-period signals (LPSs). Shorter-period detections, those in the 10–100 days range where we generally look for evidence of stellar rotation for these F–K dwarfs stars, seem to be unaffected by these long-period variations.

3.4. Speckle Imaging

For a handful of the stars studied in this work, high-resolution speckle imaging observations to search for and/or rule out nearby stellar companions were obtained. The speckle imaging observations were carried out using the ‘Alopeke and Zorro’ instruments at Gemini-North and Gemini-South, respectively (Scott et al. 2021). These instruments observe simultaneously in two bands, $(832 \pm 40 \text{ nm})$ and $(562 \pm 54 \text{ nm})$ obtaining diffraction limited images with IWAs of $0''.026$ and $0''.017$, respectively. All targets were observed using a sequence of short 60 ms exposures. These images were combined using Fourier analysis techniques, examined for stellar companions, and used to produce reconstructed speckle images (see Howell et al. 2011 and Horch et al. 2021). We summarize the observations and the resulting sensitivity to companions in Table 8 and Figure 8.

4. Analysis

4.1. Overview of RVSearch

RVSearch (Rosenthal et al. 2021) is a recently released Python package based on RadVel (Fulton et al. 2018), built specifically to perform uninformed searches for Keplerian signals in RV data and to perform injection and recovery analysis of RV time-series data.

RVSearch’s uninformed search function is used to identify candidate signals in our compiled radial velocity, S-index, and $H\alpha$ data sets. For each data set, we bin the input velocities/activity measurements to nightly data points to decrease the computational requirements and set a minimum search period of 2 days and a maximum search period of three times the total observational baseline days. In addition to any Keplerian signals, RVSearch also fits for a constant offset between each instrument’s data set and for the “jitter” of each instrument. This jitter term is used to address the unmodeled instrumental effects or stellar variability that induce additional scatter in the RV time series and encompasses uncorrelated signals that occur on timescales shorter than the observational baseline.

RVSearch implements an iterative fitting approach when searching for periodic signals in a time series. It first tests for the presence of a linear or quadratic slope in the data, before beginning the Keplerian fitting process by generating a single planet with undefined orbital parameters to become the initial likelihood model. With the initial model in hand, RVSearch defines a set of periods to test³⁴ and computes a ΔBIC goodness-of-fit periodogram by fitting a sinusoid to the data at each fixed period. The Bayesian information criterion (BIC) is used for model selection when considering a finite set of models and is calculated as:

$$\text{BIC} = -2 \ln \mathcal{L}_{\text{max}} + n \ln N \quad (3)$$

where \mathcal{L}_{max} is the maximum likelihood, n is the number of model free parameters, and N is the number of data points (see, e.g., Kass & Raftery 1995, for details). Models with lower BIC values are generally preferred. The ΔBIC value at each period is the difference between the best-fit, $n + 1$ -planet model with the given fixed period, and the n -planet fit to the data.

Once the ΔBIC periodogram has been calculated, a linear fit is applied to the data, and a histogram of periodogram power values is plotted on a log scale. A detection threshold is then constructed such that only 0.1% of periodogram peaks are expected to be high-powered enough to exceed it. This threshold is the empirical false-alarm probability (FAP) of 0.1% (Rosenthal et al. 2021). Any signal above a 0.1% empirical FAP is considered significant. If no significant signals are detected, and the linear or quadratic fit is favored over a complete nondetection, RVSearch returns the parameters of the fitted trend. Table 5 contains the best-fit solutions for stars whose RV data favored linear or quadratic trends.

For our S-index search, we enforce an additional requirement that the ΔBIC value be at least 10 for a signal to be added to the system’s model, even if that corresponds to an FAP value $< 1\%$. This prevents the inclusion of a nonphysical number of short-period signals in sparse data sets, while still being a generous inclusion criterion, as the field standard for

³⁴ The periods are spaced such that the frequency offset between adjacent grid points is $1/2\pi\tau$, where τ is the observational baseline of the full RV time series.

considering a signal worthy of consideration for publication is more often $\Delta\text{BIC} > 25$.

If a significant detection is made, *RVSearch* refines the fit of the signal’s Keplerian orbit by performing a maximum a posteriori (MAP) fit with all model parameters free, including eccentricity, and records the BIC of that best-fit model. The search algorithm then adds an additional planet to the model and repeats the fitting and evaluation process. In the $n+1$ planet fit, the signals are treated simultaneously, so that the change in the BIC can again be evaluated to compare the n -planet fit to the $n+1$ -planet fit. We note here that when analyzing our S-index and $H\alpha$ data sets, the “planet” detections instead refer to activity-driven periodicities in the data sets. If the new planet is supported by the data, the search continues. The uninformed search continues to iterate on the time series until no additional significant signals are present in the periodogram.

At this point, *RVSearch* returns the max-likelihood estimates of the orbital model parameters of the data set, and the model posteriors are sampled via an affine-invariant sampling that is implemented in *RadVel* using the *emcee* package (Foreman-Mackey et al. 2013). The resulting parameter estimates and uncertainties, reported as the median and $\pm 1\sigma$ intervals, are visible in the summary figures produced by *RVSearch* and in our summary tables.

One complication encountered in the fitting process, across both the RV and S-index applications, is the treatment of signals with periods on the order of or greater than the total observational baseline. While the ΔBIC periodogram approach used in the first phase of *RVSearch*’s process can only fully resolve periods shorter than the observational baseline, the posterior sampling is not subject to similar constraints. Thus, in cases where there is a prominent peak in the periodogram that has a peak close to or beyond the observational baseline, the Markov Chain Monte Carlo (MCMC) will sometimes suggest that the true period is $2\times$ the periodogram peak, or in some cases many times larger. In these instances, the traditional MCMC method fails to return a well-sampled model posterior, and the resulting period uncertainty is as large as, if not many times larger than, the period itself. We note these types of detections as “LPS” in our summary tables and report just the initial ΔBIC periodogram peak instead of the final MCMC fit and its corresponding uncertainties, as they are nonphysical. For these signals, note that additional data is required to fully reveal and constrain the underlying signal.

4.2. Identification of Candidate Signals in the Radial Velocity Data

An example *RVSearch* fit to the RV data for HD 115617 is shown in Figure 4. The HD 115617 planetary system was first published in Vogt et al. (2010) using data from the HIRES and UCLES spectrographs. Three planets were discovered with periods and RV semiamplitudes of 4.215 ± 0.0006 days and $2.12 \pm 0.23 \text{ m s}^{-1}$, 38.021 ± 0.034 days and $3.62 \pm 0.23 \text{ m s}^{-1}$, and 123.01 ± 0.55 days and $3.25 \pm 0.39 \text{ m s}^{-1}$ for planets b, c, and d, respectively. Revisiting the system with the available archival data, we supplement the published data with an additional 275 HIRES points, 159 UCLES points, 1248 HARPS points, and 11 PFS points taken between 2004 and 2020.

Incorporating this additional RV data produces a fit consistent with the Vogt et al. (2010) results. All three previously published planets are again detected at statistically significant levels and at very similar period and semi-amplitude

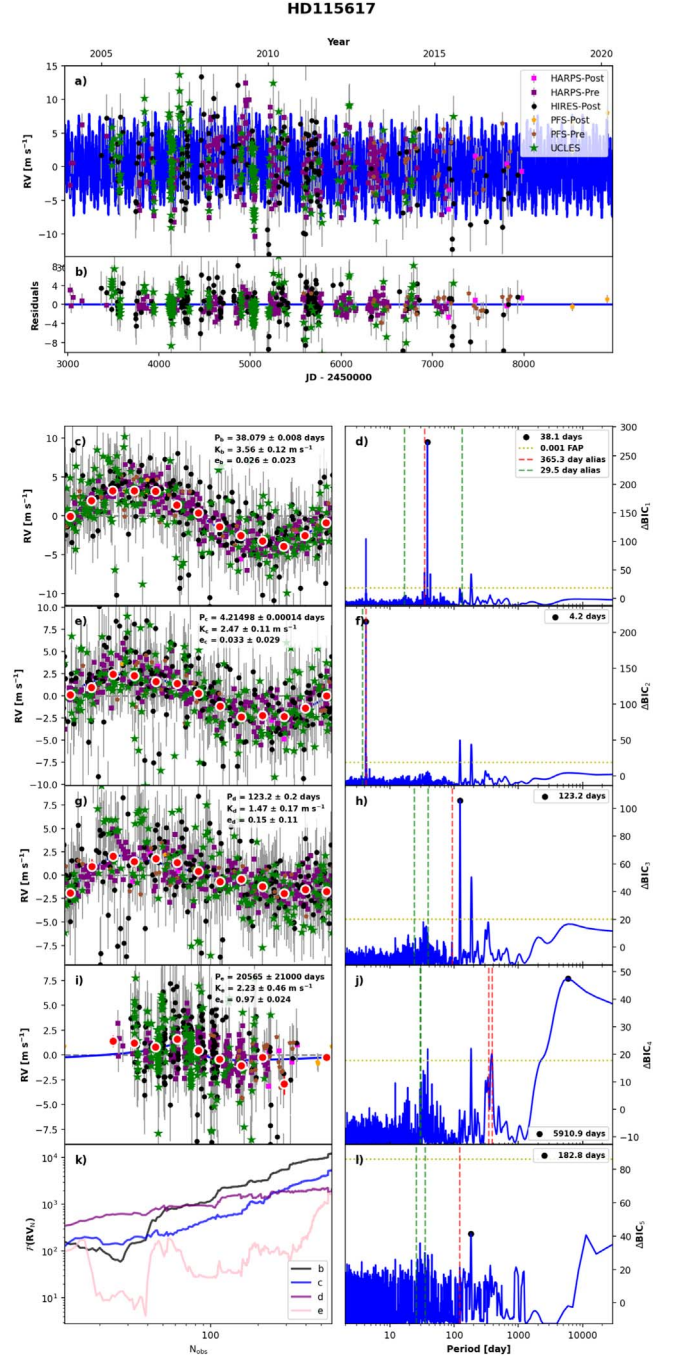


Figure 4. *RVSearch* results for HD 115617. Panel (a) shows the initial RV time series with the best-fit model plotted in blue, and panel (b) shows the RV residuals. Panels (c), (e), and (g) show phased RV curves for the three known planets in the system, and report the best-fit parameters for each orbit. Panels (d), (f), and (h) show the periodograms associated with each planet detection. The yellow horizontal dotted line marks the minimum ΔBIC for a 1% FAP, while the vertical dotted lines show monthly and yearly aliases. Panels (i) and (j) show the periodogram and best-fit curve to a fourth, much longer and highly eccentric signal that is likely driven by stellar variability. Panel (k) shows the RV significance of each signal relative to the number of observations considered and is calculated using the best-fit orbits shown in the left side panels above it, and panel (l) shows the residual periodogram, indicating that no further planets are found in the data set. The complete set of RV summary plots (49 figures) is available.

(The complete figure set (49 images) is available.)

values. The uncertainties on those values, however, are notably improved in the updated fit; the RV semi-amplitude uncertainty decreases by a factor of 2, thereby doubling the detection

Table 4
Keplerian RV Signals Identified by RVSearch (Updated for Resubmission)

ID	Period (days)	K (m s ⁻¹)	Ecc.	$M \sin i$ (M_{\oplus})	FAP	Interp
HD 1581 I	635.0 ± 4.4	0.89 ± 0.14	0.55 ± 0.13	10.08 ^{+1.22} _{-1.17}	7.24e-09	SRC
HD 1581 II	15.653 ± 0.005	0.662 ± 0.096	0.106 ± 0.097	2.56 ^{+0.37} _{-0.38}	1.85e-05	ACT-R
HD 1581 III	29.4661 ± 0.0041	1.6 ± 1.1	0.89 ± 0.12	3.53 ^{+1.15} _{-0.85}	8.26e-04	ACT
HD 2151 I	5365 ± 1400	3.21 ± 0.58	0.54 ± 0.15	81.41 ^{+12.95} _{-13.22}	8.90e-07	ACT
HD 13445 I	88080 ± 46000	3117 ± 750	0.68 ± 0.12	201858.32 ^{+79293.94} _{-71306.73}	2.28e-16	Binary
HD 13445 b	15.764862 ± 4.3e-05	377.58 ± 0.77	0.0485 ± 0.0018	1271.19 ^{+25.51} _{-25.72}	3.56e-83	KP
HD 16160 I	22999 ± 1200	702.5 ± 2.9	0.6075 ± 0.0092	20304.22 ^{+434.82} _{-436.28}	1.23e-26	Binary
HD 20766 I	5643.5	LPS
HD 20794 b	18.305 ± 0.0052	0.807 ± 0.089	0.17 ± 0.11	2.83 ± 0.31	2.20e-11	KP
HD 20794 d	89.766 ± 0.085	0.86 ± 0.12	0.27 ± 0.11	5.02 ^{+0.66} _{-0.64}	7.38e-11	KP
HD 20807 I	3180 ± 130	2.9 ± 0.4	0.23 ± 0.11	62.48 ^{+8.81} _{-8.74}	2.73e-07	SRC
HD 22049 b	2832 ± 120	11.1 ± 1.2	0.09 ± 0.08	211.16 ^{+23.57} _{-24.34}	8.55e-11	KP
HD 23249 I	596.6 ± 2.6	3.0 ± 1.1	0.65 ± 0.14	33.33 ^{+7.89} _{-5.6}	8.18e-08	SRC
HD 26965 I	42.303 ± 0.025	1.4 ± 0.22	0.37 ± 0.17	5.94 ± 0.79	1.48e-08	ACT ^a
HD 26965 II	37.33 ± 0.02	1.17 ± 0.19	0.14 ± 0.12	5.14 ^{+0.84} _{-0.86}	7.45e-05	Alias
HD 26965 III	367.9 ± 3.1	1.63 ± 0.88	0.46 ± 0.27	13.9 ^{+5.13} _{-2.95}	1.37e-05	FP
HD 32147 I	2866 ± 140	1.8 ± 0.21	0.34 ± 0.13	32.02 ^{+3.54} _{-3.49}	3.94e-12	SRC
HD 38858 I	2893 ± 150	2.8 ± 0.3	0.19 ± 0.12	58.15 ^{+6.19} _{-6.01}	1.41e-13	ACT-M
HD 39091 b	2089.05 ± 0.46	196.5 ± 0.6	0.6428 ± 0.0017	3225.56 ^{+58.95} _{-59.18}	1.10e-20	KP
HD 39091 d	125.58 ± 0.27	2.16 ± 0.42	0.16 ± 0.15	17.56 ^{+3.49} _{-3.31}	4.26e-04	KP
HD 43834 I	359.5 ± 1.2	5.5 ± 1.3	0.4 ± 0.14	54.52 ^{+11.29} _{-9.14}	2.82e-06	Candidate
HD 69830 b	8.66897 ± 0.00028	3.4 ± 0.1	0.128 ± 0.028	10.1 ^{+0.38} _{-0.37}	2.15e-62	KP
HD 69830 c	31.6158 ± 0.0051	2.6 ± 0.1	0.03 ± 0.027	12.09 ^{+0.55} _{-0.54}	1.47e-84	KP
HD 69830 d	201.4 ± 0.4	1.5 ± 0.1	0.08 ± 0.071	12.26 ^{+0.89} _{-0.88}	1.89e-36	KP
HD 75732 b	14.65157 ± 0.00015	70.39 ± 0.37	0.0069 ± 0.0047	254.81 ^{+4.79} _{-4.81}	4.13e-97	KP
HD 75732 d	14951 ± 5100	54 ± 5	0.515 ± 0.086	1686.0 ^{+229.11} _{-264.51}	9.03e-20	KP
HD 75732 c	44.39 ± 0.01	9.95 ± 0.37	0.22 ± 0.041	50.78 ^{+2.05} _{-2.0}	2.37e-34	KP
HD 75732 e	0.736546 ± 5e-06	6.26 ± 0.34	0.039 ± 0.035	8.35 ^{+0.48} _{-0.47}	6.05e-28	KP
HD 75732 f	260.88 ± 0.36	5.68 ± 0.48	0.585 ± 0.057	43.4 ^{+3.61} _{-3.5}	3.51e-14	KP
HD 85512 I	3891	1.90e-16	LPS
HD 85512 II	51.195 ± 0.073	0.438 ± 0.079	0.3 ± 0.19	1.86 ^{+0.31} _{-0.3}	6.98e-06	ACT-R ^a
HD 102365 b	121.3 ± 0.25	1.38 ± 0.23	0.28 ± 0.15	9.34 ^{+1.52} _{-1.5}	1.58e-04	KP
HD 114613 I	6622 ± 270	7.29 ± 0.45	0.291 ± 0.061	239.94 ^{+13.54} _{-13.5}	2.87e-34	ACT-M ^a
HD 114613 II	73.141 ± 0.056	2.54 ± 0.45	0.51 ± 0.14	16.72 ^{+2.38} _{-2.42}	4.31e-04	SRC
HD 114613 III	1954 ± 39	2.98 ± 0.52	0.6 ± 0.11	54.01 ^{+7.59} _{-7.5}	2.09e-04	SRC
HD 115617 b	4.21498 ± 0.00014	2.47 ± 0.11	0.033 ± 0.029	5.98 ^{+0.3} _{-0.29}	5.01e-61	KP
HD 115617 c	38.079 ± 0.008	3.56 ± 0.12	0.026 ± 0.023	17.94 ^{+0.73} _{-0.7}	2.93e-46	KP
HD 115617 d	123.2 ± 0.2	1.47 ± 0.17	0.15 ± 0.11	10.82 ^{+1.23} _{-1.03}	5.63e-22	KP
HD 115617 I	5910.9	1.22e-10	LPS
HD 136352 b	11.5767 ± 0.0015	1.65 ± 0.11	0.05 ± 0.045	5.5 ± 0.38	3.67e-38	KP
HD 136352 c	27.5845 ± 0.0064	2.49 ± 0.12	0.041 ± 0.036	11.12 ± 0.57	3.04e-24	KP
HD 136352 d	107.5 ± 0.14	1.44 ± 0.12	0.072 ± 0.061	10.08 ^{+0.87} _{-0.85}	2.06e-23	KP
HD 136352 I	121.66 ± 0.26	0.68 ± 0.13	0.22 ± 0.19	4.69 ^{+0.87} _{-0.86}	9.76e-04	ACT
HD 140901 I	5084 ± 1200	11.6 ± 2.4	0.44 ± 0.25	269.81 ^{+43.83} _{-42.02}	7.32e-04	SRC
HD 146233 I	2374 ± 47	5.47 ± 0.33	0.21 ± 0.07	111.72 ^{+6.67} _{-6.59}	1.31e-25	ACT-M ^a
HD 146233 II	6256 ± 370	4.96 ± 0.57	0.59 ± 0.06	114.86 ^{+12.0} _{-11.43}	7.39e-14	ACT-M
HD 146233 III	19.8777 ± 0.0062	1.73 ± 0.26	0.38 ± 0.16	6.77 ± 0.86	7.23e-09	Candidate
HD 160346 I	83.7286 ± 0.0005	5690.3 ± 2.3	0.2048 ± 0.0003	35280.0 ^{+706.83} _{-716.46}	1.42e-15	Binary
HD 160691 b	644.93 ± 0.28	35.7 ± 0.2	0.0499 ± 0.0082	528.58 ^{+11.05} _{-11.13}	2.16e-46	KP
HD 160691 c	9.6394 ± 0.0008	2.8 ± 0.2	0.132 ± 0.069	10.22 ± 0.73	5.38e-98	KP
HD 160691 d	308.4 ± 0.23	12.7 ± 0.3	0.074 ± 0.016	147.23 ^{+4.63} _{-4.56}	8.24e-131	KP
HD 160691 e	4035 ± 21	22.25 ± 0.24	0.026 ± 0.013	607.79 ^{+14.0} _{-13.99}	2.84e-32	KP
HD 190248 I	360.8 ± 1.9	1.21 ± 0.43	0.29 ± 0.15	12.96 ^{+5.08} _{-3.76}	5.14e-04	FP
HD 192310 b	74.278 ± 0.035	2.484 ± 0.098	0.032 ± 0.027	14.28 ^{+0.64} _{-0.63}	8.11e-50	KP
HD 192310 c	549.1 ± 4.5	1.3 ± 0.1	0.078 ± 0.073	14.96 ^{+1.21} _{-1.18}	3.64e-27	KP
HD 192310 I	3836 ± 240	1.48 ± 0.11	0.34 ± 0.15	29.3 ^{+3.33} _{-3.07}	1.64e-49	ACT-M
HD 192310 II	43.614 ± 0.023	0.93 ± 0.13	0.5 ± 0.1	3.83 ± 0.44	2.41e-13	ACT-R
HD 192310 III	39.509 ± 0.059	1.0 ± 0.1	0.22 ± 0.11	4.48 ± 0.46	1.43e-09	ACT-R
HD 192310 IV	24.559 ± 0.016	0.6 ± 0.1	0.16 ± 0.12	2.46 ^{+0.39} _{-0.4}	7.74e-06	Candidate

Table 4
(Continued)

ID	Period (days)	K (m s ⁻¹)	Ecc.	$M \sin i$ (M_{\oplus})	FAP	Interp
HD 207129 I	1964 ± 49	4.02 ± 0.61	0.44 ± 0.16	72.95 ^{+8.37} _{-8.07}	3.88e-11	ACT-M
HD 209100 I	13138.7	1.38e-37	LPS

Notes. This table contains, for each target, any significant signals identified by RVSearch. We report the period, semiamplitude, eccentricity, minimum mass, false-alarm probability (FAP), and a classification of each signal (KP: Known Planet, Candidate: promising planet candidate signal, Binary: Binary Star, SRC: Source Requiring Confirmation, ACT-R: Stellar Rotation, ACT-M: Magnetic Activity Cycle, LPS: Long-period Signal that does not return a well-sampled posterior and therefore lacks a full orbital solution prompting us to report only the initial Δ BIC periodogram peak, FP: False positive from aliasing or window function of another detection).

^a This signal was reported as a planet in other previous works, but we believe it to be stellar in nature; see corresponding discussion sections for details.

(This table is available in machine-readable form.)

Table 5
Linear/Quadratic RV Trends

HD	Alias	RV Trend
100623	20 Crt	0.00514923 m s ⁻¹ day ⁻¹
104304	GJ 454	-0.19174 m s ⁻¹ day ⁻¹
104304	GJ 454	3.28667e-05 m s ⁻¹ day ⁻²
131977	GJ 570A	-0.0116872 m s ⁻¹ day ⁻¹
188512	β Aql	0.00262165 m s ⁻¹ day ⁻¹
190248	δ Pav	-0.00055 m s ⁻¹ day ⁻¹

Note. Stars from our sample for which the preferred RVSearch model included a linear and/or quadratic trend. All appear to be due to known stellar companions except for δ Pav.

significance, and the period uncertainty decreases by factors of 2–4 across the three planets.

RVSearch also identifies a fourth, much longer-period signal that rises above the detection threshold, with $P = 20565 \pm 21000$ days (Figure 3 panel (i)). The uncertainty on the best-fit orbital period is of the order of the period itself, and it overlaps broadly with an LPS in the star’s activity data (see Section 4.3). Additionally, the strength of this fourth RV signal varies quite noticeably as the number of data points increases. This suggests that only specific clumps of data are providing additional power in the periodogram, as compared to the roughly monotonic increase that is expected for a Keplerian signal (similar to the Mortier & Collier Cameron 2017 stacked periodogram technique). Finally, we note that the period of the peak that is actually being fit by this signal is of approximately the same length as the observation baseline for this target. As discussed in Section 4.1, this results in unphysical MCMC fitting to the signal. These concerns, combined with the fact that the best-fit model’s high eccentricity would produce a semiminor axis of ~ 0.5 au that would disturb the three shorter-period planets that have been robustly vetted, lead us to conclude the final signal detected by RVSearch is not planetary in nature. This signal is classified as an LPS in Table 4.

For all previously discovered planetary systems, HD 115617 included, we report our best-fit results as updates to the published orbital parameters in Section 5.

4.3. Identification of Candidate Activity Signals in the S-index Data

We also use RVSearch to carry out an uninformed search on each star’s combined S-index measurements, similar to the

RV fitting described above. By providing RVSearch with data sets composed of the observation time stamp, S-index, and the empirical instrument-by-instrument S-index errors described in Section 3.2 from each observation, we are able to determine whether the S-index data contain significant periodic signals. Further, if the empirical errors are underestimated, RVSearch’s use of a jitter term will adjust them to more accurately capture the scatter on a star-by-star basis. A list of all of the detected S-index signals is provided in Table 6.

We then carry out a side-by-side comparison of the signals found in the activity search to the signals found in the RV search. In instances of overlapping periods between the two search results, we assert that the signal in the RVs is likely caused by stellar activity, rather than by the gravitational effects of an orbiting exoplanet. New RV signals that show evidence of this period overlap are reported in Table 4 as “Activity.” Instances where there is no overlap between the significant periods detected in the RV and S-index data sets are treated on a more individual basis. If the signal detected in the RV periodogram peak is well defined, the strength of the RV signal increases roughly monotonically with the number of observations, and we do not find a correlated activity signal, then we mark the signal as a “Candidate” in Table 4.

For less-obvious cases, where the RV signal is one of a set of numerous peaks clustered in a narrow period range but we find no corresponding signal in the activity data, we then consider the star’s spectral type and known activity history to decide whether the signal is likely to be due to activity. These cases are discussed in detail in each star’s subsection. We adopt the classification “source requiring confirmation” (SRC) for signals that do not yet have enough evidence to be classified as either Candidate or Activity. Signals marked as SRC in Table 4 require further follow-up analysis to determine their nature.

Results for HD 115617’s RVSearch analysis of the S-index data are shown in Figure 5. No significant detections are made, although we note that a strong signal is present at $P = 3995.5$ days in the periodogram. The strength of this signal is limited by the time span of observations for this target; we expect that given several more years’ worth of data, we would be able to state conclusively whether this signal is physical or not.

When compared with the radial velocity analysis in Figure 4, we see no overlapping periods between the three previously published planet signals and the S-index signal of growing strength in the periodogram. We thus affirm that the planets HD 115617 b, c, and d are not false signals caused by activity, but rather true exoplanets.

Table 6
S-index Signals Identified by RVSearch

ID	Period (days)	S-index Amp.	ID	Period (days)	S-index Amp.
HD 4628 I	3699 \pm 310	0.0161 \pm 0.0016	HD 85512 VIII	51.74 \pm 0.06	0.0152 \pm 0.0023
HD 14412 I	2312 \pm 73	0.013 \pm 0.0034	HD 100623 I	3741 \pm 93	0.0228 \pm 0.0025
HD 14412 II	5686 \pm 1600	0.0191 \pm 0.0079	HD 114613 I *	6722.80	...
HD 16160 I	4232 \pm 310	0.0417 \pm 0.0073	HD 125072 I	2989 \pm 100	0.098 \pm 0.011
HD 16160 II	3204 \pm 110	0.0253 \pm 0.0061	HD 125072 II	40.49 \pm 0.04	0.0336 \pm 0.0072
HD 20766 I *	1553.62	...	HD 131977 I	22.77 \pm 0.0	0.29 \pm 0.17
HD 22049 I	1086.7 \pm 7.1	0.0496 \pm 0.0048	HD 131977 II	3.88 \pm 0.0	0.192 \pm 0.065
HD 26965 I	3177 \pm 84	0.0206 \pm 0.0018	HD 131977 III	2.09 \pm 0.0	0.067 \pm 0.014
HD 30495 I	71.46 \pm 0.11	0.0303 \pm 0.0046	HD 146233 I	2812 \pm 290	0.0094 \pm 0.0032
HD 32147 I	3774 \pm 250	0.063 \pm 0.016	HD 146233 II	5272 \pm 1500	0.0116 \pm 0.0043
HD 32147 II	3204 \pm 310	0.043 \pm 0.016	HD 149661 I	1649 \pm 55	0.0423 \pm 0.0065
HD 32147 III	381.7 \pm 2.4	0.0093 \pm 0.0019	HD 149661 II	3874 \pm 1200	0.068 \pm 0.095
HD 32147 IV	343.2 \pm 2.7	0.0088 \pm 0.0018	HD 156026 I	378.9 \pm 2.2	0.05 \pm 0.01
HD 32147 V	95.6 \pm 0.24	0.005 \pm 0.0016	HD 160346 I	2975 \pm 600	0.0883 \pm 0.0094
HD 50281 I	2264 \pm 11	0.0748 \pm 0.0042	HD 160346 II	392.6 \pm 3.2	0.05 \pm 0.013
HD 50281 II	2102 \pm 12	0.065 \pm 0.005	HD 160346 III	7.96 \pm 0.01	0.0313 \pm 0.0093
HD 50281 III	139.42 \pm 0.05	0.0345 \pm 0.0039	HD 160346 IV	2.54 \pm 0.0	0.0177 \pm 0.0081
HD 50281 IV	12.48 \pm 0.0	0.0266 \pm 0.0039	HD 190248 I *	6810.18	...
HD 50281 V	16.5 \pm 0.0	0.022 \pm 0.0036	HD 192310 I	3817 \pm 60	0.0409 \pm 0.0013
HD 50281 VI	5.39 \pm 0.0	0.083 \pm 0.084	HD 192310 II	345.34 \pm 0.48	0.0093 \pm 0.0058
HD 50281 VII	2.7 \pm 0.0	0.0169 \pm 0.0047	HD 192310 III	44.01 \pm 0.11	0.0044 \pm 0.0011
HD 69830 I	3989 \pm 190	0.0146 \pm 0.0017	HD 192310 IV	432.6 \pm 3.4	0.015 \pm 0.0031
HD 69830 II	731 \pm 31	0.0038 \pm 0.0018	HD 192310 V	40.8 \pm 0.1	0.00383 \pm 0.00088
HD 69830 III	2530 \pm 180	0.008 \pm 0.002	HD 192310 VI	34.6 \pm 0.03	0.00521 \pm 0.00082
HD 72673 I	3217 \pm 200	0.0097 \pm 0.0016	HD 192310 VII	133.38 \pm 0.43	0.0069 \pm 0.0015
HD 75732 I	3801 \pm 130	0.0263 \pm 0.0015	HD 192310 VIII	33.73 \pm 0.05	0.00563 \pm 0.00097
HD 85512 I	4245 \pm 52	0.2106 \pm 0.0029	HD 207129 I *	1897.99	...
HD 85512 II	1294 \pm 14	0.0443 \pm 0.0035	HD 209100 I	2063 \pm 160	0.0588 \pm 0.0046
HD 85512 III	478.1 \pm 2.2	0.0324 \pm 0.0027	HD 209100 II	32.87 \pm 0.07	0.045 \pm 0.036
HD 85512 IV	322.05 \pm 0.85	0.0351 \pm 0.0032	HD 216803 I	3.89 \pm 0.0	0.066 \pm 0.008
HD 85512 V	45.52 \pm 0.04	0.0187 \pm 0.0021	HD 216803 II	4.08 \pm 0.0	0.051 \pm 0.016
HD 85512 VI	44.18 \pm 0.03	0.0188 \pm 0.0016	HD 216803 III	2.8 \pm 0.3	0.019 \pm 0.013
HD 85512 VII	104.3 \pm 0.15	0.022 \pm 0.0034			

Note. This table contains all significant S-index signals identified by RVSearch. We report the period and S-Index semiamplitude (in units of the Mt. Wilson S-index) of each signal. For signal interpretations, see each star’s individual discussion section. Signals with a “*” symbol designation failed to return well-constrained MCMC results, and so we instead report the MAP fits for their orbital periods.

(This table is available in machine-readable form.)

We include summary figures like Figure 5 from each star’s S-index data in the figure set. As referenced in Section 3.3, the UCLES spectrograph does not cover a wide enough wavelength range for the Ca II H & K lines to be observed simultaneously with the iodine region. For targets whose RV signals are largely driven by UCLES data, this causes the corresponding S-index activity analysis to be less definitive as a planet-vetting step. Instead, we use $EW_{H\alpha}$ measurements as an activity indicator for those stars.

4.4. Identification of Candidate Activity Signals in UCLES $EW_{H\alpha}$ Data

Stellar variability in the UCLES time series, which does not provide coverage of the Ca II H & K lines, was instead assessed using measurements of the EW of the $H\alpha$ absorption line ($EW_{H\alpha}$). Although the $H\alpha$ line is usually more informative for cooler, M dwarf stars (see, e.g., Robertson et al. 2013) it is still sensitive to some activity variations in hotter, Sun-like stars. We subjected the $EW_{H\alpha}$ time series to the same uninformed search process with RVSearch described for the S-index data above, again beginning with the removal of any $5 + \sigma$ outliers within each star’s data set. We run the cleaned time series

through RVSearch and record any significant periodicities so that they can be compared with the periods (if any) detected in that star’s RV data. We find that the long-term structure present in $EW_{H\alpha}$ is not sufficiently periodic to show up in the RVSearch ΔBIC periodograms, but caution that it may still obscure some lower-amplitude activity signals within the data. A list of all of the detected $EW_{H\alpha}$ signals is provided in Table 7.

Figure 6 shows an example summary figure from $H\alpha$ analysis of HD 115617. Our analysis returns three detections, only one of which we believe to be of astrophysical causes. The first signal, with $P = 346.3 \pm 1.9$ days, is extremely close to 1 yr. Just as with HARPS data, we expect to see yearly systematics within the $H\alpha$ data caused by the observing cadence. This signal is therefore attributed to systematics. $H\alpha$ signal II is close to the rotation period predicted for this star. Because we have a longer observation baseline and more-precise measurements than were used for previous rotation period estimates in the literature, we report $H\alpha$ signal II as an update to the stellar rotation period. $H\alpha$ signal III is most likely too long-period to be caused by differential rotation, though we discuss the possibility in detail in Section 5.14. It also does not

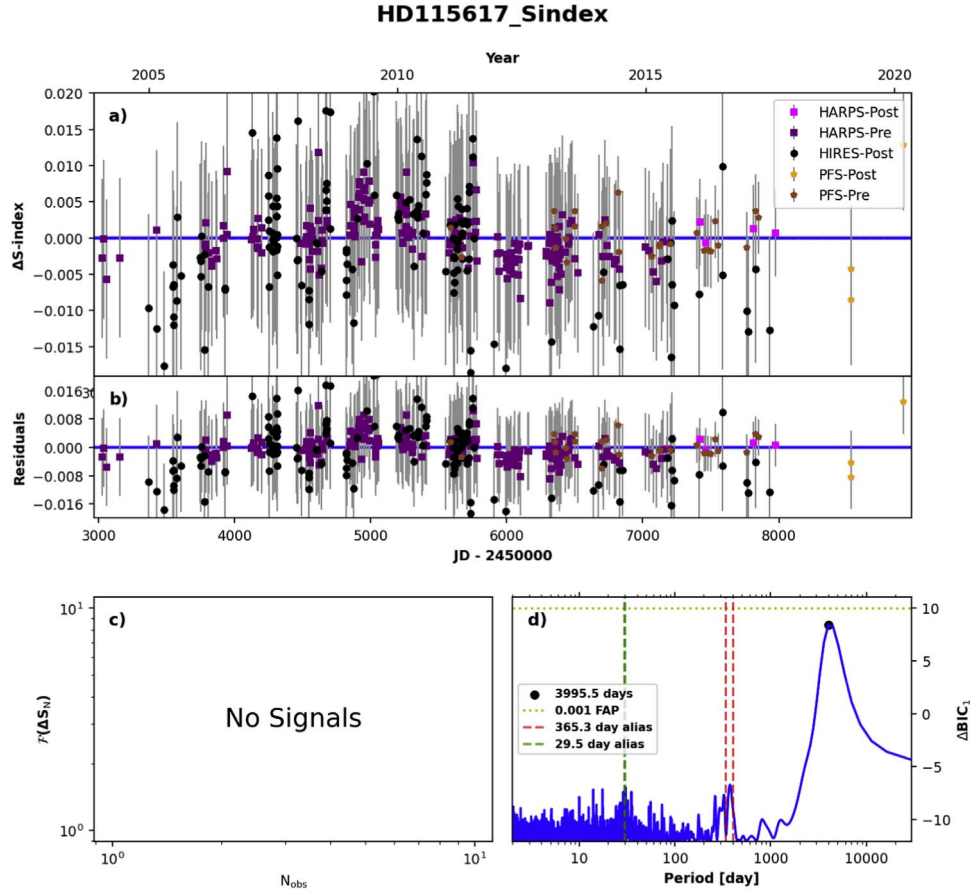


Figure 5. RVSearch results for the relative S-index measurements of HD 115617, following the same plot image structure as in Figure 4. Panel (a) shows the S-index time series with the best-fit model plotted behind them while panel (b) shows the S-index residuals. Panel (c) would present the phase-folded curves for any signals identified by RVSearch, but as can be seen in panel (d), no signals in the periodogram rise above the $\Delta\text{BIC} > 10$ requirement imposed on the S-index search (yellow horizontal dotted line). The red and green vertical dotted lines show the 1 month and 1 yr aliases of the tallest peak in the periodogram. The complete set of S-Index summary plots (49 figures) is available.

(The complete figure set (49 images) is available.)

Table 7
H α Signals Identified by RVSearch

ID	Period (days)	EW $_{\text{H}\alpha}$ Amp.	ID	Period (days)	EW $_{\text{H}\alpha}$ Amp.
HD 20794 I	2204 ± 16	0.0057 ± 0.0041	HD 115617 III	44.93 ± 0.07	0.00151 ± 0.00026
HD 20794 II	1753 ± 46	0.00283 ± 0.00095	HD 125072 I *	7137.76	0.00630685
HD 20807 I *	2859.91	0.00367565	HD 136352 I *	376.779	0.00913149
HD 23249 I	49.57 ± 0.1	0.00241 ± 0.00049	HD 136352 II *	7207.58	0.00537
HD 26965 I	43.5 ± 0.07	0.00316 ± 0.00054	HD 140901 I	7161 ± 2100	0.01205 ± 0.00082
HD 72673 I	341.2 ± 3.6	0.00508 ± 0.00076	HD 140901 II	19.99 ± 0.02	0.0036 ± 0.0007
HD 100623 I	3205 ± 130	0.01136 ± 0.00043	HD 160691 I *	$30888.2 [\text{peak} = 5293.7]$	0.00379764
HD 102365 I *	369.144	0.00752353	HD 160691 II *	362.611	0.00247693
HD 102365 II *	$18549.80 [\text{peak} = 7273.6]$	0.00322183	HD 190248 I	352.9 ± 1.5	0.00261 ± 0.00032
HD 102365 III *	49.68	0.00130454	HD 190248 II	1171 ± 36	0.0021 ± 0.00033
HD 114613 I *	$27460.5 [\text{peak} = 7652.9]$	0.00360532	HD 192310 I *	13621.7	0.00676791
HD 114613 II *	365.429	0.00211492	HD 192310 II *	363.678	0.00499708
HD 115617 I	346.3 ± 1.9	0.00376 ± 0.00027	HD 207129 I	5455 ± 1900	0.0036 ± 0.00036
HD 115617 II	24.63 ± 0.02	0.00152 ± 0.00025	HD 207129 II	1726 ± 71	0.00309 ± 0.00061

Note. This table contains all significant EW $_{\text{H}\alpha}$ signals identified by RVSearch. We report the period and EW $_{\text{H}\alpha}$ semiamplitude of each signal. For signal interpretations, see each star's individual discussion section. Systems with a "*" symbol designation failed to return well-constrained MCMC results, generally producing period uncertainties larger than the median period value, and so we instead report their MAP orbital solutions. In three cases, even the MAP period for the LPS is more than three times larger than the significant peak in the ΔBIC periodogram, and so we note the period of the original peak in brackets next to the MAP result.

(This table is available in machine-readable form.)

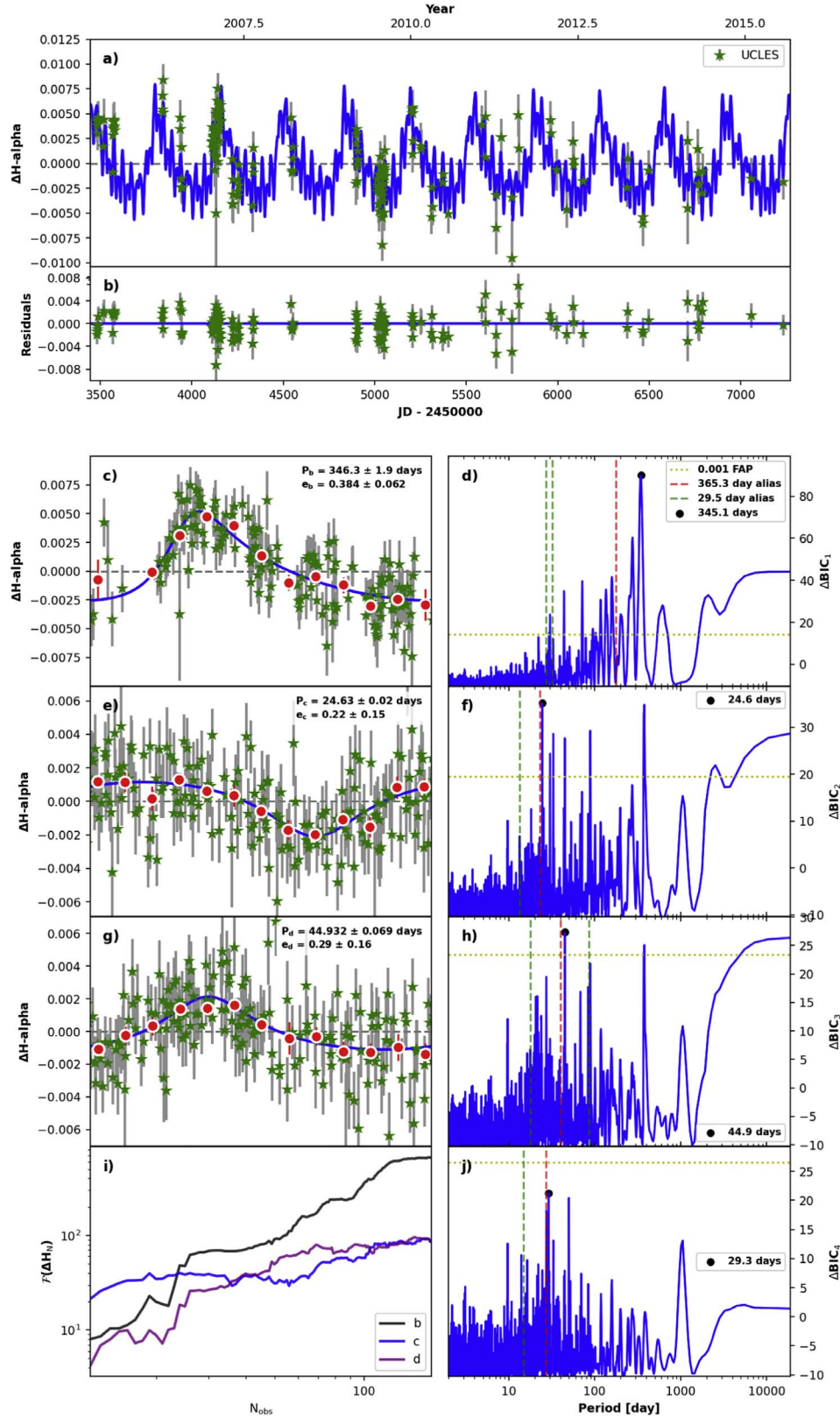


Figure 6. RVSearch results for the relative $\text{EW}_{\text{H}\alpha}$ measurements of HD 115617. Panel (a) shows the $\text{EW}_{\text{H}\alpha}$ time series with the best-fit model plotted behind them while panel (b) shows the $\text{EW}_{\text{H}\alpha}$ residuals. Panels (c), (e), and (g) show phase-folded curves for the signals identified by RVSearch, and panels (d), (f), and (h) show the periodograms associated with each signal, with the yellow horizontal dotted line marking the minimum ΔBIC for a 1% FAP significance, and the red and green vertical dotted lines showing the 1 month and 1 yr aliases of the tallest peak. Panel (i) shows the effective strength of each signal as a function of the number of observations, and panel (j) shows the residuals periodogram, indicating that no further signals are found in the data set. The complete set of $\text{H}\alpha$ activity summary plots (31 figures) is available.

(The complete figure set (31 images) is available.)

correspond to any peaks in RV or S-index data. We leave it to future, more in-depth studies of stellar activity to characterize the cause of this detection. The resulting summary figures for all 31 stars in this study observed by UCLES are available.

4.5. Injection and Recovery Analysis

After conducting and analyzing the uninformed RV and stellar activity indicator searches, we use RVSearch to execute an injection/recovery (I/R) analysis for each star’s residual RV data set. I/R analyses characterize the completeness of each star’s RV time series, quantifying which combinations of companion orbital periods and minimum masses we are currently sensitive to. The results of these I/R efforts make clear which types of planets we would expect to be able to detect in each star’s habitable zone given the current data sets, and can help to prioritize future RV surveys that aim to push sensitivity limits to lower-mass temperate planets. While we are primarily interested in the current RV sensitivity within each star’s Habitable Zone, we use this exercise as an opportunity to quantify our planet sensitivity across the entirety of the orbital period space covered by the combined RV data sets.

To accomplish this, 5000 synthetic planet signals are injected into the RV residuals of each star’s uninformed search results. These “planets” are assigned orbits and $m \sin i$ values drawn from log-uniform distributions. The corresponding periods and RV semiamplitudes span 2–10,000 days and $0.1\text{--}1000 \text{ m s}^{-1}$, respectively. Key properties of the data set, such as observation baseline, measurement values, and uncertainties, are preserved. Following the results of Kipping (2013), who examined the eccentricities of the population of RV detected exoplanets, the synthetic planets have eccentricities drawn from a β distribution. The same planet search algorithm used in the uninformed search is then run on these modified data sets to determine whether the injected signals can be recovered. This quantifies the planet sensitivity of the existing data, calculating the probability that a planet of a given $m \sin i$ and orbital period would be detected within the data.

A completeness contour plot is generated, demonstrating which regions of $m \sin i$ and orbital period space we are already sensitive to with the existing data. Figure 7 shows an example of a completeness contour plot for HD 115617. The three planets published in Vogt et al. (2010) and detected in the uninformed search stage of our analysis are depicted as black circles, and lie within the region of $m \sin i$ and semimajor axis space where we expect to be sensitive to Keplerian signals. The three regions of red points above the detected signals are remnants of the way the injection and recovery analysis works. Once an injected planet is recovered, it is compared with the already-fit model to see whether it would be in a reasonably stable orbit location compared with what has already detected. If the injected planet has the same orbit as an already-fit signal, RVSearch would not include the planet in the model due to orbital stability constraints, and so the injected signal is “not recovered.” This results in columns of nonrecovered injected planets that align with previously detected/removed Keplerian signals. The black circle corresponding to the final candidate detected in the uninformed search, the LPS that overlaps with a period in the activity search, is located in a regime with a much lower probability of detection. While the probability of detecting a synthetic at this period and semiamplitude is $<10\%$ according to the figure, the FAP of this LPS detected in

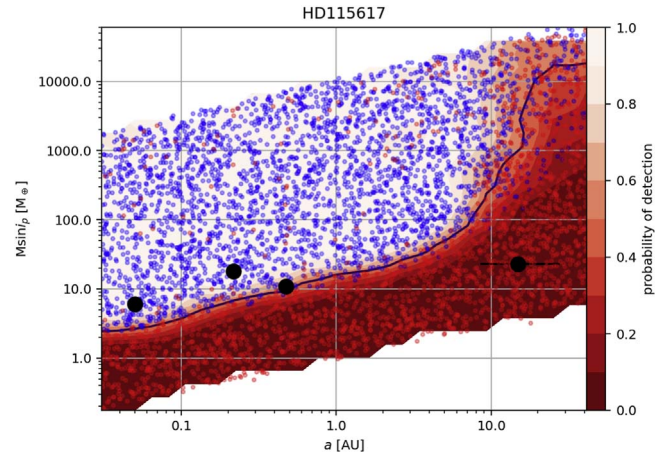


Figure 7. The RVSearch completeness contour plot for HD 115617. The large black dots indicate the periodic signals identified by RVSearch in the archival RV data (see Figure 4). The colored points depict the synthetic planets that were injected into the RV residuals—blue points represent planets that were successfully recovered, while red points represent those that were not recovered. The red contours display the probability of detection averaged over small regions of semimajor axis and $m \sin i$ space. The black line is the 50% detection probability contour. The complete set of injection and recovery analysis plots (49 figures) is available.

(The complete figure set (49 images) is available.)

the RV time series is $1.22\text{e-}10$, making it very unlikely to be a result of random fluctuations in the data.

Based on Figure 7, we would expect that for planets on a 0.1 au orbit that the existing RV data would be sensitive down to planet masses of $m \sin i = 2.6 M_{\oplus}$, a mass that could include terrestrial planets. But when considering planets on more temperate orbits near 0.914 au (this star’s EEID), the existing RV data is only sensitive to planets with masses of $\geq 15 M_{\oplus}$. Thus, efforts to detect an Earth analog around HD 115617 would not succeed with the existing data set. However, we can say with some confidence that if a $15 M_{\oplus}$ or larger planet were orbiting the star within its habitable zone, which would preclude the existence of an Earth-analog on a similar orbit, that we would already be able to detect it. Thus, at the moment, there is nothing to eliminate the possibility that HD 115617 could host an Earth-analog.

Table 12 describes the results of these injection and recovery tests. For each star in the set, we report which regions of $m \sin i$ and period space we are already sensitive to using the compiled archival data. We include minimum mass values for several semimajor axes, marking the limits of sensitivity for each star’s archival data set.

4.6. Speckle Imaging Analysis

In an attempt to identify any stellar companions from the speckle imaging observations obtained for some of the target stars, reconstructed images derived from the image reduction process were used (Horch et al. 2011; Howell et al. 2011). The distribution of all local maxima and minima in the background of the images as a function of separation was examined by drawing five concentric annuli each with width of $0''.2$ centered at radii of $0''.2$, $0''.4$, $0''.6$, $0''.8$, and $1''.0$ from the primary star. Standard deviations of these extrema from the mean background in each annulus were computed by averaging the values obtained from both maxima and minima. A 5σ detection limit, which is five times brighter than the mean background within

Table 8
Speckle Imaging Results

HD	Instrument	Date (UT)	Δm_{562} (0''1)	Δm_{562} (1''1)	Δm_{832} (0''1)	Δm_{832} (1''1)	EW _{Hα} Correlation
1581	Zorro	2020 Oct 29	4.31	7.50	4.43	7.95	N/A
20766	Zorro	2020 Oct 23	5.02	7.36	4.82	8.00	−0.48
20807	Zorro	2020 Oct 23	4.80	6.29	4.70	8.22	−0.17
140901	Zorro	2021 Jul 22	N/A	N/A	4.44	7.79	−0.68
146233	‘Alopeke	2021 Jun 27	4.66	6.56	4.74	9.33	−0.06
196761	‘Alopeke	2021 Jun 27	4.97	6.02	5.05	8.22	N/A

Note. All columns without N/A values present speckle imaging details, except for the last column, which includes Pearson coefficient values of correlation between UCLES RVs and H α EWs. Some UCLES RVs returned no significant signals when analyzed alone, and so no correlation is calculated, thus N/A. For HD 140901, no data was acquired for the blue channel due to alignment issue.

(This table is available in machine-readable form.)

each annulus, was then estimated. Any peak in the image that was above the 5σ limit at a specific angular separation was considered a companion candidate for further study. For the six targets that had speckle imaging observations, no such peaks were found, and therefore no stellar companions were identified. For these nondetections, 5σ limits derived for each annulus in terms of instrumental magnitude difference (Δm_i , where i is filter type) were used as a conservative upper limit above which stars should be detected, thus providing a constraint of the possible undetected low-mass companions nearby. Since Δm_i varies as a function of separation from the primary where at smaller separations Δm_i is slightly smaller, we reported the estimated Δm_i at both 0''1 and 1''1 from the primary in Table 8. Figure 8 summarizes these results for HD 1581.

5. Systems with Updated Parameters

In this section, we present results from targets for which we recover previously published planetary systems, stellar companions, and activity cycles. For the cases in which we have additional data or increased precision, we cite the current accepted values and report updates to these systems’ parameters. Table 9 contains former and new (this work) parameters for previously reported exoplanetary systems.

5.1. HD 13445 (GJ 86 A)

HD 13445 (GJ 86 A, HR 637, HIP 10138) is a nearby K1V star (Gray et al. 2006) at $d = 10.76$ pc ($\varpi = 92.9251 \pm 0.0461$ mas; Gaia Collaboration et al. 2021a). GJ 86A has both a known stellar companion (GJ 86B, WD 0208-510) and an exoplanet (GJ 86Ab, HD 13445b). Farihi et al. (2013) characterized the white dwarf companion GJ 86B and constrained its orbit—estimating a spectral type of DQ6, mass $= 0.59 \pm 0.01 M_\odot$, orbital period of $P = 120\text{--}481$ yr, and adopted system age of 2.5 Gyr.

We detect two signals in the RVs. One is the known exoplanet, and the other may be caused by the binary companion, but is too poorly constrained to say for certain. Butler et al. (2001) published the planet with a 15.76 day period. We derive orbital parameters for GJ 86Ab of $P_b = 15.764862 \pm 0.000043$ days, $K_b = 377.58 \pm 0.77$ m s $^{-1}$, and $e_b = 0.0485 \pm 0.0018$. The second significant detection has a peak in the periodogram with $P = 20,504$ days. Because this is much longer than the observation baseline for the target, the MCMC fit for the signal is not physical. We categorize this signal as an LPS and note that more data would be required to

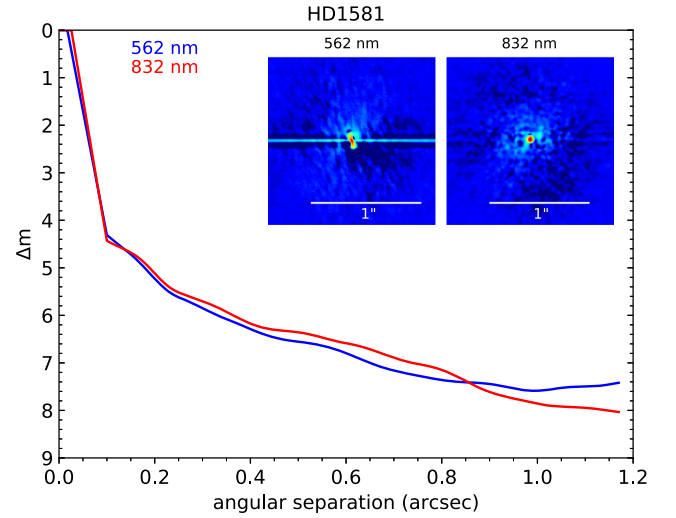


Figure 8. Speckle imaging analysis plot for HD 1581. Top right: the reconstructed Speckle images for HD 1581 for each wavelength. Larger plot: 5σ flux detection limit relative to image backgrounds, measured in concentric circular annuli from the center of the image. The complete set of speckle imaging analysis plots (6 figures) is available.

(The complete figure set (6 images) is available.)

constrain this signal further. Further discussion of the LPS category of detection can be found in Section 4.1.

Finally, we note that H α analysis shows strength in the periodogram at $P = 2001.7$ days, though the detection does not cross the FAP threshold.

5.2. HD 16160 (GJ 105 A)

HD 16160 (GJ 105 A, HR 753, HIP 12114) is a nearby K3V spectral standard star (Keenan & McNeil 1989) in a triple system, located at $d = 7.23$ pc ($\varpi = 138.2084 \pm 0.1436$ mas; Gaia Collaboration et al. 2018). The star is a 5.1 ± 1.1 Gyr old thin disk (Ramírez et al. 2012), low-activity ($\log R'_{\text{HK}} = -4.87$; Gomes da Silva et al. 2021) star with a magnetic activity cycle of $P_{\text{cyc}} \simeq 12.18$ yr (Willamo et al. 2020) or 12.7 ± 0.11 yr (Boro Saikia et al. 2018). From analysis of the Mt. Wilson survey data, Donahue et al. (1996) reported an average rotation period of $P_{\text{rot}} = 48.0$ days over five seasons, with individual seasonal rotation periods ranging from 42.2–51.5 days (i.e., pronounced differential rotation).

GJ 105 A has a faint M7V companion GJ 105 C (HD 16160B, WDS J02361+0653B) observed at separations

Table 9
Updated Parameters for Previously Reported Exoplanets

ID ...	$P(\text{new})$ (days)	$K(\text{new})$ (m s ⁻¹)	$e(\text{new})$...	$P(\text{old})$ (days)	$K(\text{old})$ (m s ⁻¹)	$e(\text{old})$...	References ...
HD 13445 b ^a	15.764862 ± 04.3e-05	377.58 ± 0.77	0.0485 ± 0.0018	15.76491 ± 0.00039	376.7 ± 2.9	0.04 ± 0.01	Butler et al. (2006)
HD 20794 b	18.305 ± 0.0052	0.807 ± 0.089	0.17 ± 0.11	18.33 ^{+0.01} _{-0.02}	0.81 ^{+0.0} _{-0.24}	0.27 ^{+0.04} _{-0.22}	Feng et al. (2017b)
HD 20794 d	89.766 ± 0.085	0.86 ± 0.12	0.27 ± 0.11	88.90 ^{+0.37} _{-0.41}	0.60 ^{+0.10} _{-0.18}	0.25 ^{+0.16} _{-0.21}	Feng et al. (2017b)
HD 22049 b	2832 ± 120	11.1 ± 1.2	0.09 ± 0.08	2690 ± 30	...	0.07 ^{+0.06} _{-0.05}	Mawet et al. (2019)
HD 39091 b	2089.05 ± 0.46	196.5 ± 0.6	0.6428 ± 0.0017	2088.33 ± 0.34	192.99 ± 0.38	0.6396 ± 0.0009	Hatzes et al. (2022)
HD 39091 d	125.58 ± 0.27	2.16 ± 0.42	0.16 ± 0.15	124.64 ^{+0.48} _{-0.52}	1.68 ± 0.17	0.22 ± 0.079	Hatzes et al. (2022)
HD 69830 b	8.66897 ± 0.00028	3.4 ± 0.1	0.128 ± 0.028	8.667 ± 0.003	3.51 ± 0.15	0.10 ± 0.04	Lovis et al. (2006)
HD 69830c	31.6158 ± 0.0051	2.6 ± 0.1	0.03 ± 0.027	31.56 ± 0.04	2.66 ± 0.16	0.13 ± 0.06	Lovis et al. (2006)
HD 69830d	201.4 ± 0.4	1.5 ± 0.1	0.08 ± 0.071	197 ± 3	2.20 ± 0.19	0.07 ± 0.07	Lovis et al. (2006)
HD 75732 b ^a	14.65157 ± 0.00015	70.39 ± 0.37	0.0069 ± 0.0047	14.6516 ± 0.0001	71.37 ± 0.21	0.0 ± 0.0	Bourrier et al. (2018)
HD 75732 c ^a	44.39 ± 0.01	9.95 ± 0.37	0.22 ± 0.041	44.3989 ^{+0.0042} _{-0.0043}	9.890 ± 0.220	0.03 ± 0.02	Bourrier et al. (2018)
HD 75732 e ^a	0.736546 ± 5e-06	6.26 ± 0.34	0.039 ± 0.035	0.7365474 ^{+0.0000013} _{-0.0000014}	6.02 ^{+0.24} _{-0.23}	0.05 ± 0.03	Bourrier et al. (2018)
HD 75732 f ^a	260.88 ± 0.36	5.68 ± 0.48	0.585 ± 0.057	259.88 ± 0.29	5.14 ^{+0.26} _{-0.25}	0.080 ^{+0.05} _{-0.04}	Bourrier et al. (2018)
HD 102365 b	121.3 ± 0.25	1.38 ± 0.23	0.28 ± 0.15	122.1 ± 0.3	2.30 ± 0.35	0.34 ± 0.14	Tinney et al. (2011)
HD 115617 b ^a	4.21498 ± 0.00014	2.47 ± 0.11	0.033 ± 0.029	4.215 ± 0.0006	2.12 ± 0.23	0.12 ± 0.11	Vogt et al. (2010)
HD 115617 c ^a	38.079 ± 0.008	3.56 ± 0.12	0.026 ± 0.023	38.021 ± 0.034	3.62 ± 0.23	0.14 ± 0.06	Vogt et al. (2010)
HD 115617 d ^a	123.2 ± 0.2	1.47 ± 0.17	0.15 ± 0.11	123.01 ± 0.55	3.25 ± 0.39	0.35 ± 0.09	Vogt et al. (2010)
HD 136352 b	11.5767 ± 0.0015	1.65 ± 0.11	0.05 ± 0.045	11.5824 ^{+0.0024} _{-0.0025}	1.59 ± 0.13	0.14 ± 0.08	Udry et al. (2019)
HD 136352c	27.5845 ± 0.0064	2.49 ± 0.12	0.041 ± 0.036	27.5821 ^{+0.0089} _{-0.0086}	2.65 ± 0.14	0.04 ^{+0.05} _{-0.03}	Udry et al. (2019)
HD 136352 d	107.5 ± 0.14	1.44 ± 0.12	0.072 ± 0.061	107.5983 ^{+0.2796} _{-0.2669}	1.35 ± 0.15	0.90 ^{+0.1} _{-0.07}	Udry et al. (2019)
HD 160346	83.7286 ± 0.0005	5690.3 ± 2.3	0.2048 ± 0.0003	83.7140	...	—	Halbwachs et al. (2018)
HD 160691 b	644.93 ± 0.28	35.7 ± 0.2	0.0499 ± 0.0082	645.3 ± 0.3	336.1 ± 0.2	0.036 ± 0.007	Benedict et al. (2022)
HD 160691 c	9.6394 ± 0.0008	2.8 ± 0.2	0.132 ± 0.069	9.6392 ± 0.0006	2.94 ± 0.17	0.16 ± 0.06	Benedict et al. (2022)
HD 160691 d	308.4 ± 0.23	12.7 ± 0.3	0.074 ± 0.016	307.9 ± 0.3	12.23 ± 0.27	0.091 ± 0.014	Benedict et al. (2022)
HD 160691 e	4035 ± 21	22.25 ± 0.24	0.026 ± 0.013	3947 ± 23	22.18 ± 0.25	0.022 ± 0.012	Benedict et al. (2022)
HD 192310 b ^a	74.278 ± 0.035	2.484 ± 0.098	0.032 ± 0.027	74.72 ± 0.1	3.00 ± 0.12	0.13 ± 0.04	Pepe et al. (2011)
HD 192310 c ^a	549.1 ± 4.5	1.3 ± 0.1	0.078 ± 0.073	525.8 ± 9.2	2.27 ± 0.28	0.32 ± 0.11	Pepe et al. (2011)

Note.

^a Additional signals detected in our best-fit solution; see Table 4 for additional information.

(This table is available in machine-readable form.)

between $1''.7$ and $3''.3$ (Golimowski et al. 1995, 2000; Mason et al. 2001),³⁵ and the M4.0V star GJ 105 B star on a very wide orbit at $164''$ separation (van Maanen 1938; Mann et al. 2015). Astrometric perturbations attributed to a low-mass stellar companion to GJ 105 A (BD+6° 398) were first reported by Lippincott (1973), who measured photographic plate positions from the Sproul astrometric program taken between 1937 and 1968, estimated the orbit to have $P = 50$ yr and $e = 0.6$, and predicted the companion to be a $0.10 M_{\odot}$ star of type M6.

Golimowski et al. (2000) concluded that the companion C first observed in 1993 with the Palomar 60" Adaptive Optics Coronagraph (Golimowski et al. 1995) was consistent with (1) the astrometric perturbations with ~ 50 – 60 yr periodicities reported by Lippincott (1973; and later refined by Ianna 1992 and Heintz & Cantor 1994), and (2) the $11 \text{ m s}^{-1} \text{ yr}^{-1}$ RV trend observed during the 1990s by Cumming et al. (1999). Ianna (1992) analyzed photographic plate positions for GJ 105 A between 1915 and 1992 and estimated $P = 59.5$ yr, astrometric amplitude $\alpha = 0''.293$, $e = 0.35$, and companion mass $M_C = 0.13 M_{\odot}$. Our analysis of the archival RV data with RVSearch yields an LPS with $P = 22999 \pm 1200$ days (63.0 ± 3.3 yr), $K = 702.5 \pm 2.9 \text{ m s}^{-1}$, and $e = 0.6075 \pm 0.0092$, which is reasonable for the orbit of GJ 105 C.

These values are not far from the most recent astrometric-only orbital analysis from Heintz & Cantor (1994), who estimated $P = 61$ yr, $e = 0.67$, and $i = 49^\circ$ (consistent with companion mass $M_C = 0.10 M_{\odot}$). They also align well with the values reported in the recent work of Rosenthal et al. (2021), who found $a = 16.37 \pm 0.28$ au and $e = 0.6427^{+0.0038}_{-0.0039}$. Using the stellar mass adopted in this paper, we calculate the period to be approximately $P = 77$ yr. This also aligns with the signal we recover, though our detection is significantly less well constrained than in other works. A joint analysis of the RV, astrometric, and imaging data over the past century could yield stronger orbital constraints and a more accurate dynamical mass estimate, but is beyond the scope of this study.

Analysis of S-indices using RVSearch returns two significant activity detections, with parameters: (i) $P_I = 4232 \pm 310$ days, $e_I = 0.17 \pm 0.055$ and (ii) $P_{II} = 3204 \pm 110$ days, $e_{II} = 0.413 \pm 0.092$. The first of these aligns fairly well with the magnetic activity cycle reported by Willamo et al. (2020). We recommend a more in-depth study of this star's activity to fully characterize the sources of these periodic signals in the S-indices.

5.3. HD 20794 (82 Eri)

82 Eri (GJ 139, HD 20794, HR 1008, HIP 15510) is a G8V star (Gray et al. 2006) at $d = 6.00$ pc ($\varpi = 166.5242 \pm 0.0784$ mas; Gaia Collaboration et al. 2021a). The star is somewhat cooler than the Sun ($T_{\text{eff}} = 5398$ K), metal-poor ($[\text{Fe}/\text{H}] = -0.41$; Tsantaki et al. 2013), and very inactive ($\log R'_{\text{HK}} = -5.025$; Lovis et al. 2011). Lovis et al. (2011) reported a magnetic activity cycle of $P_{\text{cyc}} = 751^{+290}_{-25}$ days ($2.06^{+0.79}_{-0.07}$ yr) based on 197 $\log R'_{\text{HK}}$ measurements over a span of 2694 days. The star was reported to host three planets by Pepe et al. (2011), with orbital periods of $P_b = 18.1$ days, $P_c = 40.1$ days, and $P_d = 90.3$ days, based upon their analysis of 173 HARPS RV data points taken between 2003 and 2011.

A reanalysis of the system was published in 2017, which made use of an updated HARPS data set containing 713 RV epochs obtained between 2003 and 2013 (Feng et al. 2017b). The Feng et al. (2017b) results confirm the Keplerian nature of the 18 and 90 day signals put forth in Pepe et al. (2011) and identify two additional planet candidates with orbital periods of 147 and 330 days. They find only weak evidence of the ~ 40 days signal reported by Pepe et al. (2011), however, and assert that more data are necessary to determine the nature of this signal.

Our data set for HD 20794 contains 763 HARPS epochs, spanning 2003–2016, along with 549 UCLES points, and 77 PFS points. Running this combined RV data set through RVSearch, we confirm HD 20794 b ($P_b = 18.305 \pm 0.0052$ days, $K_b = 0.807 \pm 0.089 \text{ m s}^{-1}$, $e_b = 0.17 \pm 0.11$) and HD 20794 d ($P_d = 89.766 \pm 0.085$ days, $K_d = 0.86 \pm 0.12 \text{ m s}^{-1}$, $e_d = 0.27 \pm 0.11$) in Tables 9 and 4.

Similarly to Feng et al. (2017b), we do not register a detection of the ~ 40 days signal attributed to HD 20794c, though we note that the residuals periodogram shows significant power for a signal at 40.2 days, which likely corresponds to the reported 40.1 day period of HD 20794c in Pepe et al. (2011). If the signal were Keplerian in nature, however, we would expect its statistical significance to increase as more RV data points are added to the analysis. This is especially true for a star that exhibits the low levels of RV scatter we see in the HD 20794 RVs, where $\text{rms} = 1.99 \text{ m s}^{-1}$ and 1.00 m s^{-1} for HARPS and PFS, respectively.

Another possibility is that the 40 day signal is tied to stellar variability. The star's low chromospheric activity ($\log R'_{\text{HK}} = -5.03$) is consistent with a rotation period of $P_{\text{rot}} > 34$ days for a star of its color (using the activity-rotation relations of Mamajek & Hillenbrand 2008), and so rotational modulation at a period of roughly 40 days would not be surprising. Yet applying RVSearch to the star's assembled S-index data does not reveal significant power at or near a 40 day period. We also do not significantly detect planet candidates e, f, or g, as reported by Feng et al. (2017b). There is another peak in the RV residuals periodogram close to 330 days, the orbital period of candidate f, but similarly to the 40 day signal, it does not cross the threshold of being detected by RVSearch. Given the more sophisticated treatment of stellar variability and correlated noise in the that paper, however, we do not view our nondetections as a refutation of these candidates.

S-index analysis returns no significant signals, but analysis of $H\alpha$ in the UCLES data yields two significant detections: (i) $P_I = 2204 \pm 16$ days, $e_I = 0.886 \pm 0.049$ and (ii) $P_{II} = 1753 \pm 46$ days, $e_{II} = 0.68 \pm 0.15$. The high eccentricities fit to these signals are cause for skepticism regarding their exactness, but we regard them as good evidence for the existence of an approximately 7–8 yr activity cycle for this star.

5.4. HD 22049 (ϵ Eri)

ϵ Eri (GJ 144, HD 22049, HR 1084, HIP 16537, Ran) is a young, active K2V spectral standard star (Keenan & McNeil 1989) at $d = 3.22$ pc ($\varpi = 310.5773 \pm 0.1355$ mas; Gaia Collaboration et al. 2021a) with a candidate planet and debris disks (Mawet et al. 2019). Analysis of the Mt. Wilson Ca II H & K data of ϵ Eri by Donahue et al. (1996) found strong evidence for differential rotation, with season-averaged rotation periods ranging from $P_{\text{rot}} = 11.04$ – 12.18 days over nine seasons, with an average $P_{\text{rot}} = 11.68$ days. An archival

³⁵ References to the Washington Double Star (WDS) catalog (Mason et al. 2001) are actually referring to the regularly updated WDS table at Vizier (<https://cdsarc.unistra.fr/viz-bin/cat/B/wds>).

analysis of 45 yr of chromospheric activity data by Metcalfe et al. (2013) identified two prominent activity cycles for ϵ Eri at $P_{\text{cyc1}} = 2.95 \pm 0.03$ yr and $P_{\text{cyc2}} = 12.7 \pm 0.3$ yr, at approximately $0.68\times$ and $2.94\times$ planet orbital period reported by Mawet et al. (2019).

We recover the one confirmed planet ($P = 2690 \pm 30$ d $= 7.365 \pm 0.082$ yr; Mawet et al. 2019), but with a less certain period of $P_b = 2832 \pm 120$ days (7.76 ± 0.33 yr), and semiamplitude and eccentricity $K_b = 11.1 \pm 1.2$ m s $^{-1}$, $e_b = 0.09 \pm 0.08$. The periodogram residuals show a signal at 12.4 days, which agrees well with rotation periods reported by Donahue et al. (1996).

We detect one S-index activity signal with parameters $P_I = 1086.7 \pm 7.1$ days (2.98 ± 0.02 yr) and $e_I = 0.268 \pm 0.081$. This agrees with the 2.95 yr activity cycle reported by Mawet et al. (2019).

We note that we do not detect the false-positive $P = 773.4^{+4.7}_{-4.8}$ days signal reported by Rosenthal et al. (2021).

5.5. HD 26965 (40 Eri A)

40 Eri A (σ^2 Eri A, GJ 166 A, HD 26965, HR 1325, Keid) is a famous nearby ($d = 4.98$ pc, $\varpi = 200.62 \pm 0.23$ mas; van Leeuwen 2007) K0.5V standard star (Keenan & McNeil 1989) in a triple system with a white dwarf (B) and M dwarf (C) component. From time-series analysis of chromospheric activity data from the Mt. Wilson survey, the rotation period of the star has been previously measured to be 43 days (Baliunas et al. 1996) and 42 days (Frick et al. 2004), and *predicted* rotation periods (based on $\log R'_{\text{HK}}$ values and correlations with rotation for other cool dwarfs) have been reported to be 37.1 days (Saar & Osten 1997), 42.2 ± 4.4 days (Lovis et al. 2011), and 43 days (Isaacson & Fischer 2010). Long-term monitoring of Ca H & K emission from 40 Eri A has revealed a magnetic activity period with measured period $P_{\text{cyc}} = 10.1 \pm 0.1$ yr (Baliunas et al. 1995), 10.4 yr (3800 days; Frick et al. 2004), $9.18^{+2.20}_{-1.48}$ yr (Lovis et al. 2011), and $10(9.57 - 10.5)$ yr (Oláh et al. 2016), or 10.23 ± 0.07 yr (Boro Saikia et al. 2018).

Díaz et al. (2018) presented an extensive analysis of ~ 1100 spectra taken using HIRES, PFS, CHIRON, and HARPS, and reported a strong signal at $P = 42.364 \pm 0.015$ days, $K = 1.59 \pm 0.15$ m s $^{-1}$, and $e = 0.017 \pm 0.046$, but found it challenging to distinguish this signal from the star's rotation. Shortly after, Ma et al. (2018) conducted a reanalysis of the Díaz et al. (2018) data combined with 133 new spectroscopic observations taken with the TOU instrument. Ma et al. (2018) found that while there were signals in the star's activity indices at 41.2 ± 0.9 days and 39.2 ± 0.7 days likely corresponding to (differential) stellar rotation, the well-defined $P = 42.38$ day signal persisted over the seasons and between activity states—concluding that the signal was most likely due to a planet. Rosenthal et al. (2021) reported a signal at $P = 42.305^{+0.015}_{-0.019}$ days ($K = 1.82^{+0.43}_{-0.31}$ m s $^{-1}$) and considered it a false positive attributed to the star's rotation, and another longer signal at $P = 3560^{+200}_{-580}$ days ($K = 1.89^{+0.37}_{-0.32}$ m s $^{-1}$) attributed to long-period magnetic activity cycle.

We detect a strong significant RV signal with $P_I = 42.303 \pm 0.025$ days, $K_I = 1.40 \pm 0.22$ m s $^{-1}$, and $e_I = 0.37 \pm 0.17$, very similar to that reported previously by Díaz et al. (2018) and Ma et al. (2018). Analysis of H α data for this target returns a well-correlated detection with $P = 43.504 \pm 0.066$ days, $e = 0.37 \pm 0.18$. The extreme proximity of these

two detections leads us to classify this RV detection conclusively as activity. Additionally, we detect RV signals with (i) $P_{\text{II}} = 37.33 \pm 0.02$ days, $K_{\text{II}} = 1.17 \pm 0.19$ m s $^{-1}$, $e_{\text{II}} = 0.14 \pm 0.12$, and (ii) $P_{\text{III}} = 367.9 \pm 3.1$ days, $K_{\text{III}} = 1.63 \pm 0.88$ m s $^{-1}$, $e_{\text{III}} = 0.46 \pm 0.27$. Looking closely at the periodogram, we note that the 37 day period signal is extremely close to the yearly alias of the 42 day signal, and report it as such. The 365 day signal is likely driven by the window function of this star as the phase-folded fit makes clear that a significant ($>25\%$) portion of the orbital phase space is unpopulated due to seasonal observing constraints. We therefore classify this as a false-positive signal.

In the S-index activity analysis, we find a signal with $P_I = 3177 \pm 84$ days (8.70 ± 0.23 yr) and $e_I = 0.059 \pm 0.051$, which agrees well with Rosenthal et al. (2021) and which we report as an update to the 10 yr magnetic cycles previously published.

5.6. HD 39091 (π Men)

π Men (GJ 9189, HD 39091, HR 222, HIP 26394) is a G0V spectral type star (Gray et al. 2006) at $d = 18.28$ pc ($\varpi = 54.6825 \pm 0.0354$ mas; Gaia Collaboration et al. 2021a). π Men has three published planets. π Men b was first published in Jones et al. (2002), and was discovered using RV data from the UCLES instrument. We recover π Men b in our RV data with $P_b = 2089.05 \pm 0.46$ days, $K_b = 196.5 \pm 0.6$ m s $^{-1}$, and $e_b = 0.6428 \pm 0.0017$. These parameters are comparable to recent estimates by Huang et al. (2018), Gandolfi et al. (2018), and Xuan & Wyatt (2020). Our analysis includes newly released PFS data, building upon the HARPS + UCLES orbital fits performed in the previous works, and so we report our detection as an update to the orbital parameters of π Men b.

π Men c was the first new transiting planet discovered by NASA's Transiting Exoplanet Survey Satellite (TESS; Huang et al. 2018). The planet was not robustly detected by RVSearch's uninformed search of the RVs, although there is a well-defined peak in the residuals periodogram at the expected period of $P_c = 6.2$ days.

π Men d is a recently detected, sub-Neptune-mass planet candidate reported to have $P_d = 124.64^{+0.48}_{-0.52}$ days, $K_d = 1.68 \pm 0.17$ m s $^{-1}$, and $e_d = 0.22 \pm 0.079$ (Hatzes et al. 2022). These parameters are driven largely by observations taken as part of intensive HARPS and ESPRESSO observing campaigns, the data for which is not included in this analysis.

We detect a similar signal, consistent to within 1.5σ on all parameters, albeit with larger uncertainties on the planet's RV semiamplitude. Our best-fit results for this third signal are $P_d = 125.58 \pm 0.27$ days, $K_d = 2.16 \pm 0.42$ m s $^{-1}$, and $e_d = 0.16 \pm 0.15$.

Activity analysis of both S-index and H α data for this target recovers no significant signals.

5.7. HD 43834 (α Men)

α Men (GJ 231, HD 43834, HR 2261, HIP 29271) is a G7V star (Gray et al. 2006) at $d = 10.21$ pc ($\varpi = 97.9158 \pm 0.0573$ mas; Gaia Collaboration et al. 2021a). Eggenberger et al. (2007) reported a mid-M dwarf companion at $3''$ (projected separation 31.7 au). Tokovinin (2014) estimates the companion's mass to be $0.14 M_{\odot}$ and the orbital period to be $\sim 58,900$ days (~ 161 yr).

Our analysis of RVs returns one significant signal, with parameters $P = 359.5 \pm 1.2$ days, $K = 5.5 \pm 1.3$ m s⁻¹, and $e = 0.40 \pm 0.14$. The peak is very well defined, and well above the ΔBIC detection threshold, though its proximity to a 1 yr signal introduces concerns about whether it might be driven by the windowing effects of seasonal observing. However, the HARPS S-index and UCLES H α analysis for this star do not reveal any significant signals. We therefore report this signal as a Candidate, leaving it to future efforts to perform the more detailed analysis of this signal required to determine whether it is truly Keplerian in nature. Additionally, we note the existence of a second LPS in the RVs at $P = 3694.7$ days that falls just below the detection threshold.

5.8. HD 69830 (GJ 302)

HD 69830 (GJ 302, HR 3259, HIP 40693) is a well-studied star of type G8+V (Gray et al. 2006) at distance $d = 12.58$ pc ($\varpi = 79.4953 \pm 0.0400$ mas; Gaia Collaboration et al. 2021a), famous for hosting a planetary system of three Neptunes (Lovis et al. 2006) and a dusty debris disk (Beichman et al. 2005). The stellar rotation period has been estimated by Isaacson & Fischer (2010) to be 42 days, while Simpson et al. (2010) reported 35.1 ± 0.8 days.

With 1515 additional RV measurements since Lovis et al. (2006), we recover all three of the same planets with slightly different periods and amplitudes (see Table 9 for a full comparison). For HD 69830 b, we report $P_b = 8.66897 \pm 0.00028$ days, $K_b = 3.4 \pm 0.1$ m s⁻¹, and $e = 0.128 \pm 0.028$. For HD 69830c: $P_c = 31.6158 \pm 0.0051$ days, $K_c = 2.6 \pm 0.1$ m s⁻¹, and $e_c = 0.030 \pm 0.027$, and for HD 69830 d: $P_d = 201.4 \pm 0.4$ days, $K_d = 1.5 \pm 0.1$ m s⁻¹, and $e_d = 0.080 \pm 0.071$. The uncertainties on our derived orbital periods are slightly smaller than those recently reported by Rosenthal et al. (2021), who used data from HIRES and the APF but not the other instruments included here, and appear to be the most precise yet reported.

Rosenthal et al. (2021) found two false positives in their analysis with periods of 201 and 382 days, which they attribute to systematic errors. However, the $P = 201$ day signal is in fact a detection of Lovis et al.’s (2006) planet d, and its inclusion in Rosenthal et al.’s (2021) false-positive table (Table 7) is a typo. We do not recover the 382 day false positive reported by Rosenthal et al. (2021), but our inclusion of multiple instruments’ data that are not included in Rosenthal et al. (2021) may dilute individual facilities’ systematics.

Additionally, we recover three significant signals in the S-index activity analysis. S-index signal I has $P_I = 3989 \pm 190$ days (10.93 ± 0.52 yr), which is similar to the Sun’s own 11 yr activity cycle (e.g., Hathaway 2015). Lovis et al. (2011) reported a poorly constrained activity cycle period of $P_{\text{cyc}} = 5865^{+\infty}_{-1235}$ days, which is 1.46σ longer than our measured activity signal I, but they are likely detections of the same long-term magnetic activity cycle. We report S-index activity signal I as a magnetic activity cycle. S-index activity signal II has $P_{II} = 731 \pm 31$ days (2.00 ± 0.08 yr), which we note is almost twice the expected HARPS yearly systematic. Attribution of this signal to an HARPS systematic is further supported by the complete lack of corresponding signal in the UCLES H α analysis for this target, which not only returns no significant detections but shows almost no strength in the periodogram at this period.

Finally, S-index activity signal III has $P_{III} = 2530 \pm 180$ days (6.93 ± 0.49 yr). This may be another magnetic activity cycle, though we note that there appears to be a minimum in the H α periodogram at this period. We recommend further investigation by future work to understand this signal.

Comparison of the star’s rotation period and cycle periods with other nearby Sun-like stars in Figure 9 of Boro Saikia et al. (2018) indicate that HD 69830 may be a rare case of a slow-rotating star with two detected activity cycles (10.93 ± 0.52 yr and 6.93 ± 0.49 yr, both of which are near the “inactive branch” locus in P_{rot} versus P_{cyc} space).³⁶

5.9. HD 75732 (55 Cnc)

55 Cnc (ρ^1 Cnc, GJ 324 A, HD 75732, HR 3522, HIP 43587, Copernicus) is a famous, K0IV-V (Gray et al. 2003) exoplanet host star at $d = 12.58$ pc ($\varpi = 79.4482 \pm 0.0429$ mas; Gaia Collaboration et al. 2021a). 55 Cnc also has a wide separation ($85''$, ~ 1060 au) low-mass stellar companion 55 Cnc B. Bourrier et al. (2018) presented an extensive review of the 55 Cnc system and its five exoplanets (see also, e.g., Fischer et al. 2008; Endl et al. 2012; Fischer 2018). Bourrier et al.’s (2018) analysis contains 1552 RV measurements from a combination of both first-generation and more modern precise RV spectrographs spanning 25 yr. In comparison, this work includes only modern precise RV data sets and contains 837 RV measurements taken over 18 yr. Our analysis does, however, have longer HIRES and APF baselines than present in Bourrier et al. (2018). We recover signals corresponding to all five reported planets around 55 Cnc and report updates to the parameters of planets b, c, e, and f in Table 4.

Our detection of the long-period planet 55 Cnc d suffers from our more limited observational baseline and the months of time between the HIRES -Pre and -Post data sets. The ΔBIC periodogram peak suggests a 4421 day period, which is notably shorter than the $P_d = 5574.2^{+93.8}_{-88.6}$ result from Bourrier et al. (2018). After fitting the full system, RVSearch arrives at a best-fit model of $P_d = 14951 \pm 5100$ days, $K_d = 54 \pm 5$ m s⁻¹, and $e_d = 0.515 \pm 0.086$ for this LPS. This overly long, poorly constrained result exhibits similar behavior to the other “LPS” signals in this work due to the lack of full orbital phase coverage. Due to the period of the initial periodogram peak, we attribute this signal to 55 Cnc d, but we do not report this as an updated orbital parameter result.

Baluev (2015) reported an activity cycle for 55 Cnc of period $P_{\text{cyc}} = 12.6^{+2.5}_{-1.0}$ yr, with a prediction that an activity minimum would occur around 2014–2015. This correlates with our S-index detection at $P = 3801 \pm 130$ days (10.4 ± 0.36 yr), so we report this signal as an update to the previously published activity cycle. The activity cycle prediction from Baluev (2015) also does not align with the signal reported in Rosenthal et al. (2021).

5.10. HD 85512 (GJ 370)

HD 85512 (GJ 370, HIP 48331) is a nearby, somewhat metal-poor ($[\text{Fe}/\text{H}] = -0.26$) (Tsantaki et al. 2013), inactive ($\log R_{\text{HK}} = -4.976$; Costes et al. 2021) K6V(k) star (Gray et al. 2006) at $d = 11.28$ pc ($\varpi = 461.446$ mas; Gaia Collaboration et al. 2021a). The star has one previously reported planet at

³⁶ A similar example from Boro Saikia et al. (2018) is the K2V star HD 149661, with activity cycles of 15.3 ± 0.4 and 7.7 ± 0.12 yr (see also Saar & Brandenburg 1999).

$P_b = 58.43 \pm 0.13$ days (Pepe et al. 2011), recovered through RV analysis of 185 HARPS data points.

Our RVSearch analysis, run on an additional 1127 data points, does *not* detect a 58 day signal, but rather a shorter-period signal with parameters: $P_b = 51.195 \pm 0.073$ d, $K_b = 0.438 \pm 0.079$ m s⁻¹, and $e_b = 0.3 \pm 0.19$. This change, from $P_b = 58.43 \pm 0.13$ days in Pepe et al. (2011) to $P_b = 51.195 \pm 0.073$ days in this study amounts to a 48σ difference, well beyond any expected planetary orbit refinement. The reported amplitudes are also somewhat inconsistent, with Pepe et al. (2011) reporting $K_b = 0.769 \pm 0.090$ m s⁻¹ a 2.8σ difference from our RVSearch result.

We note that there is a suggestive similarity between the reported Doppler periods from both Pepe et al. (2011) and our work and the predicted rotation period for the star. Based on HD 85512’s chromospheric activity, Pepe et al. (2011) predicted $P_{\text{rot}} = 47.13 \pm 6.98$ days, and Lovis et al. (2011) predicted $P_{\text{rot}} = 50.9 \pm 7.0$ days—i.e., within 0.58σ and 0.04σ of the RV signal we measure ($P_b = 51.195 \pm 0.073$ days). Pepe et al. (2011) searched for power in the $\log R'_{\text{HK}}$ activity indicator and the CCF line bisector (BIS) but did not detect any excess power consistent with stellar rotation between 50 and 100 days. Our analysis of the S-index measurements detects significant periods at 44, 45, and 51 days, causing us to suspect rotation as the cause of this signal.

To investigate the consistency of these two periods over time, we generated a moving Bayes factor periodogram using the AGATHA software suite (Feng et al. 2017a). Since RV data are typically not measured in a uniform way, especially when combining results from different surveys, the consistency of a true Keplerian signal may depend on the sampling cadence even if the power is normalized. Moving periodograms can help to identify false positives if a signal is found to be inconsistent even during spans where data was taken at a high cadence and over a number of nights comparable with or longer than the signal period.

The moving periodogram results for HD 85512 (Figure 9) show a prominent peak in the 58 day region when looking at the first half of the RV time series. This signal, however, bifurcates in roughly 2017 (JD \simeq 2458000) and splits into two weaker periodicities of 59 and 57 days. At approximately the same time, a more prominent peak appears at the $P \simeq 51$ day period identified by RVSearch, and becomes the most significant period for the duration of our observational baseline.

As low-mass stars can manifest differential rotation (e.g., Donahue et al. 1996), the reported 58 and 51 day periods could be due to active regions rotating at different latitudes. The trend in differential rotation among G/K dwarfs from the Mt. Wilson survey shown by Donahue et al. (1996; their Figure 3) shows that K dwarfs with $P_{\text{rot}} \simeq 50$ days could exhibit differential rotation at the $\Delta P \simeq 9$ day level. Indeed the previously discussed K3V star HD 16160 (see Section 5.2) was the Mt. Wilson survey poster child for such extreme differential rotation, exhibiting seasonal mean rotation periods ranging from 42.2–51.5 days over five seasons. So it is certainly reasonable for a slow-rotating mid-K dwarf like HD 85512 to manifest differential rotation over $P_{\text{rot}} \simeq 44$ –58 days.

Given the lack of periodic consistency for both signals across the RV time series, we assert that the reported companion HD 85512 b from Pepe et al. (2011) is not caused by a physical planet, but rather that the signal is due to the

star’s rotation. We adopt the notation of calling this HD 85512 RV Signal II (rather than HD 85512 b) in Table 4, since it is the second RV signal fit by the RVSearch algorithm.

RVSearch finds one additional significant signal in the RV data, with an initial ΔBIC periodogram peak of 3891 days. The best-fit period for RV Signal I after running the RV data through RVSearch’s MCMC analysis is $P_1 = 9646 \pm 5500$ days, which we categorize as an “LPS” due to the large error bars and period that stretches beyond the baseline of the combined RV data.

While Pepe et al. (2011) presented time-series $\log R'_{\text{HK}}$ data for the star over a span of 2745 days, and sinusoidal-looking activity variability was observed, they did not estimate a magnetic cycle period. By eye, interpreting the Pepe et al. (2011) $\log R'_{\text{HK}}$ data near JD 2453000 as a minimum and JD 2454500 as a maximum, one can infer $P_{\text{cyc}} \simeq 3000$ days. And indeed, when analyzing the majority of the Pepe et al. (2011) data set (175 of the 185 observations), Lovis et al. (2011) estimated an activity cycle of $P_{\text{cyc}} = 3793^{+806}_{-366}$ days ($10.38^{+2.21}_{-1.55}$ yr).

Here we compile in total 1312 S-index measurements taken over a baseline of ~ 7000 days. With this longer baseline, we see a subsequent activity minimum around JD 2456600 and a maximum around JD 2458800, and RVSearch identifies a significant S-index signal with $P = 4245 \pm 52$ days (11.62 ± 0.14 yr). This falls well within the 1σ uncertainties of the Lovis et al. (2011) activity cycle, and better constrains the period by a factor of 10. It is also consistent with the ΔBIC periodogram peak in the RV data, and so we note that it is likely that the LPS in the RVs is caused by a magnetic activity cycle; however, more data is needed to definitively characterize the nature of this signal.

Our S-Index analysis returns a multitude of additional signals falling between the rotation period and magnetic activity cycle of HD 85512. To fully characterize the significance of all of these signals, a much more in-depth study of the system is required than is covered within the scope of this work. The full list of signals can be found in the activity summary plot contained in the figure set. We leave further analysis of the activity results from this target to future work.

5.11. HD 102365 (GJ 442A)

HD 102365 (GJ 442 A, HR 4523, HIP 57443) is a G2V star (Gray et al. 2006) at $d = 9.32$ pc ($\varpi = 107.3024 \pm 0.0873$ mas; Gaia Collaboration et al. 2021a). The star is just slightly cooler than ($T_{\text{eff}} = 5618 \pm 14$ K) and of similar chromospheric activity to the Sun ($\log R'_{\text{HK}} = -4.94$; Meunier et al. 2022); however, the star is substantially more metal-poor ($[\text{Fe}/\text{H}] = -0.31 \pm 0.02$) compared to the Sun (Soubiran et al. 2022). Recent age estimates for the star make it ancient: 11.3 ± 0.9 Gyr (Nissen et al. 2020), $12.46^{+1.04}_{-1.42}$ Gyr (Gaia Collaboration et al. 2021b), and 13.1 ± 1.5 Gyr (Casali et al. 2020). The star has a low-mass stellar companion of type M4V (Henry et al. 2002) at a projected separation $22''.72$ or 211 au (Tian et al. 2020). The masses of the stars A and B are $0.88^{+0.02}_{-0.03} M_{\odot}$ (Aguilera-Gómez et al. 2018) and $0.192 M_{\odot}$ (Mugrauer 2019), respectively. Tinney et al. (2011) reported an exoplanet with orbital period $P_{\text{orb}} = 122.1 \pm 0.3$ days, $K = 2.40 \pm 0.35$ days, and eccentricity $e = 0.34 \pm 0.14$, corresponding to a Neptune-like predicted mass of $16.0 \pm 2.6 M_{\oplus}$. No subsequent orbital solution has been reported over the past decade.

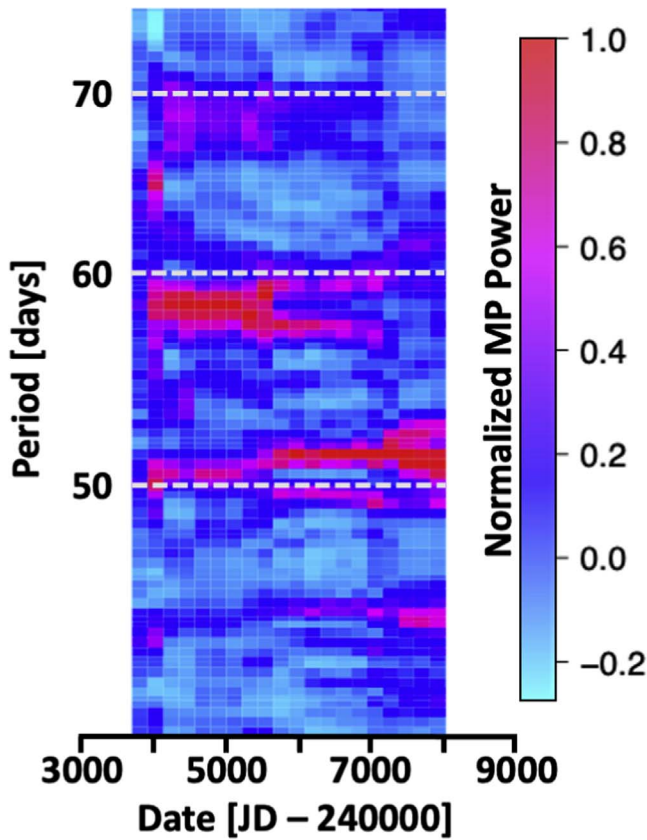


Figure 9. Moving periodogram (MP) for the combined HD 85512 RV data sets. The colors encode the scaled MP power, which is truncated to optimize the visualization of signals. The previously reported 58.43 day planet is visible as a dark-red horizontal band on the left side of the MP, denoting its significance in the first half of the RV time series, but bifurcates and then disappears in later years. A second signal at $P \approx 51$ days takes over in the latter half of the time series, but does not exhibit a tight enough period range to be seriously considered as a planet candidate.

We recover this same planet that Tinney et al. (2011) also recovered, with updated orbital parameters thanks to our additional RV observations. We report parameters for HD 102365 b of $P = 121.3 \pm 0.25$ days, $K = 1.38 \pm 0.23$ m s⁻¹, and $e = 0.28 \pm 0.15$. Note that our RV amplitude is only 58% of that reported by Tinney et al. (2011), resulting in a significantly lower $m \sin i$ of $9.34^{+1.52}_{-1.50} M_{\oplus}$ (Table 4).

We find no significant signals in analysis of the S-index data, but the H α data analysis yields three periodic signals. The first has a period of approximately 1 yr, so we assert that it is most likely caused by the seasonal availability of the star. The second H α signal is fit to a periodogram peak of 7273.6 days, longer than the baseline of the UCLES data. This peak is most likely the same long-period trend present in most of the UCLES H α data as described in Section 3.3, and so we disregard it from consideration as astrophysical. The third H α peak has period $P_{\text{III}} = 49.68$ d and $e_{\text{III}} = 0.08$. While the peak is sharp and well defined, and could reasonably correspond to the stellar rotation period for this ancient star, it does not show any corroborating signal in the S-indices. We note that the MCMC fit to the EW_{H α} data settles on a solution for the longest signal that is nonsensical ($P = 36122 \pm 64000$ days) and so we report the MAP best-fit solution in the summary table. Even the MAP result suffers from the similarity between the LPS and the total observational baseline of the UCLES

data, however, and the resulting fit lands on an orbital period of $P = 18,549$ days; clearly well beyond the scope of our data set.

5.12. HD 104304 (GJ 454)

HD 104304 (GJ 454, HR 4587, HIP 58576, Lalande 22585) is a G8IV star (Gray et al. 2006) at $d = 12.76$ pc ($\varpi = 78.3359 \pm 0.0923$ mas; Gaia Collaboration et al. 2021a). An M4 dwarf companion with mass of $0.21 M_{\odot}$ was discovered using the “lucky imaging” technique on ESO’s NTT 3.5 m by Schnupp et al. (2010), who computed an estimated orbital period of 48.5 yr via comparisons between the imaging results and archival RV data from Marcy (2007). Even with over an additional 7 yr of data since the discovery of the M4 companion, the RV-only fit performed by RVSearch prefers to model the companion’s orbit with a combination of a linear and quadratic trend, rather than a Keplerian. An MCMC analysis of this trend combination does not converge, so we report just the MAP values here. The linear trend is measured at -0.191741 m s⁻¹ day⁻¹, and the quadratic is found to be $3.28667\text{e-}05$ m s⁻¹ day⁻². This companion orbit is also reported by Rosenthal et al. (2021) with $a = 18.1^{+1.4}_{-1.6}$ au ($P = 77.00^{+9.10}_{-9.98}$ yr) and $e = 0.37^{+0.031}_{-0.035}$. Rosenthal et al. (2021) included more RV data for this target than this study, and thus we defer to their measurements for the M4 dwarf companion to HD 104304.

5.13. HD 114613 (GJ 9432)

HD 114613 (GJ 9432, GJ 501.2, HR 4979, HIP 64408) is a G4IV star (Gray et al. 2006) at $d = 20.46$ pc ($\varpi = 48.8691 \pm 0.1058$ mas; Gaia Collaboration et al. 2021a). Brewer et al. (2016) found that the star is more massive ($1.24 \pm 0.17 M_{\odot}$) and metal-rich ([Fe/H] = 0.17) than the Sun, and also cooler ($T_{\text{eff}} = 5641$ K) and larger ($2.14 \pm 0.06 R_{\odot}$) with lower surface gravity ($\log g = 3.87$). Lovis et al. (2011) reported the star to have very low chromospheric activity ($\log R'_{\text{HK}} = -5.509$) with a magnetic activity cycle of $P_{\text{cyc}} = 897^{+61}_{-53}$ days ($2.46^{+0.15}_{-0.17}$ yr).

Wittenmyer et al. (2014) reported a planet with $P_b = 3827 \pm 105$ days and a semiamplitude of $K_b = 5.4 \pm 0.4$ m s⁻¹. Our search of the updated RV data set, which contains 980 additional velocities from HARPS, HIRES, and PFS, does not recover this planet but rather reveals a much longer-period signal at $P_1 = 6622 \pm 270$ days (18.13 ± 0.74 yr) with a semiamplitude of $K_1 = 7.29 \pm 0.44$ m s⁻¹, suggestive of a planet candidate with $m \sin i \approx 0.74 M_J$.

However, both the S-index data and the EW_{H α} periodograms identify significant signals at similar periods to the RV periodogram, with the S-index peak appearing at 7563 days and the EW_{H α} peak at 7653 days. Both of these signals struggle with similarity in duration to the baselines of their respective data sets, however, as the lack of a single activity indicator that covers the full 8500 day span of radial velocities prevents a clean resolution of the activity signals. Instead, both the S-index signal and the EW_{H α} signal are pushed to much larger and nonsensical values: $81,942 \pm 190,000$ days for the S-index data, and $29,213 \pm 41,000$ days for the EW_{H α} data. Because of this, we opt to disregard the MCMC analyses and proceed with the signals evident in the initial ΔBIC periodograms. We take the agreement of these two activity indicator periodogram peaks and their overlap with the RV signal (which is well resolved) to be sufficient evidence that all three signals are manifestations of the same underlying magnetic cycle.

Given this overlap, and the lack of a re-detection of the original 3827 day signal in the radial velocities, we assert that the previously claimed HD 114613 b from Wittenmyer et al. (2014) is not in fact a planet, but may be attributed to a long-period magnetic cycle.

RVSearch detects two additional RV signals with period and semiamplitude pairings of (i) $P_{\text{II}} = 73.14 \pm 0.06$ days, $K_{\text{II}} = 2.54 \pm 0.48$ m s⁻¹, and (ii) $P_{\text{III}} = 1954 \pm 39$ days, $K_{\text{III}} = 2.98 \pm 0.52$ m s⁻¹. There are no corresponding signals in the S-index or EW_{H α} periodograms, and so we label each of these signals as “SRC.” As a subgiant star, we would expect HD 114613 to exhibit higher levels of RV jitter (Luhn et al. 2020), which may drive some of the scatter seen in the RV summary figure.

5.14. HD 115617 (61 Vir)

61 Vir (GJ 506, HD 115617, HR 5019, HIP 64924) is a G7V star (Gray et al. 2006) at $d = 8.53$ pc ($\varpi = 117.1726 \pm 0.1456$ mas; Gaia Collaboration et al. 2021a). The star is slightly less active than the Sun, with reported $\log R'_{\text{HK}}$ values between -4.93 and -5.03 (e.g., Baliunas et al. 1996; Wittenmyer et al. 2006; Hall et al. 2007; Isaacson & Fischer 2010; Vogt et al. 2010; Lovis et al. 2011; Brewer et al. 2016; Meunier et al. 2017). Baliunas et al. (1996) reported an average rotation period of $P_{\text{rot}} = 29$ days based on analysis of the Mt. Wilson survey data, while Lovis et al. (2011) reported a chromospheric activity cycle of $P_{\text{cyc}} = 1548^{+266}_{-811}$ days and a predicted rotation period of $P_{\text{rot}} = 33.9 \pm 3.6$ days. According to Vogt et al. (2010), 61 Vir is a three-planet system with $P_b = 4.21$ days, $P_c = 38.021 \pm 0.034$ days, and $P_d = 123.01 \pm 0.55$ days.

We recover the same three planets as Vogt et al. (2010) with slightly updated parameters: $P_b = 4.21498 \pm 0.00014$ days, $K_b = 2.47 \pm 0.11$ m s⁻¹, $e_b = 0.033 \pm 0.029$; $P_c = 38.079 \pm 0.008$ days, $K_c = 3.56 \pm 0.12$ m s⁻¹, $e_c = 0.026 \pm 0.023$; and $P_d = 123.2 \pm 0.2$ days, $K_d = 1.47 \pm 0.17$ m s⁻¹, $e_d = 0.15 \pm 0.11$. We report these parameters as an improvement to the previously reported ones, due to an additional 2473 RV observations since Vogt et al. (2010).

After analysis of residual signals, Rosenthal et al. (2021) reported the 123 day period signal as a yearly alias. We do not see similar evidence in our data as they report, after examining an additional 10 yr of data. We therefore report this signal as an update to the currently confirmed planet d.

We recover one additional RV signal, RV signal I, with parameters $P = 20565 \pm 21000$ days, $K = 2.23 \pm 0.46$ m s⁻¹, and $e = 0.97 \pm 0.024$. The original periodogram peak being fit by this Keplerian is at 5910.9 days, which is close to the observation baseline, so the fit is poorly constrained. The presence of the peak is evidence of a long-period trend that is not yet well defined, so we classify this signal as LPS.

Analysis of the S-index activity does not yield any detections, but we note that there is significant strength in the S-index periodogram at 3995 days. This may be indicative of an approximately 11 yr magnetic activity cycle, but there is insufficient data to push this signal past the FAP threshold. Continued study of this target would allow for further understanding of potential origins of this signal.

Analysis of H α data returns three detections. The first of these has $P_I = 346.3 \pm 1.9$ days, which we attribute to observation cadence effects. The second and third signals have $P_{\text{II}} = 24.63 \pm 0.02$ days and $P_{\text{III}} = 44.932 \pm 0.069$ days. The observed H α periodicities II and III are a bit shorter and longer,

respectively, than the predicted rotation period ($P_{\text{rot}} = 33.9 \pm 3.6$ days) from Lovis et al. (2011).

H α signal II is close to the rotation period reported by Baliunas et al. (1996), though it is shorter by several days. Because the Lovis et al. (2011) rotation period is predicted, and the Baliunas et al. (1996) P_{rot} is 26 yr old, we assert that it is possible that H α signal II is due to stellar rotation.

H α signal III does not correlate with any periodicity in Ca H & K data nor RV data, and is unlikely to be caused by differential rotation, as its period is ~ 20 days greater than signal II. However, we note that it is not impossible that H α signal III is caused by differential rotation. Quantifying the differential rotation in terms of $\alpha = |P_2 - P_1|/P_{\text{max}} = 0.45$, this would suggest surface shear approximately twice that of the Sun ($\alpha_{\odot} = 0.2$; Reinhold et al. 2013). The observed differential rotation trend for nearby solar-type stars from Donahue et al. (1996) predicts that for a mean rotation period of ~ 35 days, one would predict observing $\Delta P \simeq 7.6$ days. However, the data from Donahue et al. (1996) also show that there are cases for rotators with \sim month-long periods of having ΔP as high as ~ 18 days! Because of this, we believe it is somewhat plausible that H α signals II and III could be hinting at strong differential rotation, but further observations would be needed to test this idea.

5.15. HD 136352 (ν^2 Lup)

ν^2 Lup (HD 136352, GJ 582, HR 5699, HIP 75181) is a nearby G2-V (Gray et al. 2006) star at $d = 14.74$ pc ($\varpi = 67.8467 \pm 0.0601$ mas; Gaia Collaboration et al. 2021a). The star is similar to the Sun in temperature and gravity, but considerably more metal-poor: $T_{\text{eff}} = 5664 \pm 14$ K, $\log g = 4.39 \pm 0.02$, and $[\text{Fe}/\text{H}] = -0.34 \pm 0.01$ (Sousa et al. 2008). Given its high velocity, low metallicity, and α -element enhancement ($[\alpha/\text{Fe}] \simeq 0.17$) (Soubiran & Girard 2005), the star is widely classified as a thick-disk star (e.g., Ibukiyama & Arimoto 2002; Soubiran & Girard 2005; Adibekyan et al. 2012; Hinkel et al. 2017; Kane et al. 2020).³⁷ Lovis et al. (2011) reported a magnetic activity cycle of $P_{\text{cyc}} = 1041^{+581}_{-97}$ days ($2.85^{+1.59}_{-0.27}$ yr), with a predicted rotation period of $P_{\text{rot}} = 25.0 \pm 3.1$ days based on the mean activity level ($\log R'_{\text{HK}} = -4.986$).³⁸ Udry et al. (2019) reported three planet signals in HARPS RV observations for HD 136352. Kane et al. (2020) presented a detailed study of ν^2 Lupi, reporting TESS observations that planets b and c were observed to be transiting, with their derived radii and densities consistent with being on either side of the planet radius gap.

ν^2 Lup b is a $4.62^{+0.45}_{-0.44} M_{\oplus}$ $1.482^{+0.058}_{-0.056} R_{\oplus}$ planet with period $P = 11.57779^{+0.00091}_{-0.0011}$ days—likely the stripped core of a sub-Neptune (now a “super-Earth”), and c is $11.29^{+0.73}_{-0.69} M_{\oplus}$, $2.608^{+0.078}_{-0.077} R_{\oplus}$ exoplanet with period $P = 27.5909^{+0.0028}_{-0.0031}$ days—a “sub-Neptune” (Kane et al. 2020). ν^2 Lup d is a planet with

³⁷ The only known star brighter in the V and G bands than HD 136352 with transiting exoplanets in the NASA Exoplanet Archive is HD 219134, which is an α -poor thin-disk star of approximately solar metallicity (Mishenina et al. 2004; Ramírez et al. 2012). The only known star brighter in the K_s band than HD 136352 is 55 Cnc, which is a metal-rich thin-disk star (Mishenina et al. 2004; Ramírez et al. 2012). Hence, HD 136352 (ν^2 Lup) appears to be the brightest—either in the visible or near-IR bands—thick-disk star known to have transiting exoplanets.

³⁸ ¹⁷ Independently, Isaacson & Fischer (2010) predicted the rotation period of HD 136352 to be 23 days based on $\log R'_{\text{HK}}$.

radius $2.56 \pm 0.09 R_{\oplus}$ and mass $8.82 \pm 0.94 M_{\oplus}$ with orbital period $P = 107.245$ days (Delrez et al. 2021).

We recover all three of these planets, but defer to Kane et al. (2020) and Delrez et al. (2021) for the most accurate parameters. We recover one additional RV signal with $P = 121.66 \pm 0.26$ days, $K = 0.68 \pm 0.13$, and $e = 0.22 \pm 0.19$. Udry et al. (2019) recovered a similar signal in their RV analysis, with a period of 123 days, and discarded it, as a three-planet fit was favored over four in their analysis. Our search results find that the signal just crosses the threshold for being considered a valid additional signal; however, the significance of the signal in the running periodogram wanes notably as more and more RV data points are added, which suggests a non-Keplerian origin. Additionally, a 121 day planet would be dynamically inconsistent with the confirmed 107 day planet, ruling this out as a planetary signal, and leaving only the possibility of an activity signal. Because of this, we classify the fourth signal as being due to stellar activity. We note, also, that Rosenthal et al. (2021) detected a false-positive signal with a period of 244 days, which is quite nearly double that of the fourth signal detected here and in Udry et al. (2019).

The RVSearch analysis of the S-index data returns no significant detections. Despite our large increase in observation time line since Lovis et al. (2011), from 2543 days to 5771 days, we find no evidence for the $P_{\text{cyc}} = 2.85$ yr activity cycle reported in that work.

Analysis of the $\text{EW}_{\text{H}\alpha}$ data returns two significant periodicities. Signal I has period $P = 364.7$ days in the periodogram, which is clearly close to 1 yr and we suspect is due to sampling effects. The signal also has high eccentricity, but there is a significant gap in the orbital phase coverage, which RVSearch addresses by using a high-eccentricity solution to try and fit a Keplerian curve to this jump. Signal II is detected based on a periodogram peak close to 6000 days, which is approximately the observation baseline for the UCLES data. The MCMC Keplerian fit is poorly constrained because of this fact, so we attribute this signal to the long-period UCLES trend and disregard it as significant. When run through RVSearch's MCMC analysis, the LPS produces nonsensical error bars of $P = 19924 \pm 33000$. We therefore choose to report the best-fit MAP orbital solution in the $\text{EW}_{\text{H}\alpha}$ summary table.

5.16. HD 160346 (GJ 688)

HD 160346 (GJ 688, HIP 86400) is a nearby K2.5V (Gray et al. 2003) at $d = 11.00$ pc ($\varpi = 90.91 \pm 0.67$ mas; van Leeuwen 2007). The star has published chromospheric activity estimates ranging from $\log R'_{\text{HK}} = -4.766$ (Meunier et al. 2017) to -4.85 (Gondoin 2020)—comparable to the active Sun. Analysis of the Mt. Wilson Ca II H & K survey data by Donahue et al. (1996) detected seasonal rotation periods ranging from $P_{\text{rot}} = 35.4\text{--}37.8$ days, with an average over five seasons of $P_{\text{rot}} = 36.4$ days. Boro Saikia et al. (2018) reported a Ca II H & K activity cycle of $P_{\text{cyc}} = 7.19 \pm 0.04$ yr. GJ 688 is an SB1 with three published orbits listed in the SB9 catalog (Pourbaix et al. 2004), with orbits by Tokovinin (1991), Katoh et al. (2013), and Halbwachs et al. (2018). The latter provides: $P = 83.7140 \pm 0.0120$ days, $e = 0.2100 \pm 0.0120$, and $K = 5644 \pm 57$ m s $^{-1}$.

Our updated RV analysis produces best-fit orbital parameters of $P = 83.7286 \pm 0.0005$ days, $e = 0.2048 \pm 0.00033$, and

$K = 5690.3 \pm 2.3$ m s $^{-1}$, shrinking the error bars on all three parameters by over an order of magnitude.

The S-index analysis detects a number of significant signals, the first two of which have periods of $P = 2975 \pm 600$ days and 392.6 ± 3.2 days. Comparison of their RVSearch periodograms, however, suggests that one of these signals is likely an alias of the other. The longer-period signal seems more likely to be due to a decade-long magnetic cycle much like the Sun's; however, we caution that our analysis does not include the detailed phase analysis necessary to identify which of these signals is the true manifestation of the star's activity.

The additional two S-index signals detected by RVSearch have much shorter periods of $P = 7.9567 \pm 0.0055$ days and $P = 2.54223 \pm 0.00068$ days. While these are both too short to be due to HD 160346's rotation, there is a possibility that one of the signals could be due to flux contributions from a fast-rotating, low-mass companion. But given the relative sparsity of the data, we do not have sufficient evidence to say anything truly definitive about their origins.

5.17. HD 160691 (μ Ara)

μ Ara (HD 160691, GJ 691, HR 6585, HIP 86796, Cervantes) is a G3IV-V (Gray et al. 2006) star at $d = 15.6$ pc ($\varpi = 64.0853 \pm 0.0904$ mas; Gaia Collaboration et al. 2021a), with four previously reported planets (Pepe et al. 2007). The star is metal-rich ($[\text{Fe}/\text{H}] = 0.27 \pm 0.05$) and magnetically inactive ($\log R'_{\text{HK}} = -5.11$; Gomes da Silva et al. 2021), with slightly lower surface gravity than typical G dwarfs ($\log g = 4.20 \pm 0.02$; Ramirez et al. 2013). Combining asteroseismic observations with evolutionary models, Soriano & Vauclair (2010) found that μ Ara is most likely near the beginning of its subgiant branch phase, with a mass of $1.10 \pm 0.02 M_{\odot}$ and age of 6.34 ± 0.80 Gyr. The most recent parameters for this system are from Benedict et al. (2022). We recover the same four signals with minor revisions but generally good agreement on the best-fit values, and significant improvements to all but one of the parameters' uncertainties: $P_b = 644.93 \pm 0.28$ days, $K_b = 35.7 \pm 0.2$ m s $^{-1}$, $e_b = 0.0499 \pm 0.0082$; $P_c = 9.6394 \pm 0.0008$ days, $K_c = 2.8 \pm 0.2$ m s $^{-1}$, $e_c = 0.132 \pm 0.069$; $P_d = 308.4 \pm 0.23$ days, $K_d = 12.7 \pm 0.3$ m s $^{-1}$, $e_d = 0.074 \pm 0.016$; and $P_e = 4035 \pm 21$ days, $K_e = 22.25 \pm 0.24$ m s $^{-1}$, $e_e = 0.026 \pm 0.013$.

We detect no significant S-index activity signals, but do find two signals in the $\text{H}\alpha$ data. The first of the $\text{H}\alpha$ signals is fit from a ΔBIC periodogram peak at 5293.7 days, which is close to the UCLES observation baseline, so we attribute this to the long-period UCLES systematic present in all of the $\text{H}\alpha$ data (see Section 3.3 for further discussion). $\text{H}\alpha$ Signal II has a period of $P = 362.4 \pm 1.6$ days, close to one year. This signal is likely caused by the star's seasonal availability and the observing cadence, so we disregard it as a significant detection for this system.

5.18. HD 192310 (GJ 785)

HD 192310 (HR 7722, GJ 785, HIP 99825) is a K2+V star (Gray et al. 2006) of roughly solar metallicity ($[\text{Fe}/\text{H}] = -0.03 \pm 0.04$; Tsantaki et al. 2013) at $d = 8.81$ pc ($\varpi = 113.4872 \pm 0.0516$ mas; Gaia Collaboration et al. 2021a), and with two previously reported planets (Pepe et al. 2011). Lovis et al. (2011) detected a magnetic activity cycle of $P_{\text{cyc}} = 3792^{+806}_{-566}$ days and predicted the rotation period to be

$P_{\text{rot}} = 43.7 \pm 4.9$ days based on their estimate of the star's mean chromospheric activity ($\log R'_{\text{HK}} = -4.996$). Combining the star's mean chromospheric activity levels ($\log R'_{\text{HK}} = -4.993$) recently reported by Meunier et al. (2017), with its color ($B - V = 0.884$; Mermilliod 2006) and the rotation–activity relations from Mamajek & Hillenbrand (2008), one can predict the star's rotation to be approximately $P_{\text{rot}} \simeq 48$ days.

We detect two RV signals that appear to correspond to the previously reported planets b and c, with $P_b = 74.278 \pm 0.035$ days, $K_b = 2.484 \pm 0.098 \text{ m s}^{-1}$, $e_b = 0.032 \pm 0.027$, and $P_c = 549.1 \pm 4.5$ days, $K_c = 1.3 \pm 0.1 \text{ m s}^{-1}$, $e_c = 0.077 \pm 0.073$. These appear to be the most accurate periods yet derived, with Rosenthal et al. (2021) recently reporting $P_b = 74.062 \pm 0.085$ days, and Pepe et al. (2011) reporting $P_c = 525.8 \pm 9.2$ days. And our derived amplitude for b is three times more precise than that derived by Rosenthal et al. (2021; $2.49^{+0.35}_{-0.33} \text{ m s}^{-1}$), thanks to the addition of the HARPS and UCLES data. We note that our amplitude for planet c is less than half that reported by Pepe et al. (2011; $2.27 \pm 0.28 \text{ m s}^{-1}$). Given the increase in observational baseline and the number of instruments contributing data, and the additional signals resolved in the RV data, some shifting in the semiamplitude is expected. However, as this is an almost 3.5σ offset from the Pepe et al. (2011) value, a more thorough analysis that treats the RV and activity indicator data simultaneously is well warranted.

RVSearch also identifies four additional RV signals, which we designate as Signals I, II, III, and IV. Signal I has $P = 3836 \pm 240$ days, $K = 1.48 \pm 0.11 \text{ m s}^{-1}$, and $e = 0.34 \pm 0.15$. We suspect that Signal I is caused by activity due to a corresponding peak in the S-index data at $P = 3817 \pm 60$ days (10.45 ± 0.16 yr), which matches the magnetic activity cycle period ($P_{\text{cyc}} = 3792^{+806}_{-566}$ d = $10.38^{+2.21}_{-1.55}$ yr) reported by Lovis et al. (2011). We therefore attribute it to a magnetic activity cycle.

RV signals II and III have similar periods: $P = 43.614 \pm 0.023$ days for signal I and $P = 39.509 \pm 0.059$ days for signal II. Analysis of S-index data using RVSearch returns various signals with periods between 35 and 50 days. Recalling that Lovis et al. (2011) predicted the star's rotation period to be $P_{\text{rot}} = 43.7 \pm 4.9$ days, we attribute these signals II and III to differential rotation of the star, as the appearance of active regions at various latitudes over the course of the star's magnetic activity cycle could lead to a wide range of measured periods.

Finally, RV signal IV has parameters $P = 24.559 \pm 0.016$ days, $K = 0.6 \pm 0.1 \text{ m s}^{-1}$, and $e = 0.16 \pm 0.12$. The periodogram peak for this signal is sharp and well defined, and the RV fit is very well constrained. The period is sufficiently distinct from the rotation period that it is unlikely to be a signature of differential rotation. We therefore report RV Signal IV as a Candidate in Table 4, and recommend further investigation of this signal to determine whether it is planetary in origin.

In addition to the differential rotation signals, the RVSearch S-index analysis returns three well-defined signals with $P = 345.34 \pm 0.048$ days, $P = 432.6 \pm 3.4$ days, and $P = 133.38 \pm 0.043$ days. As these are logarithmically almost half way between the star's rotation period and its magnetic activity cycle, no obvious activity-based explanation exists for these signals. We note that the eccentricities of these signals

($e = 0.918, 0.7$, and 0.78 , respectively) are significantly higher than those of the other S-index detections ($e = 0.26$ for the magnetic activity cycle, and 0.14 on average for the four rotation-associated periods). This could suggest that these intermediate periods are being driven by small amounts of outlier points that were not far enough removed from the mean to be rejected by our 5σ outlier clipping.

Rosenthal et al. (2021) detect a false-positive signal at $P = 1630^{+51}_{-53}$ days and $K = 1.95^{+0.49}_{-0.36} \text{ m s}^{-1}$, which they attribute to a long-period magnetic activity cycle. We do not recover this same signal.

The $\text{EW}_{\text{H}\alpha}$ data for this star produce two significant signals when analyzed with RVSearch. The first is a very-long-period signal, with an initial periodogram peak of 30,840 days (well beyond the UCLES baseline) and a best-fit period of $P = 62641 \pm 110000$ days. Given the extreme nature of both the signal duration and the corresponding uncertainty on the period, we report the best-fit MAP solution in place of the MCMC solution. That gives $P = 13627.7$ days for the longer-period signal, and $P = 363.678$ days for the second signal, which seems to be driven by seasonal observing impacts that leave $\sim 1/3$ of the orbital phase with little to no data, and therefore make it easier for high-eccentricity signals to be fit to the data.

5.19. HD 209100 (ϵ Ind A)

ϵ Indi A (HD 209100, GJ 845, HR 8387, HIP 108870) is a well-studied K4V(k) star (Gray et al. 2006) at $d = 3.64$ pc ($\varpi = 274.8431 \pm 0.0956$ mas; Gaia Collaboration et al. 2021a). Lovis et al. (2011) reported a magnetic activity cycle of $P_{\text{cyc}} = 1719^{+217}_{-315}$ days ($4.71^{+0.59}_{-0.86}$), and predicted the star's rotation period to be $P_{\text{rot}} = 37.6 \pm 6.2$ days based on the star's chromospheric activity ($\log R'_{\text{HK}} = -4.806$). It has one reported planet, a cold Jupiter-mass planet with a period of $P_b = 45.2$ yr (Feng et al. 2019a).

We detect only a very poorly constrained LPS in our RV data, with a ΔBIC periodogram peak of 13138.7 days (35.97 yr), and a best-fit MCMC solution of $P = 13626 \pm 110000$ days (37.3 ± 30.1 yr). Due to the signal clearly stretching beyond the bounds of our RV baseline, we note this as an “LPS” in our detections table. Feng et al. (2019a), however, analyzed a longer RV baseline than used here, as it includes data from previous-generation RV instruments, such as the Coude Echelle Spectrograph Long Camera and Very Long Camera (see Zechmeister et al. 2013), and the Ultraviolet and Visible Spectrometer (Dekker et al. 2000) and utilizes a combination of RVs and Hipparcos and Gaia astrometry to constrain the planet's orbit. It is therefore not surprising that we do not resolve the Feng et al. (2019a) planet in our RV time series, and we defer to their publication for orbital parameters on ϵ Indi A b.

In our S-index activity analysis for HD 209100, we detect a signal with period $P = 2063 \pm 160$ days (5.65 ± 0.44 yr), which matches the Lovis et al. (2011) magnetic activity cycle to within 1.5σ . We report this as an updated fit to the previously published activity cycle. We detect an additional, much shorter, S-index signal with $P = 32.87 \pm 0.067$ days, which matches the Lovis et al. (2011) predicted rotation period to within 1σ . We therefore take this to be an updated, and better constrained, measurement of the star's rotation period.

6. Targets with New Signals

Here we present results from targets whose analyses returned signals that have not previously been published. Rather than the lettering system that is used to identify planets and companions, we refer to our new detections with Roman numerals for discussion purposes. Signals are interpreted and reported in Table 4.

6.1. HD 1581 (ζ Tuc)

ζ Tuc (HD 1581, GJ 17, HR 77, HIP 1599) is an F9.5V type star (Gray et al. 2006) at distance $d = 8.59 \pm 0.05$ pc ($\varpi = 116.46 \pm 0.16$ mas; van Leeuwen 2007). The star is slightly hotter ($T_{\text{eff}} = 5932 \pm 12$ K), and more metal-poor ($[\text{Fe}/\text{H}] = -0.21 \pm 0.01$) than the Sun, but with similar gravity ($\log g = 4.43 \pm 0.03$; Soubiran et al. 2022). Lovis et al. (2011) reported a magnetic activity cycle of $P_{\text{cyc}} = 1018^{+51}_{-47}$ days ($2.79^{+0.14}_{-0.13}$) based on 127 $\log R'_{\text{HK}}$ measurements over a 2625 day span, and using the mean activity level ($\log R'_{\text{HK}} = -4.954$), they predict the rotation period to be $P_{\text{rot}} = 16.7 \pm 2.6$ days. There are no confirmed exoplanets for this system.

We recover three RV signals with RVSearch. RV signal I has parameters $P = 635.0 \pm 4.4$ days, $K = 0.89 \pm 0.14$, and $e = 0.55 \pm 0.13$. This signal may correspond to magnetic activity, as the period is long, and the peak in the periodogram is somewhat broad and accompanied closely by several other peaks. The next strongest peak, located at $P \simeq 860$ days sits directly on top of the yearly alias for the detected 635 day signal, denoted by the red dashed line in the RVSearch summary plot. Examination of the window function for this data set reveals a dramatic yearly period in the periodogram, further supporting the concept that one of these signals is indeed the yearly alias of the other. Given the similarity of their periodogram peaks, however, identifying which signal is the true Keplerian would require a full analysis of the phases of the peaks in the window function as seen in Dawson & Fabrycky (2010). This is beyond the scope of our current effort, but we encourage future investigation into the true nature of these two signals. For the time being, as there are no correlated peaks in the activity periodogram for the RVSearch-identified $P = 635.0$ day peak, we report only this signal in our summary table and classify it as an SRC. The two remaining signals (II and III) are more well-defined periodogram peaks.

Signal II has $P = 15.653 \pm 0.005$ days, $K = 0.662 \pm 0.096$, and $e = 0.106 \pm 0.097$. This aligns with the rotation period predicted by Lovis et al. (2011). With our increased observation baseline of 3600 RV measurements, we have the ability to measure the rotation period for this star much more accurately than previous works. We report RV signal II as a measurement of the rotation period for HD 1581.

Signal III has parameters $P = 29.4661 \pm 0.0041$ days, $K = 1.6 \pm 1.1$ m s $^{-1}$, and $e = 0.89 \pm 0.12$. The period of this detection is almost exactly twice the rotation period, and we therefore suspect it has stellar and not planetary origins.

A periodogram analysis of 456 measurements (spanning 6157 days) of the H α EW measurements taken with UCLES yielded a signal just below the detection threshold of the FAP 0.001 at $P = 29.7$ days, which further points to the 29 day RV signal being caused by activity. We therefore classify RV Signal III as Activity in Table 4.

Analysis of the S-index activity data returns no significant detections.

6.2. HD 2151 (β Hyi)

β Hyi (GJ 19, HD 2151, HR 98, HIP 2021) is a bright ($V = 2.82$; ESA 1997) G0V star (Gray et al. 2006) at distance $d = 7.46$ pc ($\varpi = 134.07 \pm 0.11$ van Leeuwen 2007). Asteroseismic analysis of β Hyi by Brandão et al. (2011) yields a mass of $1.08 \pm 0.03 M_{\odot}$ and age of 6.40 ± 0.56 Gyr.

We recover one RV signal with $P = 5365 \pm 1400$ days, $K = 3.21 \pm 0.58$ m s $^{-1}$, and $e = 0.54 \pm 0.16$. We suspect that the signal is activity-induced due to the lack of consistent growth in the running periodogram, which quantifies the signal's power as a function of number of RV data points included. Analysis of H α measurements from UCLES shows a long-period trend just under the detection threshold at $P = 4957.8$ days. We regard this signal with some skepticism as it is close to the observation baseline for the spectrograph (see discussion in Section 3.3) but note that it supports a conclusion that this signal may be caused by activity. S-index data is too sparse to make any significant detections, so we cannot completely corroborate that suspicion and report the signal as SRC rather than activity. A future, more in-depth study of stellar activity is recommended to completely characterize this signal.

Finally, we note that the RV residuals periodogram contains a well-defined peak at 73.3 days, which may correspond to rotation, as this is a slightly evolved star.

6.3. HD 20766 (ζ^1 Ret)

ζ^1 Ret (HD 20766, GJ 136, HR 1006, HIP 15330) was classified as G2.5V H δ 1 by Keenan & McNeil (1989) and lies at $d = 12.04$ pc ($\varpi = 83.0240 \pm 0.0438$ mas; Gaia Collaboration et al. 2021a). ζ^1 Ret is the secondary of a wide binary³⁹ (309") with ζ^2 Ret (HD 20807; see Section 6.4). A few conflicting estimates of the rotation period have been reported for this star: $P_{\text{rot}} < 12.1$ days (Cincunegui et al. 2007), $P_{\text{rot}} = 14.81$ days (Oelkers et al. 2018), and $P_{\text{rot}}/\text{sini} = 15.9$ days (Ammeler-von Eiff & Reiners 2012). Recently, Flores et al. (2021) found evidence for an activity cycle of $P_{\text{cyc}} = 1527 \pm 43$ days (4.18 ± 0.12 yr).

We report one significant RV detection. The periodogram peak occurs at $P = 5643.5$ days, which is fairly close to the observation baseline of approximately 6000 days for this target. As discussed in Section 4.1, the RVSearch MCMC fitting for this signal yields nonphysical results ($P = 10218 \pm 10000$ days, $K = 12 \pm 2$ m s $^{-1}$, $e = 0.82 \pm 0.11$), so we record the periodogram peak as the best estimate of this signal and classify it as LPS. The turnaround we see in the center of the

³⁹ From the Gaia DR3 astrometry, Kervella et al. (2022) reported that ζ^2 and ζ^1 Ret have projected separation $309''$ (3720 au) and V_{tan} that agree within 0.40 ± 0.01 km s $^{-1}$, with predicted escape velocity $v_{\text{esc}} = 0.91$ km s $^{-1}$. Using Gaia DR3, we estimate that the stars are co-distant to $\Delta d = 1095 \pm 2240$ au. The difference in the mean radial velocities reported by Soubiran et al. (2018; 11.953 ± 0.0031 km s $^{-1}$ for ζ^2 Ret, and 12.488 ± 0.0019 km s $^{-1}$ for ζ^1 Ret) is $\Delta v_R = 0.535 \pm 0.004$ km s $^{-1}$. Ignoring possible differences due to gravitational redshift and convective blueshift as negligible, since the stars are nearly twins, we interpret the velocity offset as true orbital motion. The total relative orbital motion between ζ^2 and ζ^1 is then only $v_{\text{orb}} = 662 \pm 9$ m s $^{-1}$, and with a current 3D separation of $s = 4100^{+1000}_{-350}$ (68% CL). The system is consistent with being a bound binary with $a \simeq 4500$ au and $P \simeq 220$ kyr, although further analysis would be needed to constrain the orbit further.

RV time series was also reported by Zechmeister et al. (2013) based on the HARPS data.

We do not recover this signal in our S-index analysis, but the nondetection is unsurprising given that the RV signal is driven by UCLES data, which lack S-indices. We report one S-index activity detection, which encounters a similar period-to-baseline fitting issue as the detection in the RVs; our observation baseline is just over 1200 days, while the detection peaks at $P = 1406$ days (3.85 yr) in the ΔBIC periodogram. This appears to correspond to the 4.18 ± 0.12 yr activity cycle reported by Flores et al. (2021). In this case, the MCMC fit cannot even reach a final fit solution, and so instead we report just the MAP period fit in the S-index table while noting the signal's LPS-esque behavior. This signal overlaps with one just barely below the detection threshold in the $\text{EW}_{\text{H}\alpha}$ data, with $P = 1059$ days (2.90 yr).

6.4. HD 20807 (ζ^2 Ret)

ζ^2 Ret (HD 20807, GJ 138, HR 1010, HIP 15371) is a slightly metal-poor ($[\text{Fe}/\text{H}] = -0.215 \pm 0.010$; Adibekyan et al. 2016) G1V standard star (Keenan & McNeil 1989), and fairly nearby at distance 12.04 pc ($\varpi = 83.0606 \pm 0.0608$ mas; Gaia Collaboration et al. 2021a). ζ^2 Ret is the primary of a wide binary (309") with ζ^1 Ret (HD 20766; see Section 6.3). Lovis et al. (2011) reported a magnetic activity cycle of $P_{\text{cyc}} = 1133_{-65}^{+1090}$ days ($3.10_{-0.18}^{+2.98}$ yr) based on only 38 $\log R'_{\text{HK}}$ measurements over a span of 2309 days. Flores et al. (2021) presented an analysis of the time series chromospheric activity data for ζ^2 Ret, finding an activity cycle of $P_{\text{cyc}} = 7.9 \pm 0.38$ yr ($\sim 2885 \pm 139$ days), and predicting a rotation period of $P_{\text{rot}} = 16.5 \pm 1.8$ days based on $\log R'_{\text{HK}}$. Zechmeister et al. (2013) also reported correlations between the RVs and $\log R'_{\text{HK}}$ FWHM, and BIS based on their limited HARPS data that spanned ~ 1500 days. The star has been claimed to have far-IR excess (70, 100 μm) from a dusty debris disk (Trilling et al. 2008; Eiroa et al. 2013; Gáspár et al. 2013; Sierchio et al. 2014); however, recent Atacama Large Millimeter/submillimeter Array observations have shown that the millimeter emission in the vicinity of ζ^2 Ret is likely to be attributable to background sources (Faramaz et al. 2018).

We detect one significant RV signal with $P = 3180 \pm 130$ days, $K = 2.9 \pm 0.4$ m s $^{-1}$, and $e = 0.23 \pm 0.11$. This signal, corresponding to a period of 8.7 yr, is just beyond the 1σ error overlap with the activity cycle reported by Flores et al. (2021), prompting suspicion about its nature. Our own S-index analysis does not yield any significant detections, and indeed the star appears to be very inactive. Our $\text{EW}_{\text{H}\alpha}$ analysis detects one significant signal with a periodogram peak at $P = 2897$ days (7.9 yr), which aligns well with the activity cycles reported in the literature. We note, however, that this is also approximately half the UCLES observation baseline and a period where the stacked periodogram of $\text{EW}_{\text{H}\alpha}$ nondetections exhibits significant power (Figure 3). We therefore regard this activity detection with some uncertainty as discussed in Section 3.3. Because of this uncertainty and the lack of our own S-index detection, we report our RV Signal I as SRC rather than activity, and recommend a more in-depth study of activity indicators for this target to confirm the nature of this signal.

6.5. HD 23249 (δ Eri)

δ Eri (HD 23249, GJ 150, HR 1136, Rana) is a K0+IV spectral standard star (Keenan & McNeil 1989) at $d = 9.09$ pc ($\varpi = 110.0254 \pm 0.1944$ mas; Gaia Collaboration et al. 2021a). The star is a slightly metal-rich, evolved star ($T_{\text{eff}} = 5045$ K, $\log g = 3.77 \pm 0.02$, $[\text{Fe}/\text{H}] = 0.06 \pm 0.01$; Jofré et al. 2014), slow-rotating ($P_{\text{rot}} = 71$ days, $v \sin i = 1.54 \pm 0.23$ km s $^{-1}$; Baliunas et al. 1996; Jofré et al. 2015), and magnetically very inactive—both chromospherically ($\log R'_{\text{HK}} = -5.184$; Baliunas et al. 1996) and coronally ($\log(L_X/L_{\text{bol}}) = -7.14 \pm 0.18$; Morel et al. 2004). Despite the very low activity, the star is oddly classified in the General Catalog of Variable Stars (Samus' 2017) as an RS CVn variable (chromospherically active binary)—which typically implies a very magnetically active detached stellar binary with orbital period between ~ 1 and ~ 14 days (Hall 1976). This RS CVn classification appears to be erroneous and can be traced to time series photometric observations that used a fast-rotating spotted star as a photometric standard. Fisher et al. (1983) reported δ Eri to be a suspected RS CVn variable based on detection of ~ 0.02 mag amplitude variability with period ~ 10 days. Unfortunately the observations used ϵ Eri as a photometric standard, itself being a spotted variable star with $P_{\text{rot}} \simeq 10$ –12 days and having variability at the ~ 0.01 –0.03 mag level (Frey et al. 1991; Croll et al. 2006). Subsequent VLTI/VINCI interferometry measurements by Thévenin et al. (2005) ruled out the existence of any stellar companion down to about $\sim 2\%$ the luminosity of δ Eri. We concur with findings of Eaton & Poe (1985), Frey et al. (1991), and Thévenin et al. (2005) that δ Eri is unlikely to be an RS CVn variable, and suggest that this four-decade-old misclassification for this bright nearby star be dropped from the GCVS and SIMBAD.

RVSearch recovers one significant RV signal, with parameters $P = 596.6 \pm 2.6$ days, $K = 3.0 \pm 1.1$ m s $^{-1}$ and $e = 0.65 \pm 0.14$. Though the peak is well defined, as expected for a planet, the eccentricity is a bit high and is being pulled quite strongly by a few UCLES points. We thus classify this signal as SRC, and suggest that future work investigate this signal more thoroughly.

No signals are detected in the S-index activity data. $\text{H}\alpha$ activity analysis returns one significant signal just over the detection threshold, with $P = 49.568 \pm 0.097$ days, $e = 0.21 \pm 0.18$. This is substantially shorter than the reported rotation period from Baliunas et al. (1996; 71 days). It seems possible that we could be seeing differential rotation ($\alpha = |P_2 - P_1|/P_{\text{max}} = 0.43$) with surface shear approximately twice that of the Sun ($\alpha_{\odot} = 0.2$; Reinhold et al. 2013). There is a general trend that slower rotating stars exhibit enhanced differential rotation (e.g., Donahue et al. 1996); however, the behavior is not well-constrained observationally for periods longer than ~ 1 month, or for subgiants (e.g., Reinhold et al. 2013).

6.6. HD 32147 (GJ 183)

HD 32147 (GJ 183, HR 1614, HIP 23311) is a metal-rich ($[\text{Fe}/\text{H}] = +0.29 \pm 0.02$; Maldonado et al. 2012) K3+V star (Gray et al. 2003) at $d = 8.84$ pc ($\varpi = 113.0715 \pm 0.0222$ mas; Gaia Collaboration et al. 2021a). Although Baliunas et al. (1996) reported the star to have low chromospheric activity ($\log R'_{\text{HK}} = -4.948$) and slow rotation ($P_{\text{rot}} = 47$ days), it is classified as a BY Dra variable with amplitude 0.03 mag in the

General Catalog of Variable Stars (Samus' 2017). More recently, Willamo et al. (2020) reported $\log R'_{\text{HK}} = -4.939$ and rotation period $P_{\text{rot}} = 33.7$ days, and activity cycle period $P_{\text{cyc}} = 10.40$ yr (~ 3800 days). Boro Saikia et al. (2018) estimated the activity period to be $P_{\text{cyc}} = 10.84 \pm 0.15$ yr, whereas analysis of Mt. Wilson survey between 1967 and 2002 by Garg et al. (2019) reported two activity cycles of 9.33 yr (~ 3408 days) and 12.42 yr (~ 4536 days). We report one RV signal with $P = 2866 \pm 140$ days, $K = 1.8 \pm 0.21$ m s $^{-1}$, and $e = 0.34 \pm 0.13$. Rosenthal et al. (2021) found a similar signal with $P = 3444.0^{+91.0}_{-81.0}$ days, which they classified as a false positive due to activity as well. Our signal is not quite close enough for us to consider it to be from the same source, and so we classify our RV Signal I as SRC rather than activity.

Analysis of S-index activity data returns a multitude of signals. The first two of these signals have periods of $P = 3774 \pm 250$ days and 3204 ± 310 days, which appear to be the same periodogram peak being fit multiple times. This signal correlates well with the 9.33 yr (3405.5 day) signal from Garg et al. (2019) and the false positive from Rosenthal et al. (2021), so we report it as that same cycle but make no update to the period as our detection is clearly not well constrained. We recover a second set of similar signals, with periods $P = 381.7 \pm 2.4$ days and $P = 343.2 \pm 2.7$ days. The periodograms clearly show that these are aliases of the respective first two signals, so we disregard these detections as having any significance.

We recover one further activity signal with parameters $P = 95.6 \pm 0.24$ days, $e = 0.39 \pm 0.22$. This signal does not appear in the radial velocity data, though we note that it is approximately twice the rotation period of 47 days reported by Baliunas et al. (1996). Additionally, the RV residual periodogram shows a strong peak at 44.4 days, which may correspond to the reported rotation period.

The residual peak in the periodogram at 44.3 days likely corresponds to the rotation period, which Baliunas et al. (1996) measured to be 47 days.

Additionally, Rosenthal et al. (2021) reported a false positive at $P = 51.997^{+0.078}_{-0.039}$ days, which they attribute to an annual or instrumental systematic. Our data includes instruments not included in their study such as HARPS and PFS, so we expect not to detect this systematic from HIRES as strongly.

6.7. HD 38858 (GJ 1085)

HD 38858 (GJ 1085, HR 2007, HIP 27435) is a nearby star at distance 15.21 pc ($\varpi = 65.7446 \pm 0.0307$ mas; Gaia Collaboration et al. 2021a) classified as G2V (Gray et al. 2003), with just slightly higher gravity ($\log g = 4.51 \pm 0.01$) than the Sun but more metal-poor ($[\text{Fe}/\text{H}] = -0.22 \pm 0.01$; Sousa et al. 2008). Isaacson & Fischer (2010) and Lovis et al. (2011) predicted rotation periods of 24 days and 23.6 ± 3.1 days based on mean chromospheric activity levels. The star's mean chromospheric activity level ($\log R'_{\text{HK}} = -4.948$; Lovis et al. 2011) is similar to that of the Sun. We detect one RV signal, with $P_1 = 2893 \pm 150$ days, $K_1 = 2.8 \pm 0.3$ m s $^{-1}$, and $e_1 = 0.19 \pm 0.12$. The long period and broad shape of this peak in the periodogram lead us to suspect that this signal is caused by magnetic activity. Though S-index analysis returns no significant detections, we note the presence of a growing signal in the periodogram at $P = 2615.0$ days. This signal does not meet our detection threshold of

$\Delta BIC = 10$, but is strong evidence supporting our classification of RV Signal I as a magnetic activity cycle.

Rosenthal et al. (2021) reported a similar signal with $P = 3113^{+82.0}_{-79.0}$ days, $K = 4.43^{+0.73}_{-0.64}$ m s $^{-1}$, which they attribute to an activity cycle as well.

6.8. HD 100623 (20 Crt)

20 Crt (HD 100623, GJ 432 A, HR 4458, HIP 56452) is a K0-V star (Gray et al. 2006) at distance $d = 9.55$ pc ($\varpi = 104.6570 \pm 0.0267$ mas; Gaia Collaboration et al. 2021a). 20 Crt is cooler ($T_{\text{eff}} = 5189$ K) and more metal-poor ($[\text{Fe}/\text{H}] = -0.37$; Valenti & Fischer 2005). It has a wide separation ($15''3$, projected separation 146 au; Tian et al. 2020) white dwarf companion 20 Crt B (GJ 432B, HD 100623B, VB 4) of type DC10 (Holberg et al. 2016). The Kervella et al. (2019) analysis of Hipparcos and Gaia astrometry found 20 Crt A to have a tangential velocity anomaly of 41.26 ± 5.38 m s $^{-1}$ with a position angle of velocity anomaly vector of $\text{PA} = 131^\circ.24 \pm 5^\circ.18$, which is remarkably close to the observed PA to component B ($\text{PA} = 129^\circ$; Mason et al. 2001). Adopting fiducial masses of $M_A = 0.78 M_\odot$ (Aguilera-Gómez et al. 2018) and $M_B = 0.66 M_\odot$ (Gentile Fusillo et al. 2019), and assuming the projected separation is representative of the semimajor axis, one would estimate a system mass of $\sim 1.44 M_\odot$, orbital period of ~ 1470 yr, and approximate orbital velocities of ~ 1.4 and ~ 1.6 km s $^{-1}$ for A and B, respectively.

Analysis using RVSearch fits the RV data using a linear trend rather than a Keplerian orbit. The signal is very evident in the RV time series, and we recover a best-fit trend of 0.00482 ± 0.00022 m s $^{-1}$ day $^{-1}$ for HD 100623.

We assert that this signal is due to the companion, but our observation baseline is obviously not long enough to constrain its orbit well. Rosenthal et al. (2021) also reported a long-term linear trend of $\dot{\gamma} = 0.00475 \pm 0.00028$ m s $^{-1}$ day $^{-1}$ (1.73 ± 0.10 m s $^{-1}$ yr $^{-1}$), which is consistent with our result, suggesting that our two signal detections are likely being caused by the same source.

Additionally, we report one significant signal in the S-index activity analysis, with parameters $P = 3729 \pm 89$ days and $e = 0.288 \pm 0.073$. The peak is fairly well defined, and the long period makes this detection a plausible new magnetic activity cycle.

6.9. HD 131977 (GJ 570A)

HD 131977 (GJ 570 A, HR 5568, HIP 73184, KX Lib, Lalande 27173) is the primary in a complicated multiple star system with at least two other stellar companions situated $24''$ away (HD 131976, resolved into the M dwarf pair GJ 570B and C; Forveille et al. 1999), and a distant substellar companion, GJ 570D, $274''$ away (Burgasser et al. 2000). HD 131977 is 5.89 pc away ($\varpi = 169.8843 \pm 0.0653$ mas; Gaia Collaboration et al. 2021a) and classified K4V (Keenan & McNeil 1989). There are two published rotation periods, $P_{\text{rot}} = 44.6$ days Cincunegui et al. (2007) and 39.993 days Fuhrmeister et al. (2022). There is a surprisingly wide range of quoted metallicities for HD 131977, ranging from $[\text{Fe}/\text{H}] = -0.24 \pm 0.05$ (Mishenina et al. 2012) to 0.12 ± 0.03 (Valenti & Fischer 2005).

Through analysis with RVSearch, we recover only a linear trend for this system, likely attributable to one of the (sub) stellar companions. There are only 55 data points for this target,

all from HARPS, spanning ~ 6 yr. Because of these constraints, it is unsurprising that we do not recover full stellar companion orbits for this system, and we recommend further observations to better constrain the parameters of the system.

Our S-index analysis returns three significant detections. The first detection has $P = 22.7657 \pm 0.0049$ days, which we note is half the rotation period published by Cincunegui et al. (2007). Detection of a $P_{\text{rot}}/2$ signal can be caused by stellar spots on different hemispheres of the star being observed over multiple observing seasons, and so we attribute this signal to stellar rotation. The other two signals are extremely short-period ($P = 3.87799 \pm 0.00054$ days and $P = 2.08913 \pm 0.00044$ days), and we suspect that the relatively small amount of data for this target stretched over 6 yr allows for Keplerian signals to fit multiple short-period cycles to the sparse sampling. We disregard these signals from being astrophysically significant at this point in time, and recommend more observations of this target to better characterize the star's activity.

6.10. HD 140901 (GJ 599 A)

HD 140901 (GJ 599 A, HR 5864, HIP 77358) is a G7IV-V type star (Gray et al. 2006) with a high proper motion. It is located at $d = 15.25$ pc ($\varpi = 65.5889 \pm 0.0342$ mas; Gaia Collaboration et al. 2021a), and has a $14''.6$ separation white dwarf companion HD 140901B (GJ 599 B). It is slightly cooler than the Sun ($T_{\text{eff}} = 5602 \pm 14$ K), and slightly more metal-rich at $[\text{Fe}/\text{H}] = 0.10 \pm 0.02$ (Soubiran et al. 2022). There are no confirmed planets or published rotation periods for this star.

Using the average $\log R'_{\text{HK}}$ value from Gomes da Silva et al. (2014), color from Hipparcos ($B - V = 0.715$), and the activity-rotation calibration from Mamajek & Hillenbrand (2008), we predict that the rotation period of the star would be $P_{\text{rot}} \simeq 21.5$ days.

Our RV analysis in RVSearch recovers one signal, with $P = 5084 \pm 1200$ days, $K = 11.6 \pm 2.4$ m s $^{-1}$, and $e = 0.44 \pm 0.25$. S-index analysis does not return any significant detections. The majority of our RV data comes from UCLES, and because we do not have S-index activity data from this instrument, it makes sense that we do not see this same RV signal within the S-index data.

H α data analysis recovers two significant detections. The first of these signals is too long period to be well constrained by the Keplerian fit, because its duration is on par with the UCLES data observation baseline, so we defer to the original periodogram peak as the best estimator of this signal: $P_I = 5431.8$ days. This period agrees well with our RV detection, but because it also aligns with the long-period trend present in all of the UCLES data, we refrain from concluding definitively that RV Signal I is caused by magnetic activity. We classify it instead as SRC and recommend further study of this target to confirm the source of this signal.

The second H α signal has parameters $P_{II} = 19.986 \pm 0.019$ days and $e_{II} = 0.27 \pm 0.19$. This is in good agreement with our prediction of a 21.5 day rotation period. We report H α activity signal II as a measurement of this star's rotation period.

6.11. HD 146233 (18 Sco)

18 Sco (HD 146233, GJ 616, HR 6060, HIP 79672) is a well-characterized solar twin and G2Va spectral standard star (Keenan & McNeil 1989) at $d = 14.13$ pc

($\varpi = 70.7371 \pm 0.0631$ mas; Gaia Collaboration et al. 2021a). Spina et al. (2018) reported stellar parameters extremely similar to those of the Sun: $T_{\text{eff}} = 5808 \pm 3$ K, $\log g = 4.440 \pm 0.009$, $[\text{Fe}/\text{H}] = +0.041 \pm 0.003$, $\tau = 4.0 \pm 0.4$ Gyr, and $M = 1.022 \pm 0.004 M_{\odot}$. The star also has both rotation ($P_{\text{rot}} = 22.9$ days; Vidotto et al. 2014) and chromospheric activity levels ($\log R'_{\text{HK}} = -4.919$; Meunier et al. 2017) very similar to the Sun as well. Lovis et al. (2011) reported a magnetic activity cycle of $P_{\text{cyc}} = 2803^{+2663}_{-392}$ days, with predicted rotation period $P_{\text{rot}} = 23.8 \pm 3.2$ days based on the mean activity level ($\log R'_{\text{HK}} = -4.923$). Boro Saikia et al. (2018) reported a period of $P_{\text{rot}} = 22.7$ days and activity cycle of $P_{\text{cyc}} = 11.36 \pm 1.23$ yr. It has no reported exoplanets.

We find three RV signals within this system: $P_I = 2374 \pm 47$ days, $K_I = 5.47 \pm 0.33$ m s $^{-1}$, $e_I = 0.21 \pm 0.07$; $P_{II} = 6256 \pm 370$ days (17.1 ± 1.01 yr), $K_{II} = 4.96 \pm 0.57$ m s $^{-1}$, $e_{II} = 0.59 \pm 0.06$; and $P_{III} = 19.8777 \pm 0.0062$ days, $K_{III} = 1.73 \pm 0.26$ m s $^{-1}$, $e_{III} = 0.38 \pm 0.16$. Additionally, there is one signal in the residuals periodogram at $P = 10.5$ days that falls just below the detection threshold.

Butler et al. (2017) reported a planet candidate at roughly the same period as our Signal I ($P_{\text{Butler}} = 2528.8 \pm 105.5$ days) and an S-index periodicity of 4190 days in their HIRES data. Our detection of $P_I = 2374 \pm 47$ days corresponds directly to a signal recovered in the S-index activity data ($P = 2812 \pm 290$ days), so we report this signal as an update to the magnetic activity cycle in Table 9. We also note the existence of a broad peak in the H α periodogram at around 2000 days, which further supports our conclusion that this signal is caused by magnetic activity rather than a planet, as proposed by Butler et al. (2017). The discrepancy between our analysis and that of Butler et al. (2017) comes from their work including only data from HIRES, while ours incorporates HARPS, HIRES, PFS, and UCLES. Our signal is mainly driven by HARPS, and comparatively, the error bars on the HIRES measurements are significantly larger. It makes sense that we recover the activity detection while the HIRES-only work did not. This is confirmed by Rosenthal et al. (2021), who reported a similar signal with $P = 2426.0^{+60.0}_{-42.0}$ days as an activity cycle as well.

We believe the 6256 day signal to be activity as well, due to its long period and periodogram peak shape. The S-index activity data also yields a significant detection at $P = 5272 \pm 1500$, which corresponds well to this LPS. They are not exact matches, but the presence of a 5000 day signal in both data sets further supports the conclusion that this signal is caused by magnetic activity.

RV Signal III has parameters $P_{III} = 19.877 \pm 0.0062$ days, $K_{III} = 1.73 \pm 0.26$ m s $^{-1}$, and $e = 0.38 \pm 0.16$. Rotation periods reported by Lovis et al. (2011) and Vidotto et al. (2014) are both >20 days, and this signal is fit to extremely high precision to 19.877 days. A signal caused by rotation should also appear in the Ca H&K data, but there is no strength in the S-index periodogram around 19 days. Additionally, the periodogram peak is very sharp and well defined, which would be highly unusual if the signal was caused by rotation. Rotation signals in RV come from observing stellar spots as the star rotates, and spots migrate and change slightly over time, so we expect to see some level of imprecision or variation in these RV measurements. The definition in this periodogram peak suggests no variation in the period over our approximately 20 yr observation baseline, which is highly unusual. We therefore

classify this signal as a Candidate, and recommend further study of this signal to confirm whether it is planetary in origin.

Though it is not fit by *RVSearch*, we note that the 10.5 day peak in the residual periodogram is also very well defined and extremely close to the FAP line. A future, more in-depth study of this target could investigate this signal further to address the cause of this significant period.

Analysis of $H\alpha$ activity from the UCLES instrument returns no significant detections.

6.12. HD 188512 (β Aql)

β Aql (HD 188512, GJ 771 A, HR 7602, HIP 98036, Alshain) is a high proper-motion star at $d = 13.69$ pc ($\varpi = 73.00 \pm 0.20$ mas; van Leeuwen 2007), and is the primary spectral standard for type G8IV (Johnson & Morgan 1953; Keenan & McNeil 1989). The star is the most luminous star in our sample, and is somewhat cooler than the Sun ($T_{\text{eff}} = 5117 \pm 10$ K), less metal-rich ($[\text{Fe}/\text{H}] = -0.19 \pm 0.01$), and somewhat evolved with a lower surface gravity ($\log g = 3.64 \pm 0.03$; Maldonado & Villaver 2016). Butkovskaya & Plachinda (2017) reported a magnetic activity cycle of $P_{\text{cyc}} = 969 \pm 27$ days (2.653 ± 0.074 yr) and a surprisingly short rotation period of $P_{\text{rot}} = 5.08697 \pm 0.00031$ days. Corsaro et al. (2012) reported asteroseismic analysis of RV data for β Aql showing intranight oscillations at the ~ 5 – 10 m s^{-1} amplitude level. The star appears to be an evolved star somewhat more massive than the Sun ($1.36 \pm 0.17 M_{\odot}$, $1.337 \pm 0.021 M_{\odot}$; Corsaro et al. 2012; Gomes da Silva et al. 2021); hence, the relatively fast rotation for a subgiant likely reflects that the star spent its main-sequence life blueward of the Kraft break. The star appears to be consistent with being an intermediate-mass star, with isochronal age estimates consistently slightly younger than the Sun (~ 3 – 4 Gyr; Maldonado et al. 2013; da Silva et al. 2015; Jofré et al. 2015; Brewer et al. 2016; Gomes da Silva et al. 2021), and chromospheric age estimates that had assumed that the star was a typical solar-type dwarf (9.6, 11.4 Gyr; Mamajek & Hillenbrand 2008) are likely to be significantly overestimated.

After finding and subtracting a linear trend ($0.00225 \text{ m s}^{-1} \text{ day}^{-1}$) in the California Planet Search data set for β Aql A, Luhn et al. (2020) reported a Doppler signal “*b*” with $P = 10524.603$ days and velocity amplitude $K = 5.43 \text{ m s}^{-1}$, which would correspond to an $m \sin i = 0.167 M_{\text{J}}$ companion at $a = 10.18$ au. β Aql is in the Washington Double Star Catalog (Mason et al. 2001) with components A, B, and C (WDS J19553+0624 = STT 532), although component C at separation $214''$ (TYC 493-72-1) is reported to be an unrelated interloper (Kiyaeva et al. 2008). β Aql B is an M2.5V star (Montes et al. 2018) at a projected separation $13''.27$ (182 au), and clearly a physical companion sharing similar proper motion and parallax ($\varpi = 73.3889 \pm 0.0215$ mas; Gaia Collaboration et al. 2021a). Kervella et al. (2022) reported that the inferred tangential velocity calculated from Gaia EDR3 astrometry differs from that of β Aql A by only 1.60 km s^{-1} . However, the astrometric perturbation on β Aql A, in the form of the tangential velocity anomaly as estimated through comparing Hipparcos and Gaia astrometry, appears to be negligible ($5.74 \pm 10.65 \text{ m s}^{-1}$; Kervella et al. 2022).

Analysis of two decades’ worth of RV data with *RVSearch* returns a linear trend rather than a full Keplerian signal. We find a best-fit RV trend of $0.00262 \text{ m s}^{-1} \text{ day}^{-1}$, in good agreement with the Luhn et al. (2020) result. The long-period

trend is undoubtedly associated with the perturbation induced by the M dwarf companion B at separation at ~ 180 au. As the position angle of the β Aql binary has changed by only 23° between 1838 and 2016, this suggests the AB orbital period to be of the order of a few thousand years.

Analysis of the S-index data for this target returns no significant detections. The star does not have any UCLES observations, so there are no $\text{EW}_{H\alpha}$ measurements to study.

6.13. HD 190248 (δ Pav)

δ Pav (HD 190248, GJ 780, HR 7665, HIP 99240) is a G8IV (Gray et al. 2006) star at $d = 6.10$ pc ($\varpi = 163.9544 \pm 0.1222$ mas; Gaia Collaboration et al. 2021a) and chromospherically quite inactive ($\log R'_{\text{HK}} = -5.10$; Gomes da Silva et al. 2014). Ramírez et al. (2013) reported the star to have $T_{\text{eff}} = 5517 \pm 60$ K, $\log g = 4.28 \pm 0.03$, and to be fairly metal-rich ($[\text{Fe}/\text{H}] = 0.33 \pm 0.07$). The star’s rotation period has been estimated to be $P_{\text{rot}} = 21.4 \pm 9.3$ days (Hojjatpanah et al. 2020).

RVSearch identifies one Keplerian signal in the combined RV data for this star, with $P_1 = 360.8 \pm 1.9$ days and $K = 1.21 \pm 0.43 \text{ m s}^{-1}$. The HARPS and UCLES data exhibit significant disagreements with one another in the phase-folded plot, however, and the signal seems to be driven strongly by the seasonality of the HARPS data as evidenced by the sudden increase in the strength of the signal as a function of observation (see HD 190248’s *RVSearch* final summary in the accompanying figure set). We therefore suspect that this signal is due to observational sampling effects and not a planet.

RVSearch also detects a linear trend in the data, with $dv_r/dt = -0.00055 \pm 0.00009 \text{ m s}^{-1} \text{ day}^{-1}$ ($-0.201 \pm 0.033 \text{ m s}^{-1} \text{ yr}^{-1}$). Such trends are often suggestive of long-period substellar or giant planet companions. We can compute initial estimates of the minimum mass and semimajor axis for this companion by considering the linear trend to fall in the nonquadrature portion of an RV phase curve. In this case, we assume that the period of such a companion must be at least twice our observational baseline, as otherwise we would have expected to see some level of quadratic or sinusoidal curvature by now, and that its RV semiamplitude must be at least half of the total RV span covered by the linear trend in the data set. That sets $P_{\text{min}} = 37$ yr and $K_{\text{min}} = 1.85 \text{ m s}^{-1}$. Folding in our knowledge of the host star’s stellar mass, $M_{\star} = 1.001 M_{\odot}$, we find that the planet must be at least $69 M_{\oplus}$ ($0.22 M_{\text{Jup}}$) and on an orbit with a minimum semimajor axis $a_{\text{min}} = 11.1$ au. Comparing with the *RVSearch* injection/recovery summary plot, this combination of planet mass and orbital distance falls into a region that is not reliably recovered, and so it is not surprising that the potential companion inducing this signal is not yet detectable with our current RV data set.

Makarov et al. (2021) recently reported the detection of an astrometric perturbation for δ Pav that they interpret as being likely due to a long-period giant planet. They compare the short-baseline Gaia EDR3 proper motions (Gaia Collaboration et al. 2021a) for δ Pav with long baseline astrometric parameters (~ 22 – 26 yr) combining Hipparcos with ground-based astrometry USNO Robotic Astronomic Telescope (URAT; Zacharias et al. 2015). Combining the Gaia EDR3, Hipparcos, and URAT data, Makarov et al. (2021) estimated the perturbation of the tangential velocity for δ Pav to be $(17.4, -13.2) \text{ m s}^{-1}$ in α and δ , respectively (0.995 and 0.958 confidence levels). Removing the ground-based data, and using only Hipparcos and Gaia EDR3,

Makarov et al. (2021) found the signal to be small but still significant: $(7.7, -6.2) \text{ m s}^{-1}$ in α and δ , respectively (at combined confidence level 0.999). Simply subtracting the proper motions from Hipparcos (epoch 1991.5) from Gaia EDR3 (epoch 2016.0) yields $\Delta\mu_\alpha, \Delta\mu_\delta = 0.731 \pm 0.149, -0.187 \pm 0.167 \text{ mas yr}^{-1}$, which at the distance of $d = 6.099 \text{ pc}$ ($1/\varpi$ from Gaia EDR3) yields differences in the tangential motions of $21.1 \pm 4.3, -5.4 \pm 4.8 \text{ m s}^{-1}$ in α and δ , respectively. Over the 24.5 yr baseline between the mean epochs for Hipparcos and Gaia EDR3, the averaged tangential accelerations are then $a_\alpha, a_\delta = 0.861 \pm 0.176, -0.220 \pm 0.196 \text{ m s}^{-1} \text{ yr}^{-1}$, or total tangential acceleration $a_{\text{tan}} = 0.889 \pm 0.263 \text{ m s}^{-1} \text{ yr}^{-1}$. Combining the measured radial acceleration ($a_{\text{rad}} = -0.201 \pm 0.033 \text{ m s}^{-1} \text{ yr}^{-1}$) with the tangential acceleration (a_{tan}) yields a total inferred acceleration on δ Pav of $a_{\text{tot}} = 0.911 \pm 0.265 \text{ m s}^{-1} \text{ yr}^{-1}$ ($2.89 \pm 0.84 \times 10^{-8} \text{ m s}^{-2}$).

Analysis of S-index data returns one significant period, with an initial ΔBIC periodogram peak at 6375 days and an initial MAP fit of 6810.18 days. This is suggestive of a ~ 17 yr magnetic cycle, but attempts to fully characterize the signal via RVSearch’s MCMC analysis fail—likely due to insufficient sampling of the full orbital phase space. We therefore note the signal as an “LPS” in the S-index detections table and report just the MAP period, but encourage further monitoring of this star in the coming years to help fully resolve the star’s long-term magnetic activity.

The star’s $\text{EW}_{\text{H}\alpha}$ data contains two significant signals according to RVSearch, one with a period $P = 352.9 \pm 1.5$ days, and the other with $P = 1171 \pm 36$ days. The first signal suffers from the star’s seasonal availability, leaving $\sim 1/3$ of its orbital phase curve much less populated than the rest, and we suspect this is due to observational cadence constraints. The longer-period signal is well defined in the ΔBIC periodogram but falls logarithmically between the periods expected for the star’s rotation period and its potential magnetic cycle. As HD 190248 is a very inactive star, much like the Sun at solar minimum, this ~ 1200 day signal prompts a question of whether we are seeing less-obvious activity phenomena (e.g., meridional flows Meunier & Lagrange 2020) that operate on intermediate timescales.

6.14. HD 207129 (GJ 838)

HD 207129 (GJ 838, HR 8323, HIP 107649) is a nearby star at distance $d = 15.56 \text{ pc}$ ($\varpi = 64.2717 \pm 0.0430 \text{ mas}$; Gaia Collaboration et al. 2021a) classified as G0V Fe+0.4 (Gray et al. 2006), and is famous for having a resolved dusty debris disk (Jourdain de Muizon et al. 1999; Krist et al. 2010). The star is a dwarf ($\log g = 4.49 \pm 0.02$) of solar metallicity ($[\text{Fe}/\text{H}] = 0.00 \pm 0.01$), just slightly hotter than the Sun ($T_{\text{eff}} = 5937 \pm 13 \text{ K}$; Sousa et al. 2008). Marshall et al. (2011) estimated the rotation period of the star to be $P_{\text{rot}} \simeq 12.6$ days based on the star’s $v \sin i$. Watson et al. (2011) and Lovis et al. (2011) predicted the rotation period to be $P_{\text{rot}} = 17.13 \pm 1.61$ days and 17.6 ± 2.8 based on the star’s chromospheric activity. Lovis et al. (2011) reported a magnetic activity cycle with period $P_{\text{cyc}} = 1520_{-139}^{+171}$ days using 79 observations of $\log R'_{\text{HK}}$ measured over an 1876 day span.

We recover one significant RV signal, with parameters $P = 1964 \pm 49$ days ($5.38 \pm 0.134 \text{ yr}$), $K = 4.02 \pm 0.61 \text{ m s}^{-1}$, and $e = 0.44 \pm 0.16$.

We find a single significant signal in the S-index analysis, with an initial periodogram peak of $P_I = 1886$ days, and an

MAP fit of 1898 days. This signal does not converge when subjected to RVSearch’s affine-invariant sampling, and so we interpret it as an LPS. Despite this, the MAP period of the S-index is within 2σ of the signal detected in the RVs, and so we report RV Signal I as a magnetic activity cycle. Our estimate of the activity cycle period is marginally consistent with that reported by Lovis et al. (2011; 2.2σ difference). Our signal has a longer period than the baseline of the Lovis et al. (2011) study, and so this difference between our best-fit models does not raise significant concerns.

The $\text{EW}_{\text{H}\alpha}$ data for this star produces two significant detections, the first at $P_I = 5455 \pm 1900$ days and the second at $P_{II} = 1726 \pm 71$ days. The longer signal is close to the UCLES observational baseline extent and has a large uncertainty, so we interpret it as an LPS and do not assume that it is astrophysical in nature. The second signal, however, is well defined in period and similar in duration to both the Lovis et al. (2011) $\log R'_{\text{HK}}$ detection and our own S-index detections. We therefore consider it to be additional evidence for a long-period magnetic cycle in the star.

Given these S-index and $\text{H}\alpha$ detections, we report RV Signal I as an update to the previous, magnetic cycle driven, detection.

7. Targets Lacking RV Signals

For the remaining 16 stars included in this study, RVSearch did not recover any significant signals in the radial velocities. We further subdivide these targets into Section 7.1, stars that returned only significant activity signals, and Section 7.2, targets that failed to return any significant signals in either the RVs or the activity. Many of these had a very limited number of RV measurements. Future RV surveys should focus primarily on these targets in order to build knowledge of their exoplanetary parameter space. The stars with no significant RV signals but a nonzero number of activity detections are listed in Table 10. Stars with no detections at all are listed in Table 11. The number of measurements analyzed for each of these stars can be found in Table 2.

7.1. Targets with Activity Detections Only

7.1.1. HD 4628 (GJ 33)

HD 4628 (GJ 33, HR 222, HIP 3765, Lalande 1299, Wolf 25) is a metal-poor ($[\text{Fe}/\text{H}] = -0.24 \pm 0.03$; Takeda et al. 2005) K2V star (Gray et al. 2003) at only $d = 7.43 \text{ pc}$ ($\varpi = 134.4948 \pm 0.0578 \text{ mas}$; Gaia Collaboration et al. 2021a). The star is fairly slow rotating, with differential rotation observed (seasonal periods ranging from 37.2–41.4 days) and mean $P_{\text{rot}} \simeq 38.5$ days (Donahue et al. 1996). Analysis of the Mt. Wilson survey data by Donahue (1996) yielded a mean cycle period of $P_{\text{cyc}} = 8.6 \text{ yr}$ (~ 1966 –1995), and subsequent analysis of a longer baseline by Garg et al. (2019) yielded cycle periods of $P_{\text{cyc}} = 8.67, 8.08, \text{ and } 9.98 \text{ yr}$ (mean $P_{\text{cyc}} = 8.91 \text{ yr}$). Boro Saikia et al. (2018) estimated the chromospheric activity cycle to be $P_{\text{cyc}} = 8.47 \pm 0.05 \text{ yr}$.

We recover one significant detection in the S-index data and none in the RVs. The fitted signal has $P = 3699 \pm 310$ days and eccentricity $e = 0.33 \pm 0.12$. This appears to correspond to the activity cycle for the star ($P_{\text{cyc}} = 10.90 \pm 0.41 \text{ yr}$), although somewhat longer than the cycle periods reported by the longer baseline Mt. Wilson survey data (Donahue 1996; Garg et al. 2019).

Table 10
Targets with Activity Detections Only

Identifier	Identifier	Identifier
HD 4628	HD 14412	HD 30495
HD 50281	HD 72673	HD 125072
HD 149661	HD 156026	HD 216803

Note. Stars from our sample for which RVSearch did not detect any significant RV signals, but did return significant detections in their S-index or EW_{H α} analyses. Activity detections can be found in Tables 6 and 7.

Table 11
Targets with No Significant Signals

Identifier	Classification	Rms (m s ⁻¹)
HD 693	ID	2.81
HD 7570	NS	5.68
HD 22484	NS	3.50
HD 23356	NS*	5.27
HD 76151	ID	8.97
HD 102870	NS	5.41
HD 131977	ID	6.93
HD 196761	NS*	4.60

Note. Stars from our sample for which RVSearch did not detect any significant signals. (*): Targets marked with an asterisk have strong signals in their periodogram that almost cross the detection threshold; these are discussed more in depth in Section 7.2).

7.1.2. HD 14412 (GJ 95)

HD 14412 (GJ 95, HR 683, HIP 10798) is a G8V type star (Gray et al. 2006) at $d = 12.83$ pc ($\varpi = 77.9140 \pm 0.0295$ mas; Gaia Collaboration et al. 2021a). Rotation period P_{rot} estimates for HD 14412 range from 13.0 ± 0.3 days (Hojjatpanah et al. 2020) to 29 days (Isaacson & Fischer 2010; from $\log R'_{\text{HK}}$); however, the 13 day estimate seems surprisingly fast given the star’s low chromospheric activity ($\log R'_{\text{HK}} = -4.839$; Isaacson & Fischer 2010).

We recover two significant S-index activity signals for this star: $P_I = 2312 \pm 73$ days, $e_I = 0.091 \pm 0.098$ and $P_{II} = 5686 \pm 1600$ days, $e_{II} = 0.5 \pm 0.16$. The RV periodogram returns no significant detections but does contain one strong peak just under the detection threshold, with $P = 2074.5$ days. Howard & Fulton (2016) presented an S-value periodogram for HD 14412, showing a pronounced peak at 5.7 yr (2082 days). We report our Activity Signal I to have a magnetic activity cycle of $P_{\text{cyc}} = 2312 \pm 73$ days (6.33 ± 0.2 yr), fairly consistent with that reported by Howard & Fulton (2016). We suspect S-index activity signal II is caused by a magnetic activity cycle as well, due to the long period and broad shape of the peak.

7.1.3. HD 30495 (58 Eri)

58 Eri (HD 30495, GJ 177, HR 1532, HIP 22263, IX Eri) is a nearby star at distance 13.24 pc ($\varpi = 75.5289 \pm 0.0539$ mas; Gaia Collaboration et al. 2021a) classified as G1.5V CH-0.5 (Gray et al. 2006). The star is a young (~ 1 Gyr) solar analog, with a rotation period $P_{\text{rot}} = 11.36 \pm 0.17$ days, and manifesting both short (~ 1.7 yr) and long (~ 12.2 yr) activity cycles (Egeland et al. 2015). Gaidos et al. (2000) reported time series photometry

over six seasons, finding periods between 10.5 and 11.47 days, and reporting a mean rotation period of $P_{\text{rot}} = 11.3$ days.

RVSearch found no significant signals in the RV data, but one significant signal in the S-index activity data with $P = 71.46 \pm 0.11$ days, $e = 0.31 \pm 0.12$. There is a correlated peak in the RV residual periodogram at 72 days, although it does not rise to the level of being a “significant detection.” This signal does not correspond to the published rotation period, nor to either of the published activity cycles referenced above. Because of this, we classify this signal as SRC and recommend further study of the activity data for this target in a future work.

7.1.4. HD 50281 (GJ 250A)

HD 50281 (GJ 250A, HIP 32984) is a K3.5V star (Gray et al. 2003) at $d = 8.74$ pc ($\varpi = 114.3547 \pm 0.0418$ mas; Gaia Collaboration et al. 2021a). The star is in a wide binary (separation 58.9; Mason et al. 2001) with the M dwarf GJ 250B. HD 50281 is an active star ($\log R'_{\text{HK}} = -4.554$; Gondoin 2020), and Fuhrmeister et al. (2022) predicted a rotation period of $P_{\text{rot}} = 16.493$ days based on the chromospheric activity.

Analysis of the RV periodogram yielded no significant signals. The time series data in Ca H & K shows a very complicated periodic pattern that resulted in seven significant periodic signals detected. As the last couple appear amid a forest of slightly lower power peaks, we believe that our statistical criterion may be inadequate for this very active star and picking out true signals from background noise. We focus on the interpretation of the first five prominent peaks, which had periods of 2264 ± 11 days, 2102 ± 12 days, 139.42 ± 0.05 days, 12.47954 ± 0.00046 days, and 16.49842 ± 0.00089 days. The first three have similar semiamplitudes in ΔS at the ~ 0.05 – 0.10 level, and appear to be attempts by our code to fit a single complicated activity cycle of $P_{\text{cyc}} \simeq 2264$ days, which is inadequately fit by a single Keplerian orbit model. The latter two are well defined and similar to the predicted rotation period from Fuhrmeister et al. (2022). Hence, we consider the 12.5 and 16.5 day signals to be from differential rotation.

7.1.5. HD 72673 (GJ 309)

HD 72673 (GJ 309, HIP 41926) is a K1V star (Keenan & McNeil 1989), with no known companions or planets. The star is fairly inactive ($\log R'_{\text{HK}} = -4.968$) with a slow predicted rotation period ($P_{\text{rot}} = 40.2 \pm 4.1$ days; Lovis et al. 2011).

We recover no significant RV signals but one S-index and one H α activity detection. The S-index activity detection has parameters $P = 3217 \pm 200$ days and $e = 0.14 \pm 0.14$. This signal matches the previously reported magnetic activity cycle period reported by Lovis et al. (2011; $P_{\text{cyc}} = 3050^{+558}_{-408}$ days), although the uncertainty in our cycle period is seven times smaller. We therefore report our detection as an update to this previously published magnetic activity cycle.

The H α activity detection has a much shorter period, with parameters $P = 341.2 \pm 3.6$ days and $e = 0.16 \pm 0.18$. This is obviously very close to 1 yr, indicating a strong possibility that this signal is being driven by windowing effects similar to with the HARPS instrument. The peak is extremely well defined, however, and highly significant, so we refrain from decisively calling this detection a false positive.

7.1.6. HD 125072 (GJ 542)

HD 125072 (GJ 542, HIP 69972) is a K3V (Houk & Cowley 1975) star at $d = 11.82$ pc ($\varpi = 84.6029 \pm 0.0218$ mas; Gaia Collaboration et al. 2021a). Gray et al. (2003) classified the star as K3IV subgiant; however, the star's spectroscopic parameters ($T_{\text{eff}} = 4899 \pm 48$ K, $\log g = 4.55 \pm 0.03$, $[\text{Fe}/\text{H}] = 0.28 \pm 0.08$; Ramírez et al. 2013) and HR diagram position ($B - V = 1.03$, $M_V = 6.30$, ~ 0.44 mag above the main sequence) clearly flag it as a very metal-rich dwarf.

Lovis et al. (2011) reported a magnetic activity cycle of $P_{\text{cyc}} = 1146^{+982}_{-70}$ days and a predicted rotation period of 42.0 ± 5.9 days based on the low mean activity level ($\log R'_{\text{HK}} = -4.941$).

We recover no significant RV signals, two detections in the S-index activity data, and one in the $\text{EW}_{\text{H}\alpha}$ data. S-index signal I, with $P_I = 2989 \pm 100$ days, loosely correlates with the magnetic activity cycle of Lovis et al. (2011). S-index signal II has $P_{\text{II}} = 40.49 \pm 0.036$ days, which is most likely caused by stellar rotation, and agrees well with the predicted cycle from Lovis et al. (2011).

The $\text{EW}_{\text{H}\alpha}$ data analysis yields one significant detection with an initial ΔBIC period of 5468.5 days, but fails to produce a well-constrained orbital fit during the MCMC analysis (instead giving $P = 9483 \pm 9400$ days). We therefore instead report the MAP best-fit solution, which has a period of 7137.76 days, which we attribute to the long-period UCLES trend present in almost all of the $\text{H}\alpha$ data for all targets.

We note additionally the presence of a signal in the RV residual periodogram that falls just below the detection threshold, at $P = 13.5$ days.

7.1.7. HD 149661 (12 Oph)

12 Oph (HD 149661, GJ 631, HR 6171, HIP 81300, V2133 Oph) is a K0V(k) (Gray et al. 2006) star at $d = 9.89$ pc ($\varpi = 101.0719 \pm 0.0501$ mas; Gaia Collaboration et al. 2021a). The star has dwarf surface gravity ($\log g = 4.52 \pm 0.02$) and metallicity just slightly more than solar ($[\text{Fe}/\text{H}] = 0.03 \pm 0.01$; Soubiran et al. 2022). Analysis of chromospheric activity levels ($\log R'_{\text{HK}}$ index) show that it varies widely over the past several decades. During the Mt. Wilson survey period of 1967–1983, the star had an average $\log R'_{\text{HK}}$ value of -4.583 (Baliunas et al. 1996); however, the survey by Radick et al. (2018) during 1994–2016 recorded an average of $\log R'_{\text{HK}} = -4.71$, while analysis of HARPS observations during 2005–2012 by Gomes da Silva et al. (2021) estimated a median activity level of $\log R'_{\text{HK}} = -4.56$. From analysis of the Mt. Wilson HK survey data, Donahue et al. (1996) reported an average rotation period over nine seasons of $P_{\text{rot}} = 21.07$ days, with individual seasonal rotational periods ranging between 20.6 and 22.9 days. Boro Saikia et al. (2018) reported two Ca HK activity cycles with periods $P_{\text{cyc}} = 15.3 \pm 0.4$ yr and $P_{\text{cyc}} = 7.7 \pm 0.12$ yr.

Analysis of both RV and $\text{H}\alpha$ data returns no detections for this target, but the S-index search yields two significant signals: $P_I = 1649 \pm 55$ days, $e_I = 0.42 \pm 0.12$; $P_{\text{II}} = 3874 \pm 1200$ days, $e_{\text{II}} = 0.73 \pm 0.21$. The first of these signals is likely to be a magnetic activity cycle, based on its long period and signal strength. The second signal is poorly constrained—the periodogram peak being fit is at 4062.0 days, which is approximately half of the observation baseline. *RVSearch* struggles to fit a Keplerian orbit to the signal, as there is insufficient data to

constrain the orbit very well. This signal may be evidence of a longer-period magnetic activity cycle, but additional data is needed to constrain the cycle well.

7.1.8. HD 156026 (36 Oph C)

36 Oph C (HD 156026, GJ 664, HIP 84478, V2215 Oph, WDS J17153-2636C) is a nearby (5.88 pc; $\varpi = 169.9617 \pm 0.0311$ mas; Gaia Collaboration et al. 2021b) K5V(k) (Gray et al. 2006) star, which is a very wide separation (731''54) companion to the bright K0V+K1V pair 36 Oph A & B (Cayrel de Strobel et al. 1989). The orbital motion of C around AB appears to be detectable astrometrically, as Kervella et al. (2022) showed that C shows a tangential velocity anomaly between the Hipparcos and Gaia DR3 data of 5.98 ± 1.19 m s $^{-1}$ with a vector of $\text{PA} = 87^\circ 22 \pm 7^\circ 25$ (compare to the PA between AB and C of $\text{PA} = 73^\circ 83$). The difference in tangential velocities between AB and C is 0.63 km s $^{-1}$, which is similar to the predicted escape velocity of C from AB (0.61 km s $^{-1}$; Kervella et al. 2022).

Photometric variability at the ~ 0.02 mag in the V band for 36 Oph C was reported by Lloyd Evans & Koen (1987) who estimated a period of 21.0 days. Independently, Baliunas et al. (1996) reported an identical rotation period of 21 days based on analysis of Mt. Wilson Ca II H & K observations, and an average activity level of $\log R'_{\text{HK}} = -4.662$. Boro Saikia et al. (2018) reported a Ca II H & K activity cycle period of $P_{\text{cyc}} = 21.3 \pm 0.83$ yr. 36 Oph C appears to be erroneously classified as an RS CVn variable in the General Catalog of Variable Stars (Samus' 2017) and SIMBAD,⁴⁰ and while the star is clearly spotted and active, there is no evidence of the star being a chromospherically active binary (i.e., no sign of short-period stellar binary). The RV trend is flat, with scatter at the ~ 2 m s $^{-1}$ level, consistent with the 1.57 m s $^{-1}$ jitter previously estimated by Isaacson & Fischer (2010).

The S-index data shows one significant peak at $P = 378.9 \pm 2.2$ days, which is likely caused by systematics, as the period is extremely close to 1 yr. Additionally, there are weak peaks in the residual periodogram around 4.9 days, ~ 22 days, and ~ 25 days, with the latter two suspiciously near the previously reported 2 day rotation period.

7.1.9. HD 216803 (TW PsA)

TW PsA (Fomalhaut B) is a nearby (7.60 pc; $\varpi = 131.5525 \pm 0.0275$ mas; Gaia Collaboration et al. 2021b) K4Ve (Keenan & McNeil 1989) spectral standard star that is within a very wide, young (~ 440 Myr old) triple system with Fomalhaut A and C (LP 876-10; Mamajek et al. 2013). The star has essentially solar metallicity and dwarf surface gravity ($T_{\text{eff}} = 4601 \pm 29$ K, $\log g = 4.68 \pm 0.10$, $[\text{Fe}/\text{H}] = 0.04 \pm 0.03$; Soubiran et al. 2022). The star is relatively fast-rotating ($P_{\text{rot}} = 10.3$ days, 9.87 days; Busko & Torres 1978; Wright et al. 2011) and chromospherically active ($\log R'_{\text{HK}} = -4.44$; Gomes da Silva et al. 2021). De Rosa et al. (2019) reported an astrometric acceleration of TW PsA consistent with a $1.2^{+0.7}_{-0.6}$ M_J planet on a $P_{\text{orb}} = 25^{+52}_{-21}$ yr orbit based on comparison of the Hipparcos and Gaia DR2 astrometry. However it is worth noting that an independent comparison of the Hipparcos and Gaia DR2 astrometry by Kervella et al. (2019) yielded a borderline significance tangential velocity anomaly

⁴⁰ <https://simbad.u-strasbg.fr/simbad/>

($18.67 \pm 6.39 \text{ m s}^{-1}$; 2.9σ), a subsequent analysis using improved DR3 data by Kervella et al. (2022) yielded tighter, but less significant constraints ($2.15 \pm 1.49 \text{ m s}^{-1}$; 1.4σ).

Analysis of RV and $H\alpha$ data returns no significant signals for this target. The S-index period search yields several detections: $P_I = 3.8913 \pm 0.0002$ days, $P_{II} = 4.08499 \pm 0.00049$ days, and $P_{III} = 2.8 \pm 0.3$ days. However, the S-index data for this target is fairly sparse, so RVSearch is able to fit many different short-period signals to the data easily. We do not believe that any of these signals are physically significant, and disregard them as not physically meaningful.

7.2. Targets with No Detections

Several targets included in this work did not return any significant detections in either the RVs or the activity indicators when run through RVSearch. In some cases, this is due to a lack of data on the given target. Otherwise, there are a few cases in which the target is well studied, and likely is simply a quiet system. Table 11 lists each of the stars that had no detections, and categorizes them as having insufficient data to make a detection (ID) or well studied but still contains no signal (NS). Additionally, for each target, we report mean rms. This works as a valid proxy for stellar variability, to compare with our detection results. For targets designated “ID” in the table, we recommend further study for improved completeness in the future.

Stars marked with an asterisk in Table 11 have signals that are close to but do not quite cross the detection threshold in their RV periodograms. HD 196761 shows strong periodicity around 26–28 days, which falls just short of the FAP mark. We believe this signal to be evidence of a rotation period for this target. HD 23356 has a strong peak at 2911.6 days. The observation baseline for this target is only about twice this period, so further observation of this target could constrain this signal better.

8. Discussion

In carrying out this study, we sought to characterize the planet detection completeness of nearby, Sun-like stars that have been identified as candidates for future DI observations based upon existing RV observations. We compiled archival RV data sets from the HARPS, HIRES, UCLES, PFS, and APF spectrographs to produce a reasonably complete picture of the existing precise RV sensitivity for each star. Many of the targets in this work are hosts of previously published planetary systems. Yet despite the accumulation of many additional RV data points since their first publication, the majority of these systems’ orbital parameters have not been previously updated. By utilizing the full range of archival RV data up through present day, we are able to report updated orbital parameters for many of these previously confirmed planetary systems (Table 9) and find in many cases that the uncertainties on the planets’ periods, RV semi-amplitudes, and eccentricities improve when compared to previous publications (Figure 10).

Some select highlights of our updated analyses are summarized below:

1. We provide the most precise set of orbital parameters yet published for the three Neptune-mass planets orbiting HD 69830.

2. We assert that the 40 day orbital period planet HD 20794c published in Pepe et al. (2011) is due to stellar activity and not a Keplerian signal, as its statistical significance has not increased despite the addition of hundreds of new precise RV data points.
3. We show conclusively that the 58 day rotation period planet HD 85512 b published in Pepe et al. (2011) is due to stellar activity and not a Keplerian signal, because the signal changes in period by $10+\sigma$ over the decade of data collected here.
4. We present strong evidence that the 3827 day rotation period planet HD 114613 b reported by Wittenmyer et al. (2014) is not Keplerian in nature, as its statistical significance decreases despite the addition of hundreds of precise RV measurements.
5. We improve the best-fit error bars for the period, semi-amplitude, and eccentricity of the SB1 companion to HD 160346 by over an order of magnitude.
6. We present strong evidence that the planet HD 26965 b (ρ^2 Eri b, 40 Eri b) reported by Ma et al. (2018) is not a planet, and is rather caused by stellar activity. The 42.303 day RV signal is nearly identical to a periodicity detected in $H\alpha$ of $P = 43.504 \pm 0.066$ days, which overlaps previous estimates of the star’s rotation (42–43 days; Baliunas et al. 1996; Frick et al. 2004).
7. We report three new planet candidates to be further studied and confirmed by future works: HD 43834 RV Signal I ($P_I = 359.5 \pm 1.2$ days), HD 192310 RV Signal IV ($P_{IV} = 24.559 \pm 0.016$ days), and HD 146233 RV Signal III ($P_{III} = 19.8777 \pm 0.0062$ days).

Our analysis and results thus serve as encouragement for updated analysis on other previously confirmed planetary systems in which significant amounts of new data have been acquired since publication.

In addition, we report a number of new magnetic activity cycles and signals that are not yet complete enough to be classified, all of which invite further study.

In this work, our goal was to analyze each star’s RV sensitivity completeness, so that we might make recommendations with respect to future work in preparation of a DI mission that aims to search for Earth-analog planets around these stars. As time on future DI missions is likely to be highly oversubscribed, it is imperative that their target lists be as thoroughly vetted as possible in order to increase these future missions’ efficiency and science output.

One key component of this characterization is to identify the presence of any additional planets in the system and determine whether their orbital parameters preclude the existence of the temperate, terrestrial, planets that the future DI missions seek. If such planets are detected, then these stars should be down-weighted in the mission’s observing priority list. Figures 11, 12, and Table 12 summarize our findings in this area. While it is clear from Figure 11 that even our most well-studied targets do not come close to the $1 M_{\oplus}$ limit for a 1 au orbit, we are at least able to rule out the presence of Neptune-to-Jupiter-mass planets at ~ 1 au; such bodies would eliminate the possibility of a dynamically stable Earth analog. Figure 12 shows the range of $m \sin i$ and planetary insolation of the known planets, candidates, and SRCs in this work relative to the habitable zone for an Earth-like planet around a Sun-like star as defined in Kopparapu et al. (2014); very few of our detections fall within this region.

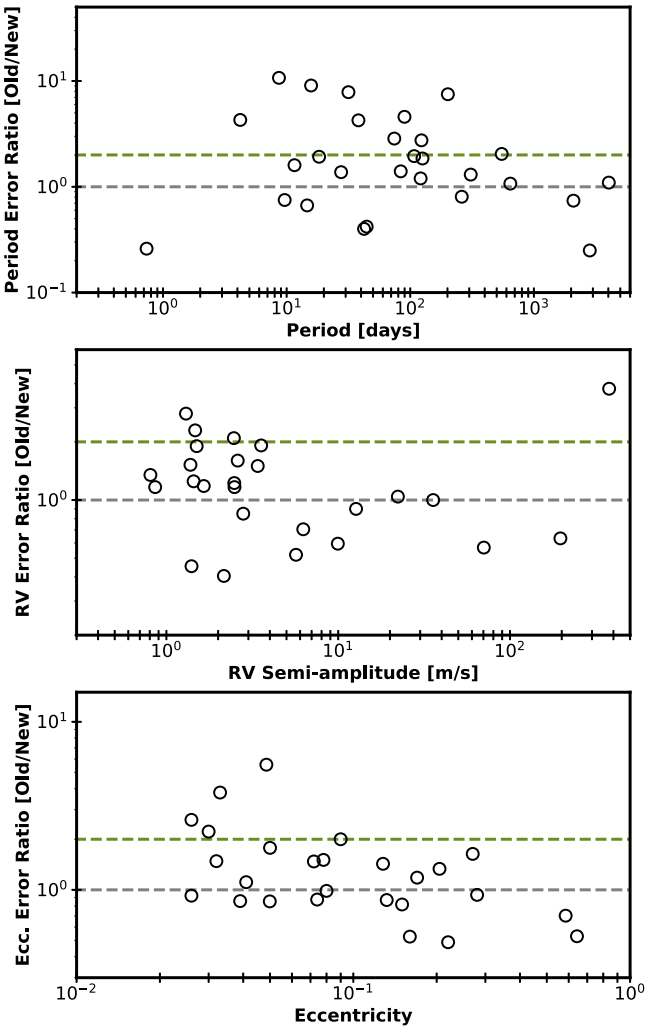


Figure 10. Comparison of the uncertainties in previously published works and our updated RV analyses for the planets listed in Table 5 for orbital period (top plot), RV semi-amplitude (middle plot), and orbital eccentricity (bottom plot). The gray dashed lines depict a 1:1 ratio, so planets above the line have more-precise results in our analysis while planets below the line have less-precise results here than previously published. The green lines denote a factor of 2 improvement, so planets above the green lines have uncertainties that decreased by 50%. This happens most commonly in the orbital period comparisons, as the additional months/years of data added here include many more orbits of each planet.

For the majority of our stars, the minimum detectable mass planet at 1 au is well above the mass of Neptune or even Saturn. And in some cases, where the stars have only a handful of existing RV observations, even a stellar companion could remain hidden in the data. We therefore recommend further study of all targets on this list. Future surveys could focus most strongly on those that have the least RV sensitivity in the 1 au region.

The stars with the least RV sensitivity, for this study, are those with the smallest number of RV observations. Our list contains nine stars with under 50 RV epochs: HD 693 (16 epochs), HD 30495 (50 epochs), HD 76151 (seven epochs), HD 131977 (22 epochs), HD 147584 (one epoch), HD 160346 (34 epochs), HD 165341 (seven epochs), HD 203608 (one epoch), and HD 216803 (42 epochs). We recommend that future RV surveys focus strongly on these 16 targets, in order to build up their RV baseline and thus increase RV sensitivity.

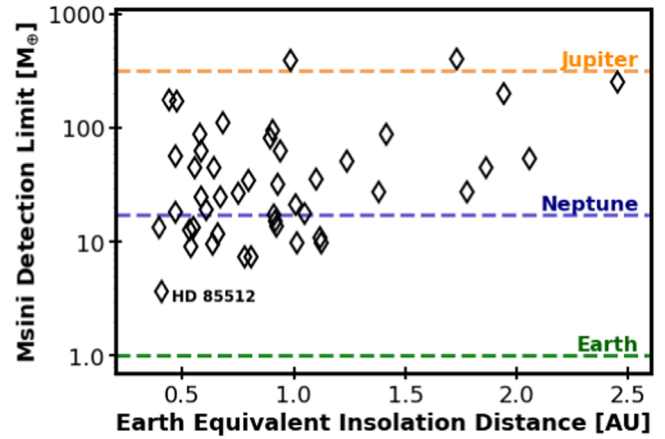


Figure 11. Fifty percent detection sensitivity threshold for each target star at its Earth equivalent irradiation distance (EEID)—the distance from the host star at which the planet will receive the same amount of energy as the Earth receives from the Sun. For the majority of targets, the existing Doppler sets are not yet sensitive to Neptune-mass planets at their respective EEIDs, which would preclude the formation of stable Earth analogs, let alone Earth-mass planets themselves.

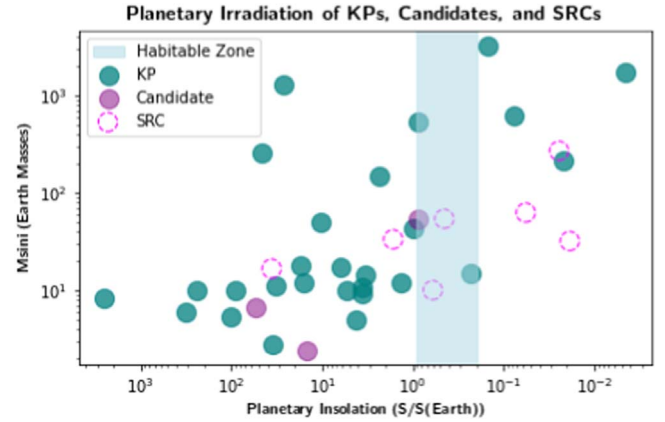


Figure 12. Planet, Candidate, or SRC planetary irradiation relative to Earth (S/S_{\oplus}) vs. $M \sin i$ (M_{\oplus}). The habitable zone for an Earth analog in a solar-analog system (Kopparapu et al. 2014) is marked in the blue shaded region.

For those targets that are closer to the 1 M_{\oplus} line, we suggest more in-depth analysis of the archival data in order to push this limit.

The final uninformed search and injection/recovery figures created by RVSearch are presented in the accompanying Figure Sets so that targets' results may be examined on an individual basis. The RV data used to perform these fits and analyses are presented in an accompanying machine-readable table.

9. Conclusion

We expect the detection and characterization of Earth-analog planets to be an exceptionally difficult undertaking due to the challenges presented by observational constraints, instrument systematics, and, most importantly, the variability of the stars themselves. The list of stars that are well suited to future DI searches for such planets is limited due to stringent requirements on the stars' distance from Earth that in turn determines whether a temperate planet orbiting that star falls outside IWA

Table 12
RV Sensitivity

HD	GJ	Mass (M_{\odot})	References	Lumin. ($\log(L/L_{\odot})$)	References	EEID (au)	Doppler Sens. (M_{\oplus})
693	10	1.08 ± 0.025	1	0.477	11	1.731	403.8
1581	17	1.00 ± 0.025	1	0.101	11	1.123	9.7
2151	19	1.141 ± 0.0125	2	0.541	TW	1.864	44.8
4628	33	0.75 ± 0.02	3	-0.523	11	0.548	13.4
7570	55	1.17 ± 0.0155	2	0.302	11	1.415	88
13445	86A	0.797 ± 0.024	2	-0.389	11	0.639	45.3
14412	95	0.811 ± 0.027	2	-0.351	11	0.668	24.5
16160	105A	0.74 ± 0.02	1	-0.549	11	0.532	12.8
20766	136	0.916 ± 0.0275	2	-0.100	11	0.891	81
20794	139	0.813 ± 0.015	2	-0.184	11	0.809	7.4
20807	138	0.955 ± 0.0265	2	0.007	11	1.008	21.4
22049	144	0.804 ± 0.025	2	-0.471	11	0.582	62.7
23249	150	1.17 ± 0.003	3	0.500	3	1.778	27.6
23356	...	0.80 ± 0.02	4	-0.515	11	0.553	44.7
26965	166A	0.79 ± 0.02	3	-0.364	11	0.658	11.8
30495	177	1.016 ± 0.0225	2	-0.015	11	0.983	393.6
32147	183	0.79 ± 0.02	1	-0.537	11	0.539	9.1
38858	1085	0.95 ± 0.05	3	-0.083	11	0.909	17.2
39091	9189	1.11 ± 0.03	1	0.186	11	1.238	51.1
43834	231	0.962 ± 0.0265	2	-0.063	11	0.930	32
50281	250A	0.75 ± 0.02	4	-0.658	11	0.469	55.9
69830	302	0.89 ± 0.03	3	-0.216	11	0.779	7.4
72673	309	0.788 ± 0.027	2	-0.394	11	0.635	9.6
75732	324A	0.92 ± 0.025	3	-0.197	11	0.797	35
76151	327	1.02 ± 0.025	1	-0.013	11	0.985	17393.5
85512	370	0.704 ± 0.019	5	-0.778	11	0.408	3.7
100623	432A	0.774 ± 0.026	2	-0.432	11	0.608	19.2
102365	442A	0.89 ± 0.035	3	-0.074	11	0.919	13.6
102870	449	1.298 ± 0.0415	2	0.576	11	1.941	201.6
104304	454	0.99 ± 0.025	3	-0.054	11	0.940	63.0
114613	9432	1.27 ± 0.02	3	0.626	11	2.055	53.6
115617	506	0.94 ± 0.03	3	-0.078	11	0.914	15.2
125072	542	0.828 ± 0.025	2	-0.466	11	0.585	24.9
131977	570A	0.77 ± 0.03	6	-0.653	11	0.472	171.2
136352	582	0.92 ± 0.03	3	0.012	11	1.014	9.7
140901	599A	0.954 ± 0.019	2	-0.088	11	0.904	95.3
146233	616	1.003 ± 0.025	2	0.039	11	1.046	17.8
149661	631	0.859 ± 0.0265	2	-0.335	11	0.680	110
156026	664	0.6972 ± 0.0253	7	-0.803	11	0.397	13.5
160346	688	0.785 ± 0.025	8	-0.480	6	0.575	87.5
160691	691	1.15 ± 0.035	1	0.278	11	1.378	27.7
188512	771A	1.27 ± 0.065	3	0.780	12	2.455	255.6
190248	780	1.001 ± 0.033	2	0.097	11	1.118	10.9
192310	785	0.82 ± 0.025	3	-0.394	11	0.636	7.8
196761	796	0.86 ± 0.035	3	-0.252	11	0.748	27.1
207129	838	1.07 ± 0.035	1	0.082	11	1.099	35.8
209100	845	0.715 ± 0.019	10	-0.654	11	0.471	18.2
216803	879	0.73 ± 0.015	8	-0.707	11	0.443	176.5

References. (1) Ramírez et al. (2012), (2) Ramírez et al. (2013), (3) Brewer et al. (2016), (4) Maldonado & Villaver (2016), (5) Soto & Jenkins (2018), (6) Luck (2017), (7) Anders et al. (2019), (8) Casagrande et al. (2011), (9) Fekel & Beavers (1983), (10) Delgado Mena et al. (2019), (11) Stassun et al. (2019), (12) Schofield et al. (2019).

(This table is available in machine-readable form.)

of the DI instrument. There are ~ 100 stars identified by the EPRV WG to meet the criteria both for being a suitable DI target and for being amenable to precision RV observations. We have compiled archival RV time-series data from the majority of precision RV spectrographs that have operated in the southern hemisphere over the past two decades for these 50 nearby, Sun-like stars that are likely to be targets of future, space-based, DI missions.

Our primary objective was to quantify each star's RV completeness via the use of an injection/recovery analysis applied to archival RV data. Our results show that the minimum detectable planet mass at 1 au ranges from 6.5–818.5 M_{\oplus} depending on the star, showcasing the heterogeneous state of the archival RV data collected from these targets. While additional data from the spectrographs included in this study are unlikely to reveal the presence of a 10 cm s^{-1} signal due to

a true Earth analog, there is still room for significant improvements to the stars' RV completeness using these current-generation instruments. Future surveys prioritizing those stars for which we are already sensitive to super-Earth/sub-Neptune-type planets ($M_p \sim 10\text{--}20 M_\oplus$) at 1 au could increase our sensitivity closer to the $1 M_\oplus$ limit. Alternatively, focusing on the stars for which we have the least RV data—those where giant planets at 1 au could remain hidden—could identify currently unknown planetary companions that would preclude the existence of a temperate, terrestrial planet.

In the course of preparing each star's RV time series for the injection/recovery analyses, we also performed an uninformed search of the RV data to identify and remove any significant signals. In doing so, we recovered 28 previously published planets. The orbital parameters of many of these planets have not been revisited since their original publication date, which is often 5–10 yr ago. Our updated analysis, which generally includes both additional data from different instruments and a longer observing baseline than previous fits, is able to increase the precision on the planets' periods, eccentricities, and RV semi-amplitudes. Looking at the ratio of the previously published uncertainties to our updated orbital parameter uncertainties, we find mean uncertainty improvements of $2.7\times$ in period, $1.3\times$ in RV semi-amplitude, and $1.4\times$ in eccentricity.

The third key component to this work is the identification and characterization of many stars' variability timescales and amplitudes using the same uninformed search methodology applied to each stars' S-index and, for targets observed by the UCLES instrument, $EW_{H\alpha}$ time series. Understanding a star's rotationally modulated activity signals along with its long-term magnetic activity cycles, both of which can mask the presence of low-amplitude Keplerian signals, will inform the sampling baseline and cadence necessary in future EPRV surveys to model and mitigate these star-based signals. Our work is not an exhaustive analysis of the stars' activity, but in many cases it does provide an initial or refined characterization of the stars' rotation and magnetic cycles. Future work to better quantify these signals and their development over time is encouraged.

If we will someday require extreme-precision RV follow-up of planets detected by DI missions around these stars, then it would well serve the exoplanet community to begin new observing campaigns of these targets in the near term. Dedicated, high-cadence, high-precision ($\sigma_{RV} \leq 1 \text{ m s}^{-1}$) RV monitoring will enable the characterization and potentially mitigation of stellar variability signals on timescales of hours to years alongside the detection of additional, currently unknown planetary companions. Knowledge of how to correctly model and remove signals of both natures will be crucial for any future efforts to measure precise masses for Earth-analog planets.

K.L., J.B., and E.M. were supported by the NASA Exoplanet Exploration Program (ExEP). K.L. acknowledges support from the Whitman College Independent Study and Senior Thesis programs. The research was carried out in part at the Jet Propulsion Laboratory, California Institute of Technology, under a contract with the National Aeronautics and Space Administration (80NM0018D0004).

The work herein is based on observations obtained at the W. M. Keck Observatory, which is operated jointly by the University of California and the California Institute of Technology, and we thank the UC-Keck and NASA-Keck




Time Assignment Committees for their support. We also wish to extend our special thanks to those of Hawaiian ancestry on whose sacred mountain of Maunakea we are privileged to be guests. Without their generous hospitality, the Keck observations presented herein would not have been possible. The work herein is also based on observations obtained with the Automated Planet Finder (APF) telescope and its Levy Spectrometer at Lick Observatory, along with data gathered with the 6.5 m Magellan Telescopes located at Las Campanas Observatory, Chile. We acknowledge the traditional owners of the land on which the Anglo-Australian Telescope (AAT) stands, the Gamilaray people, and pay our respects to elders past and present.

Some observations in the paper made use of the High-Resolution Imaging instrument(s) 'Alopec (and/or Zorro). 'Alopec (and/or Zorro) was funded by the NASA Exoplanet Exploration Program and built at the NASA Ames Research Center by Steve B. Howell, Nic Scott, Elliott P. Horch, and Emmett Quigley. 'Alopec (and/or Zorro) was mounted on the Gemini-North (and/or South) telescope of the international Gemini Observatory, a program of NSF's NOIRLab, which is managed by the Association of Universities for Research in Astronomy (auRA) under a cooperative agreement with the National Science Foundation. On behalf of the Gemini partnership: the National Science Foundation (United States), National Research Council (Canada), Agencia Nacional de Investigación y Desarrollo (Chile), Ministerio de Ciencia, Tecnología e Innovación (Argentina), Ministério da Ciência, Tecnologia, Inovações e Comunicações (Brazil), and Korea Astronomy and Space Science Institute (Republic of Korea).

This research has made use of the SIMBAD database, operated at CDS, Strasbourg, France.

Facilities: UCO/Lick: The APF (Levy spectrograph), Magellan: Clay (Planet Finder Spectrograph), Keck: I (HIRES), Gemini-North: 'Alopec, Gemini-South: Zorro.

ORCID iDs

Katherine Lalot  <https://orcid.org/0000-0002-6111-6061>
 Jennifer A. Burt  <https://orcid.org/0000-0002-0040-6815>
 Eric E. Mamajek  <https://orcid.org/0000-0003-2008-1488>
 Zhexiong Li  <https://orcid.org/0000-0002-4860-7667>
 Jinglin Zhao  <https://orcid.org/0000-0001-5290-2952>
 R. Paul Butler  <https://orcid.org/0000-0003-1305-3761>
 Bradford Holden  <https://orcid.org/0000-0002-6153-3076>
 Lee Rosenthal  <https://orcid.org/0000-0001-8391-5182>
 B. J. Fulton  <https://orcid.org/0000-0003-3504-5316>
 Fabo Feng  <https://orcid.org/0000-0001-6039-0555>
 Stephen R. Kane  <https://orcid.org/0000-0002-7084-0529>
 Jeremy Bailey  <https://orcid.org/0000-0002-5726-7000>
 Brad Carter  <https://orcid.org/0000-0003-0035-8769>
 Jeffrey D. Crane  <https://orcid.org/0000-0002-5226-787X>
 Elise Furlan  <https://orcid.org/0000-0001-9800-6248>
 Crystal L. Gnllka  <https://orcid.org/0000-0003-2519-6161>
 Steve B. Howell  <https://orcid.org/0000-0002-2532-2853>
 Gregory Laughlin  <https://orcid.org/0000-0002-3253-2621>
 Stephen A. Shectman  <https://orcid.org/0000-0002-8681-6136>
 C. G. Tinney  <https://orcid.org/0000-0002-7595-0970>
 Steven S. Vogt  <https://orcid.org/0000-0001-7177-7456>
 Sharon Xuesong Wang  <https://orcid.org/0000-0002-6937-9034>
 Robert A. Wittenmyer  <https://orcid.org/0000-0001-9957-9304>

References

- Adibekyan, V., Delgado-Mena, E., Figueira, P., et al. 2016, *A&A*, **591**, A34
- Adibekyan, V. Z., Sousa, S. G., Santos, N. C., et al. 2012, *A&A*, **545**, A32
- Aguilera-Gómez, C., Ramírez, I., & Charnamé, J. 2018, *A&A*, **614**, A55
- Ammler-von Eiff, M., & Reiners, A. 2012, *A&A*, **542**, A116
- Anders, F., Khalatyan, A., Chiappini, C., et al. 2019, *A&A*, **628**, A94
- Baliunas, S., Sokoloff, D., & Soon, W. 1996, *ApJL*, **457**, L99
- Baliunas, S. L., Donahue, R. A., Soon, W. H., et al. 1995, *ApJ*, **438**, 269
- Baluev, R. V. 2015, *MNRAS*, **446**, 1493
- Batalha, N. E., Lewis, T., Fortney, J. J., et al. 2019, *ApJL*, **885**, L25
- Bayo, A., Rodrigo, C., Barrado Y Navascués, D., et al. 2008, *A&A*, **492**, 277
- Beichman, C. A., Bryden, G., Gautier, T. N., et al. 2005, *ApJ*, **626**, 1061
- Benedict, G. F., McArthur, B. E., Nelan, E. P., et al. 2022, *AJ*, **163**, 295
- Boro Saikia, S., Marvin, C. J., Jeffers, S. V., et al. 2018, *A&A*, **616**, A108
- Bouchy, F., & Carrier, F. 2001, *A&A*, **374**, L5
- Bourrier, V., Dumusque, X., Dorn, C., et al. 2018, *A&A*, **619**, A1
- Brandão, I. M., Doğan, G., Christensen-Dalsgaard, J., et al. 2011, *A&A*, **527**, A37
- Brewer, J. M., Fischer, D. A., Blackman, R. T., et al. 2020, *AJ*, **160**, 67
- Brewer, J. M., Fischer, D. A., Valenti, J. A., & Piskunov, N. 2016, *ApJS*, **225**, 32
- Burgasser, A. J., Kirkpatrick, J. D., Cutri, R. M., et al. 2000, *ApJL*, **531**, L57
- Burt, J., Feng, F., Holden, B., et al. 2021, *AJ*, **161**, 10
- Busko, I. C., & Torres, C. A. O. 1978, *A&A*, **64**, 153
- Butkovskaya, V. V., Plachinda, S. I., Bondar', N. I., & Baklanova, D. N. 2017, *AN*, **338**, 896
- Butler, R. P., Marcy, G. W., Williams, E., et al. 1996, *PASP*, **108**, 500
- Butler, R. P., Tinney, C. G., Marcy, G. W., et al. 2001, *ApJ*, **555**, 410
- Butler, R. P., Vogt, S. S., Laughlin, G., et al. 2017, *AJ*, **153**, 208
- Butler, R. P., Wright, J. T., Marcy, G. W., et al. 2006, *ApJ*, **646**, 505
- Casagrande, L., Schönrich, R., Asplund, M., et al. 2011, *A&A*, **530**, A138
- Casali, G., Spina, L., Magrini, L., et al. 2020, *A&A*, **639**, A127
- Cayrel de Strobel, G., Perrin, M. N., Cayrel, R., & Lebreton, Y. 1989, *A&A*, **225**, 369
- Cegla, H. M., Watson, C. A., Shelyag, S., Mathioudakis, M., & Moutari, S. 2019, *ApJ*, **879**, 55
- Choi, J., Dotter, A., Conroy, C., et al. 2016, *ApJ*, **823**, 102
- Cincunegui, C., Díaz, R. F., & Mauas, P. J. D. 2007, *A&A*, **469**, 309
- Corsaro, E., Grundahl, F., Leccia, S., et al. 2012, *A&A*, **537**, A9
- Cosentino, R., Lovis, C., Pepe, F., et al. 2012, *Proc. SPIE*, **8446**, 84461V
- Costes, J. C., Watson, C. A., de Mooij, E., et al. 2021, *MNRAS*, **505**, 830
- Crane, J. D., Shectman, S. A., & Butler, R. P. 2006, *Proc. SPIE*, **6269**, 626931
- Crane, J. D., Shectman, S. A., Butler, R. P., et al. 2010, *Proc. SPIE*, **7735**, 773553
- Crane, J. D., Shectman, S. A., Butler, R. P., Thompson, I. B., & Burley, G. S. 2008, *Proc. SPIE*, **7014**, 701479
- Crass, J., Gaudi, B. S., Leifer, S., et al. 2021, arXiv:2107.14291
- Croll, B., Walker, G. A. H., Kuschnig, R., et al. 2006, *ApJ*, **648**, 607
- Cumming, A., Marcy, G. W., & Butler, R. P. 1999, *ApJ*, **526**, 890
- da Silva, R., Milone, A. d. C., & Rocha-Pinto, H. J. 2015, *A&A*, **580**, A24
- Dannert, F. A., Ottiger, M., Quanz, S. P., et al. 2022, *A&A*, **664**, A22
- Dawson, R. I., & Fabrycky, D. C. 2010, *ApJ*, **722**, 937
- De Rosa, R. J., Esposito, T. M., Hirsch, L. A., et al. 2019, *AJ*, **158**, 225
- Dekker, H., D'Odorico, S., Kaufer, A., Delabre, B., & Kotzłowski, H. 2000, *Proc. SPIE*, **4008**, 534
- Delgado Mena, E., Moya, A., Adibekyan, V., et al. 2019, *A&A*, **624**, A78
- Delrez, L., Ehrenreich, D., Alibert, Y., et al. 2021, *NatAs*, **5**, 775
- Díaz, M. R., Jenkins, J. S., Tuomi, M., et al. 2018, *AJ*, **155**, 126
- Diego, F., Charalambous, A., Fish, A. C., & Walker, D. D. 1990, *Proc. SPIE*, **1235**, 562
- Donahue, R. A. 1996, in *Stellar Surface Structure*, ed. K. G. Strassmeier & J. L. Linsky, Vol. 176 (Dordrecht: Kluwer), 261
- Donahue, R. A., Saar, S. H., & Baliunas, S. L. 1996, *ApJ*, **466**, 384
- Dumusque, X., Lovis, C., Ségransan, D., et al. 2011, *A&A*, **535**, A55
- Duncan, D. K., Vaughan, A. H., Wilson, O. C., et al. 1991, *ApJS*, **76**, 383
- Eaton, J. A., & Poe, C. H. 1985, *IBVS*, **2712**, 1
- Egeland, R., Metcalfe, T. S., Hall, J. C., & Henry, G. W. 2015, *ApJ*, **812**, 12
- EGgenberger, A., Udry, S., Chauvin, G., et al. 2007, *A&A*, **474**, 273
- Eiroa, C., Marshall, J. P., Mora, A., et al. 2013, *A&A*, **555**, A11
- Endl, M., Robertson, P., Cochran, W. D., et al. 2012, *ApJ*, **759**, 19
- ESA 1997, *ESA SO-1200, The HIPPARCOS and TYCHO Catalogues* (Noorwijk: ESA)
- Faramaz, V., Bryden, G., Stapelfeldt, K. R., et al. 2018, *MNRAS*, **481**, 44
- Farhi, J., Bond, H. E., Dufour, P., et al. 2013, *MNRAS*, **430**, 652
- Fekel, F. C. J., & Beavers, W. I. 1983, *ApJ*, **267**, 682
- Feng, F., Anglada-Escudé, G., Tuomi, M., et al. 2019a, *MNRAS*, **490**, 5002
- Feng, F., Lisogorskyi, M., Jones, H. R. A., et al. 2019b, *ApJS*, **244**, 39
- Feng, F., Tuomi, M., & Jones, H. R. A. 2017a, *MNRAS*, **470**, 4794
- Feng, F., Tuomi, M., Jones, H. R. A., et al. 2017b, *AJ*, **154**, 135
- Fischer, D. A. 2018, in *Handbook of Exoplanets*, ed. Hans J. Deeg & Juan Antonio Belmonte (New York: Springer)
- Fischer, D. A., Marcy, G. W., Butler, R. P., et al. 2008, *ApJ*, **675**, 790
- Fisher, G. F., Hall, D. S., Henry, G. W., et al. 1983, *IBVS*, **2259**, 1
- Flores, M., Jaque Arancibia, M., Ibañez Bustos, R. V., et al. 2021, *A&A*, **645**, L6
- Foreman-Mackey, D., Hogg, D. W., Lang, D., & Goodman, J. 2013, *PASP*, **125**, 306
- Forveille, T., Beuzit, J.-L., Delfosse, X., et al. 1999, *A&A*, **351**, 619
- Frey, G. J., Grim, B., Hall, D. S., et al. 1991, *AJ*, **102**, 1813
- Frick, P., Soon, W., Popova, E., & Baliunas, S. 2004, *NewA*, **9**, 599
- Fuhrmeister, B., Czesla, S., Nagel, E., et al. 2022, *A&A*, **657**, A125
- Fulton, B. J., Petigura, E. A., Blunt, S., & Sinukoff, E. 2018, *PASP*, **130**, 044504
- Gaia Collaboration, Brown, A. G. A., Vallenari, A., et al. 2018, *A&A*, **616**, A1
- Gaia Collaboration, Brown, A. G. A., Vallenari, A., et al. June 2021a, *A&A*, **650**, C3
- Gaia Collaboration, Brown, A. G. A., Vallenari, A., et al. 2021b, *A&A*, **649**, A1
- Gaidos, E. J., Henry, G. W., & Henry, S. M. 2000, *AJ*, **120**, 1006
- Gandolfi, D., Barragán, O., Livingston, J. H., et al. 2018, *A&A*, **619**, L10
- Garg, S., Karak, B. B., Egeland, R., Soon, W., & Baliunas, S. 2019, *ApJ*, **886**, 132
- Gáspár, A., Rieke, G. H., & Balog, Z. 2013, *ApJ*, **768**, 25
- Gaudi, B. S., Seager, S., Mennesson, B., et al. 2020, arXiv:2001.06683
- Gentile Fusillo, N. P., Tremblay, P.-E., Gänsicke, B. T., et al. 2019, *MNRAS*, **482**, 4570
- Golimowski, D. A., Henry, T. J., Krist, J. E., et al. 2000, *AJ*, **120**, 2082
- Golimowski, D. A., Nakajima, T., Kulkarni, S. R., & Oppenheimer, B. R. 1995, *ApJL*, **444**, L101
- Gomes da Silva, J., Santos, N. C., Adibekyan, V., et al. 2021, *A&A*, **646**, A77
- Gomes da Silva, J., Santos, N. C., Boisse, I., Dumusque, X., & Lovis, C. 2014, *A&A*, **566**, A66
- Gondoin, P. 2020, *A&A*, **641**, A110
- Gonzalez, G., Carlson, M. K., & Tobin, R. W. 2010, *MNRAS*, **403**, 1368
- Gray, R. O., Corbally, C. J., Garrison, R. F., et al. 2006, *AJ*, **132**, 161
- Gray, R. O., Corbally, C. J., Garrison, R. F., McFadden, M. T., & Robinson, P. E. 2003, *AJ*, **126**, 2048
- Gray, R. O., Napier, M. G., & Winkler, L. I. 2001, *AJ*, **121**, 2148
- Halbwachs, J. L., Mayor, M., & Udry, S. 2018, *A&A*, **619**, A81
- Hall, D. S. 1976, *IAU Coll. 29: Multiple Periodic Variable Stars*, ed. W. S. Fitch, (Dordrecht: Springer), 287
- Hall, J. C., Lockwood, G. W., & Skiff, B. A. 2007, *AJ*, **133**, 862
- Hansen, J. T., Ireland, M. J., & LIFE Collaboration 2022, *A&A*, **664**, A52
- Haslebach, C., Demory, M. E., Demory, B. O., Sarazin, M., & Vidale, P. L. 2022, *A&A*, **665**, A149
- Hathaway, D. H. 2015, *LRSP*, **12**, 4
- Hatzes, A. P., Gandolfi, D., Korth, J., et al. 2022, *AJ*, **163**, 223
- Haywood, R. D., Collier Cameron, A., Unruh, Y. C., et al. 2016, *MNRAS*, **457**, 3637
- Heintz, W. D., & Cantor, B. A. 1994, *PASP*, **106**, 363
- Henry, T. J., Walkowicz, L. M., Barto, T. C., & Golimowski, D. A. 2002, *AJ*, **123**, 2002
- Hinkel, N. R., Mamajek, E. E., Turnbull, M. C., et al. 2017, *ApJ*, **848**, 34
- Hojjatpanah, S., Oshagh, M., Figueira, P., et al. 2020, *A&A*, **639**, A35
- Holberg, J. B., Oswalt, T. D., Sion, E. M., & McCook, G. P. 2016, *MNRAS*, **462**, 2295
- Horch, E. P., Broderick, K. G., Casetti-Dinescu, D. I., et al. 2021, *AJ*, **161**, 295
- Horch, E. P., Gomez, S. C., Sherry, W. H., et al. 2011, *AJ*, **141**, 45
- Houk, N., & Cowley, A. P. 1975, *University of Michigan Catalogue of Two-dimensional Spectral types for the HD Stars. Volume I. Declinations -90 to -53* (Ann Arbor, MI: Univ. Michigan)
- Howard, A. W., & Fulton, B. J. 2016, *PASP*, **128**, 114401
- Howell, S. B., Everett, M. E., Sherry, W., Horch, E., & Ciardi, D. R. 2011, *AJ*, **142**, 19
- Huang, C. X., Burt, J., Vanderburg, A., et al. 2018, *ApJL*, **868**, L39
- Husser, T. O., Wende-von Berg, S., Dreizler, S., et al. 2013, *A&A*, **553**, A6
- Ianna, P. A. 1992, in *ASP Conf. Ser. 32, Complementary Approaches to Double and Multiple Star Research*, ed. H. A. McAlister & W. I. Hartkopf (San Francisco, CA: ASP), 323
- Ibukiyama, A., & Arimoto, N. 2002, *A&A*, **394**, 927
- Isaacson, H., & Fischer, D. 2010, *ApJ*, **725**, 875
- Jofré, P., Heiter, U., Soubiran, C., et al. 2014, *A&A*, **564**, A133

- Jofré, P., Heiter, U., Soubiran, C., et al. 2015, *A&A*, **582**, A81
- Johnson, H. L., & Morgan, W. W. 1953, *ApJ*, **117**, 313
- Jones, H. R. A., Paul Butler, R., Tinney, C. G., et al. 2002, *MNRAS*, **333**, 871
- Jourdain de Muizon, M., Laureijs, R. J., Dominik, C., et al. 1999, *A&A*, **350**, 875
- Kane, S. R., Yalçinkaya, S., Osborn, H. P., et al. 2020, *AJ*, **160**, 129
- Kass, R., & Raftery, A. 1995, *JASA*, **90**, 773
- Katoh, N., Itoh, Y., Toyota, E., & Sato, B. 2013, *AJ*, **145**, 41
- Keenan, P. C., & McNeil, R. C. 1989, *ApJS*, **71**, 245
- Kervella, P., Arenou, F., Mignard, F., & Thévenin, F. 2019, *A&A*, **623**, A72
- Kervella, P., Arenou, F., & Thévenin, F. 2022, *A&A*, **657**, A7
- Kipping, D. M. 2013, *MNRAS*, **434**, L51
- Kiyaeva, O. V., Kiselev, A. A., & Izmailov, I. S. 2008, *AstL*, **34**, 405
- Konrad, B. S., Alei, E., Quanz, S. P., et al. 2022, *A&A*, **664**, A23
- Kopparapu, R. K., Ramirez, R. M., SchottelKotte, J., et al. 2014, *ApJL*, **787**, L29
- Krist, J. E., Stapelfeldt, K. R., Bryden, G., et al. 2010, *AJ*, **140**, 1051
- Lippincott, S. L. 1973, *AJ*, **78**, 303
- Lloyd Evans, T., & Koen, M. C. J. 1987, *SAOOC*, **11**, 21
- Lockwood, G. W., Skiff, B. A., Henry, G. W., et al. 2007, *ApJS*, **171**, 260
- Lovis, C., Dumusque, X., Santos, N. C., et al. 2011, arXiv:1107.5325
- Lovis, C., & Fischer, D. 2010, in *Exoplanets*, ed. S. Seager (Tuscon, AZ: Univ. Arizona Press), 27
- Lovis, C., Mayor, M., Pepe, F., et al. 2006, *Natur*, **441**, 305
- Luck, R. E. 2017, *AJ*, **153**, 21
- Luhn, J. K., Wright, J. T., Howard, A. W., & Isaacson, H. 2020, *AJ*, **159**, 235
- Ma, B., Ge, J., Muterspaugh, M., et al. 2018, *MNRAS*, **480**, 2411
- Mahdi, D., Soubiran, C., Blanco-Cuaresma, S., & Chemin, L. 2016, *A&A*, **587**, A131
- Makarov, V. V. 2010, *ApJ*, **715**, 500
- Makarov, V. V., Zacharias, N., & Finch, C. T. 2021, *RNAAS*, **5**, 108
- Maldonado, J., Eiroa, C., Villaver, E., Montesinos, B., & Mora, A. 2012, *A&A*, **541**, A40
- Maldonado, J., & Villaver, E. 2016, *A&A*, **588**, A98
- Maldonado, J., Villaver, E., & Eiroa, C. 2013, *A&A*, **554**, A84
- Mamajek, E. E., Bartlett, J. L., Seifahrt, A., et al. 2013, *AJ*, **146**, 154
- Mamajek, E. E., & Hillenbrand, L. A. 2008, *ApJ*, **687**, 1264
- Mann, A. W., Feiden, G. A., Gaidos, E., Boyajian, T., & von Braun, K. 2015, *ApJ*, **804**, 64
- Marcy, G. 2007, in *The Direct Detection of Planets and Circumstellar Disks in the 21st Century*, ed. Paul Kalas Berkeley, CA (Univ. California)
- Marshall, J. P., Löhne, T., Montesinos, B., et al. 2011, *A&A*, **529**, A117
- Mason, B. D., Wycoff, G. L., Hartkopf, W. I., Douglass, G. G., & Worley, C. E. 2001, *AJ*, **122**, 3466
- Mawet, D., Hirsch, L., Lee, E. J., et al. 2019, *AJ*, **157**, 33
- Mayor, M., Pepe, F., Queloz, D., et al. 2003, *Msngr*, **114**, 20
- Mermilliod, J. C. 2006, *yCat*, **II/168**
- Metcalf, T. S., Buccino, A. P., Brown, B. P., et al. 2013, *ApJL*, **763**, L26
- Meunier, N., Desert, M., & Lagrange, A. M. 2010, *A&A*, **512**, A39
- Meunier, N., Kretzschmar, M., Gravet, R., Mignon, L., & Delfosse, X. 2022, *A&A*, **658**, A57
- Meunier, N., & Lagrange, A. M. 2019, *A&A*, **625**, L6
- Meunier, N., & Lagrange, A. M. 2020, *A&A*, **638**, A54
- Meunier, N., Lagrange, A. M., Borgniet, S., & Rieutord, M. 2015, *A&A*, **583**, A118
- Meunier, N., Lagrange, A. M., Mbemba Kabuiku, L., et al. 2017, *A&A*, **597**, A52
- Mishenina, T. V., Soubiran, C., Kovtyukh, V. V., Katsova, M. M., & Livshits, M. A. 2012, *A&A*, **547**, A106
- Mishenina, T. V., Soubiran, C., Kovtyukh, V. V., & Korotin, S. A. 2004, *A&A*, **418**, 551
- Mittag, M., Schmitt, J. H. M. M., & Schröder, K. P. 2013, *A&A*, **549**, A117
- Montes, D., González-Peinado, R., Tabernero, H. M., et al. 2018, *MNRAS*, **479**, 1332
- Morel, T., Micela, G., Favata, F., & Katz, D. 2004, *A&A*, **426**, 1007
- Mortier, A., & Collier Cameron, A. 2017, *A&A*, **601**, A110
- Mugrauer, M. 2019, *MNRAS*, **490**, 5088
- National Academies of Sciences, Engineering, and Medicine 2018, *Exoplanet Science Strategy* (Washington, DC: The National Academies Press)
- National Academies of Sciences, Engineering, and Medicine 2021, *Pathways to Discovery in Astronomy and Astrophysics for the 2020s* (Washington, DC: The National Academies Press)
- Nissen, P. E., Christensen-Dalsgaard, J., Mosumgaard, J. R., et al. 2020, *A&A*, **640**, A81
- Noyes, R. W., Hartmann, L. W., Baliunas, S. L., Duncan, D. K., & Vaughan, A. H. 1984, *ApJ*, **279**, 763
- Oelkers, R. J., Rodríguez, J. E., Stassun, K. G., et al. 2018, *AJ*, **155**, 39
- Oláh, K., Kővári, Z., Petrovay, K., et al. 2016, *A&A*, **590**, A133
- Pepe, F., Correia, A. C. M., Mayor, M., et al. 2007, *A&A*, **462**, 769
- Pepe, F., Cristiani, S., Rebolo, R., et al. 2021, *A&A*, **645**, A96
- Pepe, F., Lovis, C., Ségransan, D., et al. 2011, *A&A*, **534**, A58
- Pepe, F., Mayor, M., Rupprecht, G., et al. 2002, *Msngr*, **110**, 9
- Perdelwitz, V., Mittag, M., Tal-Or, L., et al. 2021, *A&A*, **652**, A116
- Pourbaix, D., Tokovinin, A. A., Batten, A. H., et al. 2004, *A&A*, **424**, 727
- Quanz, S. P., Ottiger, M., Fontanet, E., et al. 2022, *A&A*, **664**, A21
- Quirrenbach, A. 2010, in *Exoplanets*, ed. S. Seager (Tuscon, AZ: Univ. Arizona Press), 157
- Radick, R. R., Lockwood, G. W., Henry, G. W., Hall, J. C., & Pevtsov, A. A. 2018, *ApJ*, **855**, 75
- Ramírez, I., Allende Prieto, C., & Lambert, D. L. 2013, *ApJ*, **764**, 78
- Ramírez, I., Fish, J. R., Lambert, D. L., & Allende Prieto, C. 2012, *ApJ*, **756**, 46
- Ramírez, I., Meléndez, J., Bean, J., et al. 2014, *A&A*, **572**, A48
- Reinhold, T., Reiners, A., & Basri, G. 2013, *A&A*, **560**, A4
- Robertson, P., Endl, M., Cochran, W. D., & Dodson-Robinson, S. E. 2013, *ApJ*, **764**, 3
- Robertson, P., Mahadevan, S., Endl, M., & Roy, A. 2014, *Sci*, **345**, 440
- Rosenthal, L. J., Fulton, B. J., Hirsch, L. A., et al. 2021, *ApJS*, **255**, 8
- Saar, S. H., & Brandenburg, A. 1999, *ApJ*, **524**, 295
- Saar, S. H., & Donahue, R. A. 1997, *ApJ*, **485**, 319
- Saar, S. H., & Osten, R. A. 1997, *MNRAS*, **284**, 803
- Samus', N. N., Kazarovets, E. V., Durlevich, O. V., Kireeva, N. N., & Pastukhova, E. N. 2017, *ARep*, **61**, 80
- Santos, N. C., Israelian, G., & Mayor, M. 2001, *A&A*, **373**, 1019
- Santos, N. C., Israelian, G., & Mayor, M. 2004, *A&A*, **415**, 1153
- Schnupp, C., Bergfors, C., Brandner, W., et al. 2010, *A&A*, **516**, A21
- Schofield, M., Chaplin, W. J., Huber, D., et al. 2019, *ApJS*, **241**, 12
- Schrijver, C. J. 1987, *A&A*, **172**, 111
- Schwabe, M. 1843, *AN*, **20**, 283
- Scott, N. J., Howell, S. B., Gnilka, C. L., et al. 2021, *FrASS*, **8**, 138
- Seager, S., Kasdin, J., & Starshade Rendezvous Probe Team 2018, *AAS Meeting Abstracts*, **231**, 121.09
- Seifahrt, A., Stürmer, J., Bean, J. L., & Schwab, C. 2018, *Proc. SPIE*, **10702**, 107026D
- Sierchio, J. M., Rieke, G. H., Su, K. Y. L., & Gáspár, A. 2014, *ApJ*, **785**, 33
- Simpson, E. K., Baliunas, S. L., Henry, G. W., & Watson, C. A. 2010, *MNRAS*, **408**, 1666
- Soriano, M., & Vauclair, S. 2010, *A&A*, **513**, A49
- Soto, M. G., & Jenkins, J. S. 2018, *A&A*, **615**, A76
- Soubiran, C., Brouillet, N., & Casamiquela, L. 2022, *A&A*, **663**, A4
- Soubiran, C., & Girard, P. 2005, *A&A*, **438**, 139
- Soubiran, C., Jasiewicz, G., Chemin, L., et al. 2018, *A&A*, **616**, A7
- Sousa, S. G., Adibekyan, V., Delgado-Mena, E., et al. 2018, *A&A*, **620**, A58
- Sousa, S. G., Santos, N. C., Mayor, M., et al. 2008, *A&A*, **487**, 373
- Spina, L., Meléndez, J., Karakas, A. I., et al. 2018, *MNRAS*, **474**, 2580
- Spina, L., Meléndez, J., & Ramírez, I. 2016, *A&A*, **585**, A152
- Stassun, K. G., Oelkers, R. J., Paegert, M., et al. 2019, *AJ*, **158**, 138
- Nordlund, Å., Stein, R. F., & Asplund, M. 2009, *LRSP*, **6**, 2
- Takeda, Y., Ohkubo, M., Sato, B., Kambe, E., & Sadakane, K. 2005, *PASJ*, **57**, 27
- The LUVOIR Team 2019, arXiv:1912.06219
- Thévenin, F., Kervella, P., Pichon, B., et al. 2005, *A&A*, **436**, 253
- Tian, H.-J., El-Badry, K., Rix, H.-W., & Gould, A. 2020, *ApJS*, **246**, 4
- Tinney, C. G., Butler, R. P., Jones, H. R. A., et al. 2011, *ApJ*, **727**, 103
- Tokovinin, A. 2014, *AJ*, **147**, 86
- Tokovinin, A. A. 1991, *A&AS*, **91**, 497
- Trifonov, T., Caballero, J. A., Morales, J. C., et al. 2021, *Sci*, **371**, 1038
- Trifonov, T., Tal-Or, L., Zechmeister, M., et al. 2020, *A&A*, **636**, A74
- Trilling, D. E., Bryden, G., Beichman, C. A., et al. 2008, *ApJ*, **674**, 1086
- Tsantaki, M., Sousa, S. G., Adibekyan, V. Z., et al. 2013, *A&A*, **555**, A150
- Udry, S., Dumusque, X., Lovis, C., et al. 2019, *A&A*, **622**, A37
- Valenti, J. A., & Fischer, D. A. 2005, *ApJS*, **159**, 141
- van Leeuwen, F. 2007, *A&A*, **474**, 653
- van Maanen, A. 1938, *ApJ*, **88**, 27
- Vidotto, A. A., Gregory, S. G., Jardine, M., et al. 2014, *MNRAS*, **441**, 2361
- Vogt, S. S., Allen, S. L., Bigelow, B. C., et al. 1994, *Proc. SPIE*, **2198**, 362
- Vogt, S. S., Radovan, M., Kibrick, R., et al. 2014, *PASP*, **126**, 359
- Vogt, S. S., Wittenmyer, R. A., Butler, R. P., et al. 2010, *ApJ*, **708**, 1366
- Watson, C. A., Littlefair, S. P., Diamond, C., et al. 2011, *MNRAS*, **413**, L71
- Willamo, T., Hackman, T., Lehtinen, J. J., et al. 2020, *A&A*, **638**, A69
- Wilson, O. C. 1968, *ApJ*, **153**, 221
- Wittenmyer, R. A., Endl, M., Cochran, W. D., et al. 2006, *AJ*, **132**, 177

- Wittenmyer, R. A., Horner, J., Tinney, C. G., et al. 2014, [ApJ](#), **783**, 103
- Wittenmyer, R. A., Jones, M. I., Zhao, J., et al. 2017, [AJ](#), **153**, 51
- Wright, N. J., Drake, J. J., Mamajek, E. E., & Henry, G. W. 2011, [ApJ](#), **743**, 48
- Xuan, J. W., & Wyatt, M. C. 2020, [MNRAS](#), **497**, 2096
- Zacharias, N., Finch, C., Subasavage, J., et al. 2015, [AJ](#), **150**, 101
- Zechmeister, M., Kürster, M., Endl, M., et al. 2013, [A&A](#), **552**, A78
- Zechmeister, M., Reiners, A., Amado, P. J., et al. 2018, [A&A](#), **609**, A12
- Zechmeister, M., Reiners, A., Amado, P. J., et al. 2020, [SERVAL: SpEctrum Radial Velocity AnaLyser](#), Astrophysics Source Code Library, [ascl:2006.011](#)